

https://dspace.org/

Fabrication of erosion resistant WC-Ni based coatings using cold gas dynamic spaying

Lioma, Dineo Boitumelo Thansanqa

2019

https://hdl.handle.net/10539/28988

Downloaded from a DSpace repository. https://dspace.org/



UNIVERSITY OF THE
WITWATERSRAND,
JOHANNESBURG

Fabrication of erosion resistant WC-Ni based coatings using cold gas dynamic spraying

Dineo Boitumelo Thansanqa Lioma

A dissertation submitted to the Faculty of Engineering and the Built Environment, University of the Witwatersrand, in fulfilment of the requirements for the degree of Master of Science in Engineering.

Johannesburg, 2019

Declaration

I declare that this dissertation is my own unaided work. It is being submitted to the University of the Witwatersrand, Johannesburg for the Degree of Master of Science in Engineering. It has not been submitted before for examination to any other university.

Name: _____ Signature: _____

Date: _____

Acknowledgements

Firstly, I would like to thank my Lord Jesus Christ whom I love deeply. Thank you for showing me that I can achieve anything as I continue to walk beside You. Another thank you for the encouragement and for always giving me the strength that I needed throughout the duration of my research project; I am forever grateful.

To my supervisors, Prof Natasha Sacks and Prof Botef, thank you for the guidance and knowledge which facilitated this research. I would also like to express my sincere gratitude for allowing me to take a sabbatical from my studies as I pursued an MPhil in Micro and Nanotechnology Enterprise at the University of Cambridge. To Prof Botef, I wish you could be present to celebrate my graduation day; I will carry your wise teachings and the memories I have of you in my heart forever. Much appreciation is shown to Dr Agripa Hamweendo who immensely facilitated the progress of my work; Thank you for spending endless hours with me in the lab and for teaching me everything that I know about the cold spray process. I wish to acknowledge Mr Brayner Nelwalani who assisted me with the microscopy, erosion and corrosion experiments that were pivotal for this work. I also thank Dr Christopher Freemantle, Dr Rodney Genga, Mr Gerrard Peter and Mr Shadrack Maqobulane who helped me use the equipment that I needed to conduct my experiments. Pilot Tools Pty South Africa is also acknowledged for the use of their facilities. The financial support of the Centre of Excellence in Strong Materials, the Department of Science and Technology and the National Research Foundation in South Africa (grant no. 41292) that enabled this research is also acknowledged.

Last, but certainly not least, I thank my beloved family and friends for all the love, support and encouragement they shared with me throughout this journey.

Abstract

The feasibility of using a low pressure cold spray system for the fabrication of erosion resistant WC-Ni based coatings was investigated. Three different types of WC-based powders; namely, an oxide reduced WC (WC_{ox}), agglomerated and sintered WC-12 wt% Co (WC_{12Co}) and WC-10 wt% Ni (WC_{10Ni}), mechanically blended with nickel (Ni) were used in this study. The wt% Ni, deposition temperature, stagnation pressure and gun-substrate stand-off distance were varied in which the optimal spray parameters were determined using a Taguchi mixed-level design of experiments method. The deposition of the hard and brittle carbide powders proved to be challenging unless co-deposited with the ductile Ni binder. Particle bonding was achieved through the high pressures generated during impact which allowed the Ni to undergo severe plastic deformation, resulting in material interlocking. Low porosity coating build-up with a non-homogenous distribution of the carbide phase was observed across all the coatings.

The WC_{ox}-4Ni coating possessed the maximum hardness of 464 ± 15 $HV_{0.3}$ out of all the powder combinations and was subsequently selected to undergo slurry erosion and corrosion testing. The addition of 10 wt% TiC and 1 wt% Mo improved the overall hardness of the coatings, however, decreased the erosion resistance at an impact angle of 90°. Two distinct modes of erosive wear took place, namely, erosion by plastic deformation and brittle fracture, respectively characterised by the plastic deformation of the Ni binder and the extensive particle fracture and grain pull-out of the carbide phase. Long wear paths were also observed within the Ni matrix which was indicative of a two-body abrasive wear mechanism. The addition of Mo decreased the corrosion resistance of the coatings as the metal starts to erode at high humidity levels and when placed in water.

The slurry erosion performance of the cold sprayed WC_{ox}-Ni coatings was also compared to WC-Co coatings produced by HVOF techniques. It was found that the cold sprayed coatings experienced lower erosion rates at an impact angle of 90°. This can be attributed to the presence of the ductile Ni binder which was able to absorb the impact energy of the erodents. XRD analyses of the resultant cold sprayed coatings indicated that no detrimental phase transformations typical of HVOF techniques took place during deposition, further supporting their increased wear resistance. These findings indicate that low-pressure systems can potentially be used as an alternative to fabricate slurry erosion resistance for applications with an impact angle of 90°, however, further research on the technique is still required.

Table of Contents

Declaration ..... **i**

Acknowledgements ..... **ii**

Abstract ..... **iii**

Abbreviations ..... **xiii**

1. Introduction **1**

2. Literature Review **5**

2.1. WC-based coatings 5

2.2. Thermal spraying of WC-based coatings 6

2.2.1. HVOF deposition of WC-based coatings 7

2.3. Cold Gas dynamic spraying 10

2.3.1. Fundamentals 10

2.3.2. CGDS Equipment 12

2.3.3. Deposition mechanism 14

2.3.4. Cold gas dynamic spraying of WC 16

2.4. Wear fundamentals 24

2.4.1. Slurry erosion 24

2.4.1.1. Slurry erosion mechanism 26

2.4.2. Abrasion 28

2.5. Wear of cold sprayed coatings 30

2.6. Corrosion fundamentals 33

2.6.1. Passivation 36

2.7. Corrosion of WC-based coatings 37

2.8. Erosion-Corrosion 38

2.9. Experimental parameter optimization 39

3. Materials and Methods **42**

3.1. Powders preparation 42

3.1.1. Mechanical mixing 43

3.1.2. Powder characterization 44

3.2. Deposition parameter optimization 44

3.3. Coating deposition 47

3.3.1. Substrate preparation 47

3.3.2. Cold spray deposition process 47

3.4. Coating characterization 48
3.4.1. Sample preparation 48
3.4.2. Coating properties 49
3.5. Slurry erosion and corrosion testing 51
3.5.1. Slurry erosion test 51
3.5.2. Corrosion tests 53
3.5.3. Wear scar and corrosion damage analysis 54
4. Results 55
4.1. Powder characterization 55
4.1.1. As-received powders 55
4.1.1.1. Oxide reduced WC_{ox} powder 55
4.1.1.2. Agglomerated and sintered WC_{12Co} powder 56
4.1.1.4. Nickel powder 60
4.1.2. Mechanically mixed powders 62
4.2. Parameter optimisation 65
4.2.1. Oxide-reduced WC_{ox}-Ni powders 66
4.2.2. Spherical and agglomerated WC_{12Co}-Ni powders. 67
4.2.3. Spherical and agglomerated WC_{10Ni} -Ni powders 69
4.2.4. Overall summary: Coating thickness and hardness 71
4.2.5. Comparison of the experimental and theoretical coating thickness and hardness results 72
4.3. Coating microstructure and phase analyses 73
4.4. Characterisation of the TiC and Mo-based coatings 78
4.5. Slurry erosion testing 80
4.6. Corrosion testing 83
5. Discussion 87
5.1. Feasibility of the Taguchi Mixed-level DoE technique in the selection of the optimized deposition parameters. 87
5.2. Influence of the feedstock powders on the coating deposition and properties. 90
5.2.1. Microstructure of the cold sprayed coatings 94
5.3.1. Alloying effect 106
5.4. Corrosion properties of cold sprayed WC-Ni based coatings 106
6. Conclusion 110

7. Recommendations..... 112

8. References..... 114

9. Appendix..... 121

List of Figures

Figure 2.1: Summary of various high-temperature thermal spray techniques [2]. 6

Figure 2.2: XRD of WC-12wt%Co (a) feedstock powder and (b) coating [16]. 7

Figure 2.3: Schematic diagram of HVOF deposition technique [31]. 8

Figure 2.4: Schematic illustration of coating build-up mechanism and resultant microstructure of thermal spray coatings [2]. 9

Figure 2.5: Low magnification SEM micrographs of rounded titanium particles sprayed onto a) Armco iron. (b) 86° tilted view of as-sprayed titanium particles. (c) transverse section of the titanium-Armco interface [33]. 10

Figure 2.6: Schematic illustration of gas acceleration obtained by convergent-divergent de Laval nozzle [37]. 12

Figure 2.7: Operating principle of high-pressure and low pressure cold gas dynamic spray systems [19]. 13

Figure 2.8: Window of deposition for CGDS [40]. 16

Figure 2.9: Coating formation of cold sprayed WC-17 wt% Co powders differing in particle morphology [35]. 18

Figure 2.10: Resultant coatings formed from (a-b) high porosity, (c-d) medium porosity and (e-f) low porosity WC-12 wt% Co powders [47]. 20

Figure 2.11: Microstructure of WC-based coatings with feedstock composition of (a) WC-50 wt% Ni, (b) WC-25 wt% Ni, (c) WC-8 wt% Ni and (d) WC-4 wt % Ni [43]. 21

Figure 2.12: Comparison of the WC content in the coating and feedstock powder [43]. 22

Figure 2.13: High magnification images of the WC-Ni MMC coatings fabricated from (a) WC-50 wt% Ni 22

Figure 2.14: SEM micrographs of a) fine WC-Ni powder and b) microstructure of resultant cold sprayed coatings [48]. 23

Figure 2.15: Influence of impact angle on the rate of wear for brittle and ductile materials [52]. 25

Figure 2.16: The formation of Hertzian cracking leading to erosive wear by brittle fracture [53]. 26

Figure 2.17: Dependence of erosion rate on impact angle for soda lime glass eroded by 9 μm and 21 μm silicon carbide particles at 136 $m.s^{-1}$ [49]..... 27

Figure 2.18: Summary of the forms of damage that can occur by plastic erosion [54]. 28

Figure 2.19: Schematic illustration of erosion, 2 and 3 body abrasion wear mechanism [49]. 29

Figure 2.20: A wear mode diagram for abrasive wear of cutting, wedge forming and ploughing [49]..... 29

Figure 2.21: Summary of the forms of damage that can occur by abrasive wear. [54]..... 30

Figure 2.22: Graphs comparing the abrasive wear rate of (a) WC-12wt%Co and (b) WC-17wt%Co coatings produced using HVOF and CGDS [23]. 31

Figure 2.23: Curve of wear rate versus hardness, showing the respective WC content in the coating [56]. 32

Figure 2.24: The effect of binder mean free path on the wear rate of cold sprayed WC-12wt%Co-Ni coatings [56]. 33

Figure 2.25: Schematic diagram for metal corroding in an electrolyte [60]. 34

Figure 2.26: Generic polarization curve illustrating cathodic and anodic reactions [64]..... 35

Figure 2.27: Hypothetical cathodic and anodic polarization plots for a metal undergoing passivation [60]..... 36

Figure 2.28: Schematic illustration of material degradation by erosion-corrosion [66]. 38

Figure 3.1: Morphology of the (a) oxide reduced WC_{ox} powder; agglomerated and sintered (b) WC_{12Co}, (c) WC_{10Ni} and (d) Ni powder. 42

Figure 3.2: Centreline SST Series P low pressure cold spray machine. 48

Figure 3.3: Closest permitted spacing for Vickers indentations where c represents the crack length induced from the indentation [76]. 50

Figure 3.4: a) Slurry jet impingement rig used to conduct erosion tests; b) schematic diagram of the rig's operating mechanism [79]..... 52

Figure 3.5: Autolab corrosion cell used for electrochemical testing. 53

Figure 4.1: FESEM micrographs of as-received oxide reduced WCox powder. 55

Figure 4.2: Particle size distribution of the as-received oxide reduced WC_{ox} powder. 56

Figure 4.3: XRD pattern of the as-received oxide reduced WC_{ox} powder. 56

Figure 4.4: FESEM micrographs of the as-received spherical and agglomerated WC_{12Co} powder. 57

Figure 4.5: XRD pattern of the as-received spherical and agglomerated WC_{12Co} powder. 58

Figure 4.6: Particle size distribution of the as-received spherical and agglomerated WC_{12Co} powder. 58

Figure 4.7: FESEM micrographs of the as-received spherical and agglomerated WC_{10Ni} powder. 59

Figure 4.8: XRD pattern of the as-received spherical and agglomerated WC_{10Ni}. 59

Figure 4.9: Particle size distribution of the as-received spherical and agglomerated WC_{10Ni}. 60

Figure 4.10: FESEM micrographs of the as-received Ni powder. 61

Figure 4.11: XRD pattern of the as-received Ni powder. 62

Figure 4.12: Particle size distribution of the as-received Ni powder. 62

Figure 4.13: SEM micrographs of the milled, oxide reduced a) WC_{ox}-4Ni, b) WC_{ox}-50Ni, c) WC_{12Co}-4Ni, d) WC_{12Co}-50Ni, e) WC_{10Ni} -25Ni and f) WC_{10Ni} -50Ni powders. 63

Figure 4.14: a) Fracture of the oxide reduced WC_{ox} particles; b) smearing of Ni onto the surface of the carbide particles as a result of milling process; c) fractured spherical and agglomerated WC_{12Co} particles; and (d) smeared and embedded Ni particles on the surface of the carbide particles as a resultant of milling process. 65

Figure 4.15: SNR values for the oxide-reduced WC_{ox} powder as a function of a) wt% Ni, b) stagnation pressure, c) temperature and d) standoff distance. 66

Figure 4.16: SNR values for the WC_{12Co} powder as a function of a) wt %Ni, b) stagnation pressure, c) temperature and d) standoff distance. 68

Figure 4.17: Cross section of the deposited as-received WC_{10Ni} coating, indicating the poor coating build-up properties of the powder. 69

Figure 4.18: SNR values for the WC_{10Ni} powder as a function of a) wt %Ni, b) stagnation pressure, c) temperature and d) standoff distance. 70

Figure 4.19: Comparison of the resultant SNR values obtained for coating thickness and coating hardness for each 72

Figure 4.20: XRD patterns of the WC_{ox}-x wt.% Ni parent powders and corresponding coatings. 73

Figure 4.21: XRD patterns of the WC_{12Co}-xNi parent powders and corresponding coatings. 74

Figure 4.22: XRD patterns of the WC_{10Ni}-xNi parent powders and corresponding coatings.. 74

Figure 4.23: Microstructure of (a) WC_{ox}-4Ni, (b) WC_{ox}-10Ni, (c) WC_{ox}-25 Ni, (d) WC_{ox}-50Ni, (e) WC_{12Co}-4Ni, (f) WC_{12Co}-10Ni, (g) WC_{12Co}-25 Ni, (h) WC_{12Co}-50Ni, (i) WC_{10Ni} (as-received), (j) WC_{10Ni} -25Ni and (k) WC_{10Ni}-50 Ni coatings. White phase = WC, light gray phase = Co, dark gray phase = Ni matrix. 75

Figure 4.24: Elemental composition maps of the WC_{ox}-25Ni coating. (a) cross-sectional microstructure, (b) Fe, (c) Ni and (d) W..... 76

Figure 4.25: Elemental composition maps of the WC_{12Co}-25Ni coating. (a) cross-sectional microstructure, (b) Fe, (c) Ni, (d) W and (e) Co. 76

Figure 4.26: Elemental composition maps of WC_{10Ni}-25Ni coating. (a) cross-sectional microstructure. (b) Fe, (c) W and (d)Ni..... 76

Figure 4.27: Microstructure of the resultant a) WC_{ox}-4Ni ; b) WC_{ox}-4Ni-1Mo ; c) WC_{ox}-4Ni-10TiC and d) WC_{ox}-4Ni-1Mo-10TiC coatings compositions. 79

Figure 4.28: XRD patterns of the WC_{ox}-4Ni-1Mo parent powder and corresponding coating. 79

Figure 4.29: XRD patterns of the WC_{ox}-4Ni-10TiC parent powder and corresponding coating. 80

Figure 4.30: XRD patterns of the WC_{ox}-4Ni-1Mo-10TiC parent powder and corresponding coating. 80

Figure 4.31: Cumulative mass loss per unit area of the optimal WC_{ox}-4Ni based coatings. .. 81

Figure 4.32: Average total mass loss per unit area of the optimal WC_{ox}-4Ni based coatings. 81

Figure 4.33: (a) Backscatter and; (b) secondary electron FESEM micrographs of the eroded WC_{ox}-4Ni surface. 82

Figure 4.34: (a) Backscatter and; (b) secondary electron FESEM micrographs of the eroded WC_{ox}-4Ni-10TiC surface..... 82

Figure 4.35: (a) Backscatter and; (b) secondary electron FESEM micrographs of the eroded WC_{ox} -4Ni-1Mo-10TiC surface..... 83

Figure 4.36: OCP plots of the optimal WC_{ox}-4Ni based coatings in tap water at 25°C. 84

Figure 4.37: Polarization plots of optimal WC_{ox}-4Ni based coatings in tap water at 25°C. ... 85

Figure 4.38: Potential vs current density plot of optimal WC_{ox}-4Ni based coatings in tap water at 25°C. 85

Figure 4.39: Current density vs time plots of optimal WC_{ox}-Ni based coatings in tap water at 25°C. 86

Figure 4.40: BSD and SE SEM micrographs of the WC_{ox}-4Ni-10TiC based coating subsequent to corrosion testing. 86

Figure 4.41: BSD and SE SEM micrographs of the WC_{ox} -4Ni-1-Mo-10TiC based coating subsequent to corrosion testing..... 86

Figure 5.1: Schematic diagram of the supersonic impingement zone with the occurrence of bow shock at the substrate [91]. 90

Figure 5.2: Smearing of Ni binder on surface of spherical and agglomerated WC_{12Co} powder as a result of milling process..... 91

Figure 5.3: Cross sections of the as-received (a) WC_{ox}, (b)WC_{12Co} and WC_{10Ni} powder particles. 93

Figure 5.4: SEM micrographs showing elongated and deformed (a) WC_{12Co} and (b)WC_{10Ni} agglomerates within Ni matrix as a result of the high energy impact experienced during deposition..... 94

Figure 5.5: SEM micrographs showing fractured WC_{ox} particles within Ni matrix as a result of the high energy impact experienced during deposition. 94

Figure 5.6: (a)Sintered and crushed powders WC-12 wt.% Co used by Melendez et al. [43] and (b) The WC_{12Co} powders used in the current study to develop the WC-Ni based MMC coatings. 95

Figure 5.7: SEM micrograph of Vickers hardness indent in WC_{ox}-Ni MMC coating illustrating the occurrence of plastic deformation and no Palmqvist cracking required for fracture toughness measurements. 96

Figure 5.8: BSD and SE SEM micrographs of an eroded WC_{ox}-4Ni based coating demonstrating erosive wear by brittle fracture. 97

Figure 5.9: SE SEM micrographs of an eroded WC_{ox} -4Ni based coating with indentation, scratching and crater formation, characteristic of erosive and abrasive wear by plastic deformation. 97

Figure 5.10: Diagram showing forces which act on a particle in contact with a solid surface [49] 98

Figure 5.11: SEM micrograph of SiC erodent particles. 99

Figure 5.12: SiC particle embedded within softer Ni matrix of WC_{ox}-4Ni based coating. 99

Figure 5.13: Illustration of the importance of relative sizes of the particle contact zone and the hard phase regions in the abrasive wear of a two-phase material. In (a) the material responds heterogeneously, whereas in (b) the material responds heterogeneously [49]. 100

Figure 5.14: a) The effect of impact angle on the erosion rate [49], and (b) the stress and strain curves for ductile and brittle materials [95] 101

Figure 5.15: SEM micrographs of the (a) initial and new (b) oxide reduced WC_{ox} powder. 102

Figure 5.16: SEM micrograph of WC_{ox}-4Ni coating illustrating extent of carbide fracture (a) before and (b) after erosion. 103

Figure 5.17: SEM micrograph of the HVOF sprayed WC-Co alloys produced by Ogunmuyiwa [96] 105

Figure 5.18: Cumulative mass loss of (a) HVOF sprayed WC-17Co-10VC coatings [96], and (b) cold sprayed WC_{ox}-4Ni based coatings. 105

List of Tables

Table 2.1: Characteristic parameters of several thermal spray techniques [2]. 7

Table 2.2: Metal ductility series [34]..... 11

Table 2.3 Hypothetical process parameters for the deposition of WC-Co coatings using CGDS spraying. 39

Table 3.1: Composition of the mechanical powder blends. 43

Table 3.2: Cold spray parameters determined using the Taguchi method for each blend. 45

Table 3.3: Recommended spray parameters for the deposition of Ni powder (Centerline SST-N5001) [75]. 45

Table 3.4: L16 orthogonal array matrix with pre-determined combination of input parameters to be tested for the optimisation process. 46

Table 3.5: Grinding and polishing procedure for the cold sprayed coatings..... 49

Table 3.6: Parameter settings used for the slurry erosion tests. 52

Table 4.1: D_{50} of the WC-Ni based powder particles used in the current study. 64

Table 4.2: Summary of optimal spray parameters obtained from Taguchi DOE technique ... 71

Table 4.3: Theoretical predictions vs. experimentally obtained output parameters of optimal powder combinations..... 73

Table 4.4: Summary of the coating corrosion properties. 83

Table 5.1: Corrosion resistance of molybdenum [74]. 108

Abbreviations

Al- Aluminium

CGDS-Cold gas dynamic spraying

Co- Cobalt

CR- Corrosion rate

Cu- Copper

DoE- Design of experiments

E_{corr} -Equilibrium potential

EDS - Energy dispersive X-ray spectroscope

FESEM- Field emission scanning electron microscope

HVOF - High-velocity oxy-fuel

I_{corr} -Equilibrium current

M - Molar

Mo- Molybdenum

Ni- Nickel

OA- Orthogonal Array (OA)

OCP- Open circuit potential (OCP)

R_p - Polarization resistance

SOD- Standoff distance

TiC- Titanium carbide

V-Potential

V_{crit} – Critical velocity

WC- Tungsten carbide

W_2C – Ditungsten carbide

WC_{ox} – Oxide reduced WC

WC_{12Co} - Agglomerated and sintered WC-12 wt% Co

WC_{10Ni} - Agglomerated and sintered WC-10 wt% Ni

Wt – Weight

XRD - X-ray diffraction

1. Introduction

1.1. Research background and motivation

Industrial components such as steel-based pipelines and propellers mainly used in the oil, gas and mining industries are often subjected to extreme solid-particle erosion and corrosion during the transportation of slurries [1]. Such conditions drastically shorten the lifespan of these components which in turn increase production downtime and the costs associated with equipment maintenance [1-2]. These industries therefore continuously seek new ways to curb the premature failures of piping systems by mitigating the adverse effects of slurry erosion and corrosion.

A common solution employed in the piping industry is the application of cemented tungsten carbide, also known as hardmetal [2]. Hardmetal coatings are ideal for numerous wear and corrosion resistance applications, due to the ultra-hard, high strength and chemically resistant nature of the tungsten carbide (WC) compound [2-3]. These coatings are conventionally deposited onto metal substrates using high-temperature deposition techniques, such as high-velocity oxy-fuel (HVOF), plasma transferred arc welding (PTAW) and spray fusion (SF), which require the melting of the powder particles to achieve superior particle-substrate adhesion [2,4-10]. A significant drawback of such techniques is that the elevated temperatures used during deposition typically lead to the formation of hard and brittle phases such as W_2C, W, and WO_3 which are detrimental to the mechanical and wear properties of the coatings [11-13]. The high temperatures also lead to the formation of residual stresses, which, if they are tensile, tend to propagate fatigue cracks within the coatings [14].

In an attempt to mitigate the adverse effects associated with high temperature coating techniques, researchers have investigated alternative, lower temperature techniques for the deposition of WC-based coatings. Cold gas dynamic spraying (CGDS) is an example of such an alternative [15-16]. In this technique, fine, solid powder particulates are accelerated to supersonic speeds (<500 $m.s^{-1}$) using a moving carrier gas and are impacted onto a substrate to form dense coatings [17]. Particle-substrate bonding is achieved through the high pressures generated during impact which allow a ductile material to undergo severe plastic deformation and adiabatic shearing, resulting in material interlocking and mechanical bonding [18]. The cold spray process operates at relatively low temperatures, typically below 600 °C, and

involves limited to no melting during coating deposition [17,19-20]. Consequently, the chemical composition of the coatings remains identical to the feedstock powders.

It is challenging to achieve the adhesion of WC particles using cold spray deposition as the particles tend to shatter upon impact and erode the substrate [15,21]. To overcome this challenge WC is usually co-deposited with ductile metal binders such as Cu, Ni and Al [21]. The addition of a softer, more ductile metal has been demonstrated to improve the deposition efficiency of the carbide particles, unfortunately, at the expense of the hardness properties of the coatings [21]. Albeit the decrease in hardness, a critical advantage of the cold gas dynamic spraying of cemented WC-based coatings over high temperature processes is that the undesirable effects associated with the latter processes, such as phase transformations, high-temperature oxidation and recrystallisation, are prevented. The successful deposition of WC-Co coatings has been achieved using high pressure cold spray systems with coatings having thickness and hardness values comparable to those produced using HVOF processes [15]. These systems are able to achieve a carrier gas flow velocity of 1000 $m.s^{-}1$ [19]. However, the deposition of hardmetal coatings using low pressure CGDS, wherein the maximum carrier gas flow velocity achieved is 600 $m.s^{-}1$, is limited. Some of the advantages of low pressure systems include being more energy efficient, and its ease of cost-effective automation [17, 19, 20-21].

The focus of the current research study was therefore to investigate the feasibility of depositing WC-Ni based coatings using a low pressure CGDS system for possible application to slurry erosion environments such as the piping industry mentioned earlier. Limited studies have been conducted on the wear properties of low pressure cold sprayed WC-based coatings, as the majority of this research is based on coatings deposited using high pressure CGDS systems.

1.2. Research Aims and Objectives

The aim of the current study was to assess the feasibility of using a low pressure cold spray system for the fabrication of WC-Ni-based coatings suitable for slurry erosion protection. The effect of molybdenum (Mo) and titanium carbide (TiC) additions on the wear properties of the WC-Ni coatings was also incorporated into this investigation. A systematic approach to determine the optimal spray parameters for the selected WC-Ni alloy systems deposited using a low-pressure CGDS system, had not yet been conducted and was therefore, a significant

component of the study. The aims of this project were achieved through the following objectives:

- The optimization of the deposition parameters for the selected WC-Ni alloy systems using the Taguchi mixed level design of experiments (DoE) technique.
- The material property characterization of the WC-Ni coatings deposited using a low pressure cold spray system.
- The assessment of the slurry erosion properties of the optimal WC-Ni alloy system.
- The assessment of the effect of Mo and TiC additions on the material and slurry erosion properties of the optimal WC-Ni alloy system.

1.3. Contribution to knowledge

To the author's knowledge, a systematic approach to determine the optimal spray parameters for a WC-Ni alloy system deposited using low pressure CGDS had not been conducted and therefore contributed to the generation of new knowledge. Sliding and abrasive wear studies of cold sprayed WC-Ni based coatings have been conducted; however, the slurry erosion properties of this alloy system had not been documented when the study was initiated. Furthermore, the effect of molybdenum (Mo) and titanium carbide (TiC) additions to the WC-Ni alloy system for improved slurry erosion and corrosion resistance have been documented for HVOF deposited WC-based coatings but not for those deposited by CGDS and was therefore also incorporated into the investigation.

1.4. Layout of research

The structure of this dissertation is as follows: *Chapter 1* presents the background and significance of the research work undertaken. *Chapter 2* reviews published literature on the fabrication of WC-based coatings and the short-comings of the high temperature processes typically employed to manufacture them. The cold gas dynamic spraying of WC-based coatings is then introduced followed by a discussion on the erosion and corrosion properties of these materials. *Chapter 3* provides a detailed account of how the WC-Ni based coatings used in this study were fabricated and assessed for their slurry erosion properties. The results of all the experiments conducted are documented in *Chapter 4* and are discussed in *Chapter 5*. The conclusions drawn from the research work are presented in *Chapter 6*, while *Chapter 7*

provides the recommendations for future work. *Chapter 8* lists all the cited references and all the additional information relevant to this dissertation is presented in the *Appendix*.

1.5. Scope and limitations

The current research only investigated the effect of wt% Ni, deposition temperature, stagnation pressure and gun-substrate stand-off distance (SOD) on the resultant WC-Ni coatings deposited using CGDS. In order to narrow scope of work, it did not consider other deposition parameters such as carrier gas composition, powder feed rate, number of passes and transverse gun speed. An in-depth analysis of the CGDS bonding mechanisms using techniques such as neutron diffraction stress measurements could not be conducted due to a limitation in the number of fabricated coatings. Erosion at lower impact angles, corrosion in other mediums varying in pH and the synergy between the two processes was not investigated, also due to a limitation in coating samples. However, work not covered in the current investigation has been listed in the recommendations section for future investigation.

2. Literature Review

This chapter introduces WC-based coatings; their properties and the high temperature thermal spray techniques conventionally used in industry to deposit them. The concept of cold gas dynamic spraying is then introduced as an alternative to these high temperature techniques. The relevant studies on the CGDS of WC-based coatings previously documented by other researchers are reviewed. The chapter ends with a review of the erosion and corrosion fundamentals of WC based coatings, followed by a brief review on the application of design of experiments methodologies for the optimisation of experimental parameters.

2.1. WC-based coatings

Coatings are typically applied to protect the underlying surface from premature surface damage, wear, corrosion and thermal degradation [1-2]. Tungsten carbide (WC) based coatings are ideal for numerous wear and corrosion resistance applications due to the ultra-hard, high-strength and chemically resistant nature of the compound [3]. Carbide materials are seldom deposited without a softer binder metal to facilitate adhesion and to enhance the final properties of the coatings[3,22]. Cobalt (Co) is the best-known binder metal for high wear resistance performance, as it offers moderate fracture toughness and excellent transverse rapture strength [3]. However, Co has poor corrosion properties, making WC-Co unsuitable for corrosive environments [3,23]. Corrosion resistant metals such as Ni and Cr usually replace or are added to the Co binder system to improve the corrosion resistance of the coatings [24-25].

Research on the tailoring of WC powders suitable for particular applications has been conducted [25-29]. In order to enhance the chemical and mechanical properties of WC based coatings, the carbide grain size and binder content are often optimised [27-29]. Finer carbide grain sizes and lower proportions of the binder metal are conventionally used for applications requiring ultra-high hardness, while larger grain sizes are used for improved fracture toughness and strength [27-29]. Metals such as Vanadium (V) and Niobium (Nb) can be added to the binder system to obtain finer grain sizes, while other carbides such as TiC are added for improved hardness, wear and corrosion resistance [25-29].

2.2. Thermal spraying of WC-based coatings

WC-based coatings are conventionally deposited onto metal substrates using high temperature thermal spray deposition processes. Thermal spray techniques can be divided into four major categories namely, plasma arc, electric arc, flame and kinetic spraying, each with characteristic temperature ranges, velocities and resultant coating properties. High velocity oxy fuel (HVOF), detonation gun and plasma transferred arc welding (PTAW), are examples of these various classes of techniques as summarised in *Figure 2.1* [2].

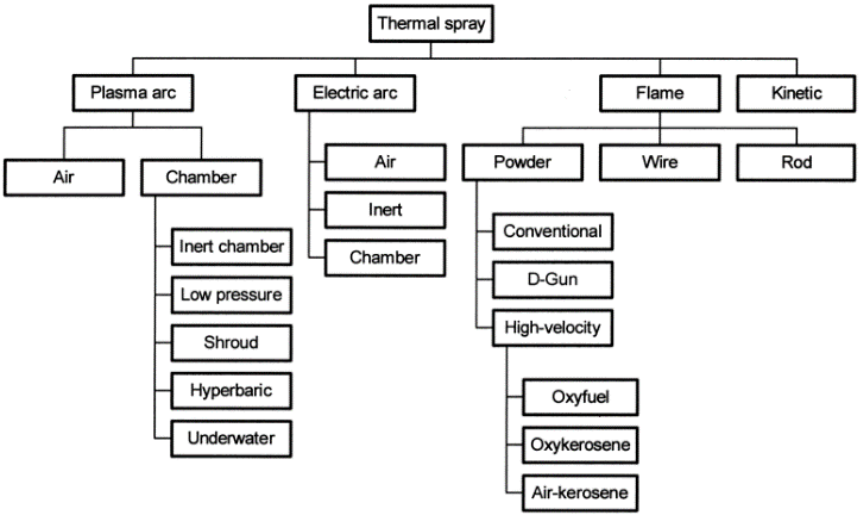

Figure 2.1: Summary of various high-temperature thermal spray techniques [2].

These high temperature processes involve the heating and melting of the high-velocity powder particles, in order to achieve good particle-substrate and particle-particle adhesion [4-10]. The elevated temperatures used during the deposition of WC-Co cemented carbide coatings typically lead to the decomposition of WC and the formation of hard and brittle phases such as W_2C, W, $Co_xW_yC_z$ and WO_3 as illustrated in the X-Ray Diffraction (XRD) patterns of HVOF sprayed WC-Co in *Figure 2.2* [11, 12-13,16]. W_2C (3000 HV [3]), which has been found to have higher hardness and strength compared to WC (1300-2300 HV [3]), is brittle and has been shown to decrease the wear resistance of the coatings [30,11-12]. Stewart et al. [11] reported that the sliding wear resistance of HVOF sprayed coatings decreased with an increase in the decomposition products, especially W_2C [11]. The high temperatures also lead to the formation of residual stresses, which if they are tensile, tend to propagate fatigue cracks within the coatings [14].

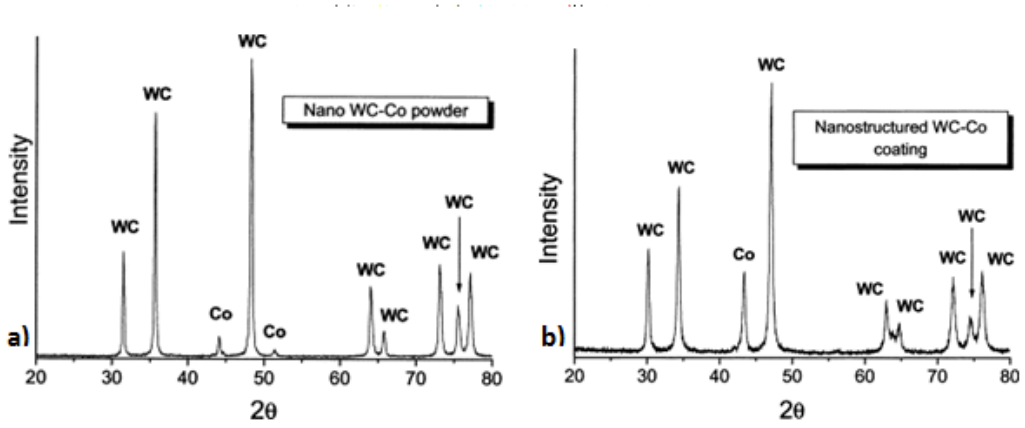

Figure 2.2: XRD of WC-12wt%Co (a) feedstock powder and (b) coating [16].

2.2.1. HVOF deposition of WC-based coatings

HVOF is the most preferred thermal spraying technique for the deposition of WC-based coatings as it has been found to produce superior coatings with the highest carbide retention, low levels of porosity and the least decomposition of WC [2]. This is attributed to the fact that the inflight particles have narrower reaction zones due to the lower process temperatures and higher velocities applied during deposition. WC-Co coatings deposited using HVOF techniques also result in a more uniform distribution of the contact stresses, therefore minimising the severe coating delamination that other methods produce [2]. *Table 2.1* compares some characteristic parameters of several thermal spray techniques.

Table 2.1: Characteristic parameters of several thermal spray techniques [2].

	Wire arc	Plasma	HVOF	CGDS
Jet temperature *K*)	~6000	~13,000	~5500	300–900
Jet velocity (m/s)	50–100	800–1500	1000–2000	1000–2500
Gas	Air, N_2, Ar	Ar, H_2, N_2, He	CH_4, C_3H_6, H_2	Air, N_2, He
Gas flow rates (Nlm)	500–3000	40–150	400–1100	1000–3300
Power (kW)	2–5	40–200	150–300	5–10
Feedstock (g/mn)	150–2000	10–80	15–50	20–80
Deposit density (%)	80–95	90–95	>95	>95

HVOF spraying makes use of combustible gases such as acetylene, propane, propylene, hydrogen; or liquid fuels such as kerosene which are reacted in a combustion chamber, generating temperatures as high as 5000 °C [2,7,31]. The feedstock powder is then injected into the combusted gas using a separate carrier gas stream as depicted in *Figure 2.3* [31]. The combustion of the fuel leads to the partial melting of the inflight particles and also generates the high pressures required to accelerate them to near supersonic velocities before impact with the substrate. The process is able to achieve high-density coatings with superior bond strength and limited oxide inclusions due to the rapid heating and impaction of the inflight particles [2]. Depending on the process parameters used, WC based coatings with thicknesses and hardness values in the range of 500 µm and 1500 HV respectively can be produced, providing sufficient wear and corrosion resistance [8,9,11].

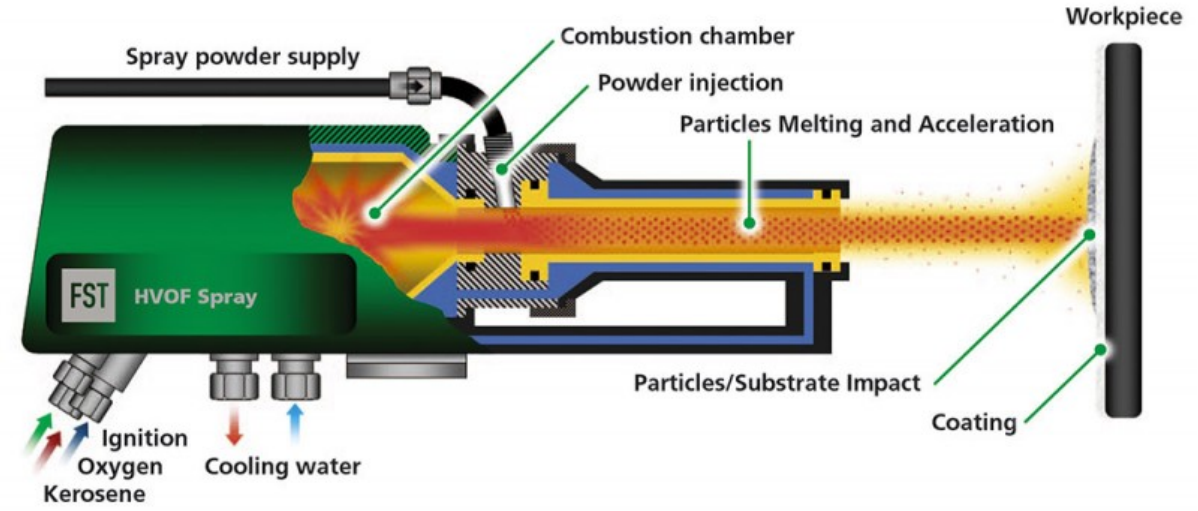

Figure 2.3: Schematic diagram of HVOF deposition technique [31].

The typical microstructure of HVOF thermal spray coatings often includes layers of lamellar (splat), unmelted particles, oxide inclusions, pores and cracks as depicted in *Figure 2.4*, giving rise to anisotropic properties [2].

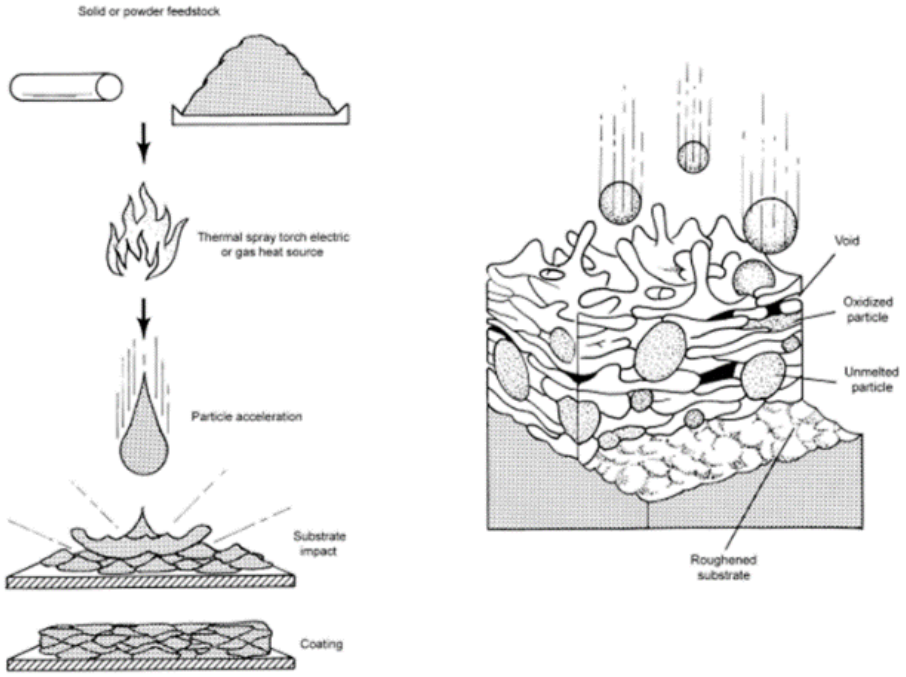

Figure 2.4: Schematic illustration of coating build-up mechanism and resultant microstructure of thermal spray coatings [2].

Splats are the basic building blocks of thermal sprayed coatings. They are formed when the molten inflight particles deform, flatten and solidify upon impact, creating a layered lamellar structure [2]. Oxide inclusions are coating defects which are formed when the molten powder particles react with the environment during flight. Oxidative reactions can be minimised by using inert gases, selecting larger particles to reduce the surface reactivity, or by reducing the temperature and particle dwell time within the carrier gas stream [2]. Pores are formed from material shrinkage, poor splat cohesion, the presence of unmelted particles and inclusions, making coatings susceptible to corrosion, oxidation and wear. In certain instances, oxide inclusions are desirable for improved wear resistance; however, these, together with pores, reduce the cohesive strength of coatings resulting in premature coating failures and reduced coating properties [2]. These coating defects can be minimised by controlling the feedstock powder, optimizing the deposition parameters and applying post-deposition treatments [2].

The resultant microstructure of HVOF deposited WC-Co coatings is dependent on several factors such as the nature and stoichiometry of the combustion fuel, the heat and mass transfer

between the combusted gas and inflight particles, and the properties of the starting powder [7-8]. Sahraoui et al. [8] demonstrated that the selection of the feedstock powder was the most pertinent variable to be optimised for the formation of a superior microstructure with minimal decarburization. It was found that the use of fine WC powder led to the decomposition of the carbide grains and that nanosized grains were more effective in the mitigation of W_2C formation compared to conventional micron-sized WC powders [8]. Reducing the amount of oxygen in the combustion and carrier gas streams was also proven to reduce the decomposition of WC [32].

The heat required to melt the binder often results in the deterioration of the carbide and binder phases by decarburization, phase changes, high temperature oxidation and grain growth which have detrimental effects on the mechanical properties of the coatings as previously discussed [4-10]. In an attempt to minimize the coating degradation effects associated with high-temperature techniques, researchers have been investigating the use of cold gas dynamic spraying (CGDS) as an alternative to the high-temperature deposition of WC-based coatings.

2.3. Cold Gas dynamic spraying

2.3.1. Fundamentals

Cold gas dynamic spraying (CGDS) is a coating deposition technique in which fine, solid powder particulates (1-50 μm in diameter) are accelerated to supersonic speeds (500-1500 $m.s^{-1}$) and are impacted onto a surface at temperatures below the melting points of the powder constituents [17]. The process is solely reliant on the plastic deformation of the powder particles to achieve adhesion with the surface as demonstrated in *Figure 2.5* [17-18,33].

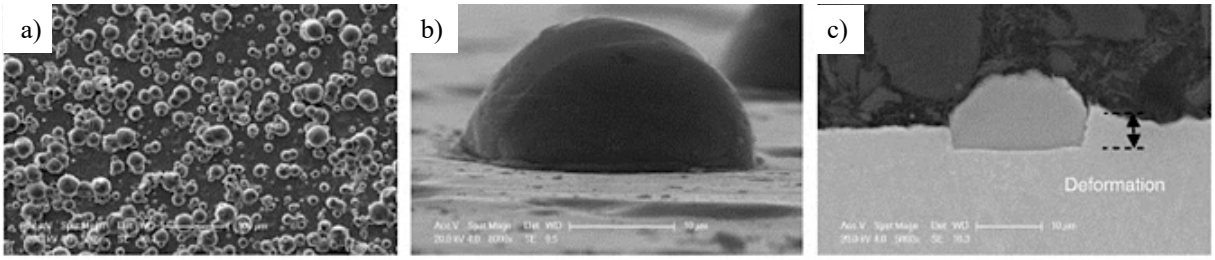

Figure 2.5: Low magnification SEM micrographs of rounded titanium particles sprayed onto a) Armco iron. (b) 86° tilted view of as-sprayed titanium particles. (c) transverse section of the titanium-Armco interface [33].

Cold spraying works best for metallic materials which are ductile and able to deform upon the application of an external stress [17]. Brittle materials such as glass, carbides and ceramics shatter upon impact with the surface and are therefore less suitable for the process [17]. *Table 3.2* [34] presents a summary of the ductility properties of a range of materials, with the most ductile being ideal for cold gas dynamic spraying.

Table 2.2: Metal ductility series [34].

Element		ν	Nanoscale κ	Physical Ductility D
Absolute Limit, Perfect Ductility		1/2	0	1
Gold	Au	0.44	0.08	0.93
Lead	Pb	0.44	0.08	0.93
Niobium	Nb	0.40	0.14	0.82
Palladium	Pd	0.39	0.16	0.80
Platinum	Pt	0.38	0.17	0.76
Silver	Ag	0.37	0.19	0.73
Vanadium	V	0.37	0.19	0.73
Tin	Sn	0.36	0.21	0.69
Aluminum	Al	0.35	0.22	0.65
Copper	Cu	0.34	0.24	0.62
Tantalum	Ta	0.34	0.24	0.62
Titanium	Ti	0.32	0.27	0.54
Nickel	Ni	0.31	0.29	0.50
Cobalt	Co	0.31	0.29	0.50
Magnesium	Mg	0.29	0.33	0.43
Iron	Fe	0.29	0.33	0.43
Tungsten	W	0.28	0.34	0.40
Zinc	Zn	0.25	0.40	0.30
Manganese	Mn	0.23	0.44	0.23
Uranium	U	0.23	0.44	0.23
Silicon	Si	0.22	0.46	0.20
Plutonium	Pu	0.21	0.48	0.18
Chromium	Cr	0.21	0.48	0.18
Carbon	C	0.20	0.50	0.16
Beryllium	Be	0.032	0.91	0.00
Absolute Limit, Total Brittleness		0	1	0



Increase in ductility

Cold spraying is solely a solid-state process in which little to no chemical reactions take place during bonding; as a result, the chemical composition of the coatings generally remains identical to the original powders [16-18]. Entirely dissimilar materials can be bonded using the technique [17]. To date, mismatched materials such as polymers, metals and ceramics have been successfully bonded using cold spraying, making it an attractive process for a variety of applications [17,19,20-21,36]. Examples demonstrating the feasibility of the technique to deposit a range of incompatible materials can be found in literature [19,36]. In a study conducted by Bortolussi et al. [36], PEEK thermoplastic polymer powder mixed with copper powder was successfully deposited onto Carbon Fiber-Reinforced Polymer (CFRP) using this

low-temperature technique [36]. Coatings with superior microstructures and electrical properties were developed and found to be suitable for lightning protection in the transportation industry [36].

Because the process occurs at temperatures below the melting points of the constituents, the deleterious effects such as phase changes, high-temperature oxidation, grain growth, recrystallisation, tensile residual stresses, debonding and gas release associated with thermal spraying methods are therefore eliminated [17,21-22,35-36]. Cold gas spraying is particularly suitable for depositing materials which are highly reactive, sensitive to heat or oxidation such as nano-crystalline powders, aluminium (Al), copper (Cu) and titanium (Ti) [17,21].

2.3.2. CGDS Equipment

The acceleration of the particles is achieved by means of a carrier gas which can be heated to soften, not melt, the particles for better particle-substrate adhesion and to increase particle velocity [17,19,20]. The rapid expansion of the high pressure gas at the convergent/divergent de Laval type nozzle, depicted in *Figure 2.6* [37], produces the conversion of enthalpy into kinetic energy which accelerates the gas flow to supersonic speeds while significantly reducing its temperature and pressure [17,37].

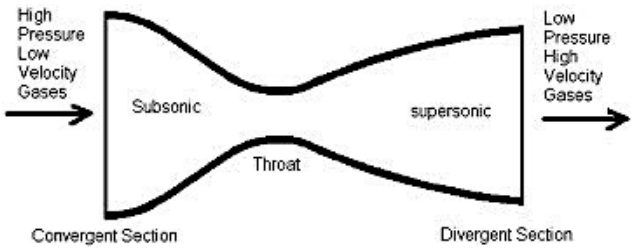

Figure 2.6: Schematic illustration of gas acceleration obtained by convergent-divergent de Laval nozzle [37].

There are currently two types of cold spraying systems that are available in the market, namely high and low pressure cold spraying systems, in which the operational parameters such as pressure, deposition temperature and the carrier gas used differ [17,19]. High pressure systems only use nitrogen or helium as propellant gases as these possess lighter atomic masses in comparison to air and can, therefore, attain higher gas velocities [17,19]. Pressures ranging up to 6895 kPa and gas flow speeds of 1,000 $m.s^{-1}$ can be achieved using these systems. The

powder feedstock is introduced axially into the gas stream, prior to the nozzle throat as illustrated in *Figure 2.7 a* [19]. The propellant gas can also be preheated to temperatures of about 1,000 °C. The heating of the gas in both low and high pressure systems mainly optimises the aerodynamic properties of the propellant gas and does little to increase the deposition temperature of the particles [17]. In low pressure cold spray systems, pressures in the range of 550-965 kPa are used for coating deposition. Air or nitrogen gas can be used as a carrier gas which can also be preheated to about 600℃. The powder feedstock is then introduced downstream in the diverging section and is accelerated toward the substrate as illustrated in *Figure 2.7 b* [19]. The propellant gas with the suspended powder particles is then forced through a DeLaval nozzle, reaching velocities of about 600 $m.s^{-1}$ towards the substrate [17,19].

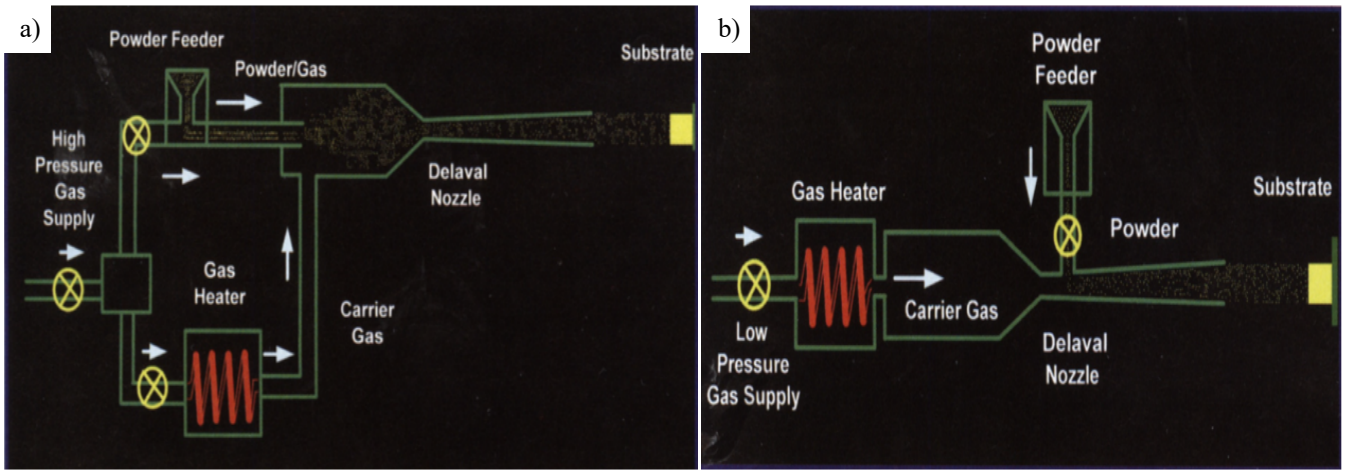

Figure 2.7: Operating principle of high-pressure and low pressure cold gas dynamic spray systems [19].

Low pressure systems are more attractive deposition methods as they considered to be safer, more portable, and easier to automate [17]. The operational costs are also reduced significantly in comparison to high pressure systems as cheaper gas compressors and carrier gases can be utilized. In addition, because the powder particles do not pass through the throat of the nozzle in low pressure systems, the wear of the nozzle walls only occurs in the supersonic portion ensuring a longer service life compared to high pressure CGDS systems [17,19]. The main disadvantage of low pressure systems is that the deposition efficiencies do not exceed 50% in comparison to the 90% achievable in high pressure systems [17]. It is also challenging to achieve the adhesion of less ductile materials using low pressure CGDS systems as the pressures generated are not sufficient to accelerate the particles so that they acquire adequate shearing and deformation required for bonding [17,19].

2.3.3. Deposition mechanism

The mechanism of particle deformation and solid-state adhesion in cold spraying is still not completely understood. Complexities such as the plastic deformation, adiabatic shear instability, material jet formation, impact-induced interface melting, grain refinement and the bonding behaviours of the particles and substrate taking place during impact are still being investigated [17-18,38-40]. To date, researchers have been able to prove that there are two types of bonds that can be identified in CGDS namely:

1. Particle-substrate bonding which is responsible for the formation of the first layer of particles and ultimately determines the adhesive strength of the final coating on the substrate [17-18,38-40].
2. Particle-particle bonding which gives rise to coating build-up and also determines the cohesive strength of the deposit [17-18,38-40].

Researchers have also demonstrated that the formation of a coating is mainly dependent on two factors namely [17-18,38-40]:

1. The kinetic energy of the inflight particles propelled towards the substrate.
2. The ability of particles to deform and adhere to the substrate and on one another during the impaction process.

The kinetic energy of the inflight particles is mainly converted into plastic deformation energy upon impact with the substrate [17-18,38-40]. The formation of bonds can be accounted for by the occurrence of adiabatic shear instability and thermal softening resulting from the high energy impact associated with cold spraying [17-18,38-40]. In thermodynamics, the term adiabatic can be described as the absence of heat transfer with a given system; as a result, the energy generated is therefore retained in that zone where it was created [41]. Shearing is the permanent plastic deformation of a material as a result of the action of a parallel force acting on the material [42]. Adiabatic shearing is, therefore, the severe plastic deformation of a material, occurring almost instantaneously such that there is little to no heat transfer at the point of contact. The lack or the absence of heat transfer leads to localised thermal softening which further enhances atomic diffusion, material mixing and mechanical interlocking, contributing to the bonding mechanisms in cold spraying [17-18]. The material jet formation and the localised severe plastic

deformation is similar to the bonding mechanism observed in cladding and explosive welding processes [17-18,38-39]. In CGDS, the conduction of heat at the points of impact can be neglected due to the short diffusion distances and brief contact times in the order of 10 ns which take place during impact [17]. The high impact energy, as well as the shearing mechanisms, also help to shatter the hard, brittle oxide film surrounding the metallic powder particles and substrate. This enables the pure metal to make intimate contact with the substrate so that excellent adhesion can occur [17-18,38-40].

2.3.3.1. Critical velocity for adhesion

Some of the factors which influence the deposition efficiency of particles include spray parameters, such as gas temperature and pressure, standoff distance (SOD), substrate properties, powder particle size and morphology, and binder content [16-17,40,21]. These process variables also have a significant effect on the critical particle velocity (V_{crit}) which is defined as the minimum velocity required to achieve adhesion. Various empirical equations such as the one presented in *Equation 2.1* have been developed with the aim of determining V_{crit} for each system, however these equations are usually limited to the spraying of pure metals [40].

$$V_{crit} = 667 - 14\rho + 0.08T_m + 0.1\sigma_u - 0.4T_i \qquad \text{Equation 2.1 [40]}$$

Where

ρ - particle density

T_m - particle melting temperature

σ_u - particle material ultimate strength

T_i - particle impact temperature.

Critical impact velocities that are typically observed during cold spraying range between 300 and 1200 $m.s^{-1}$[17]. When the particle impact velocity V_p is too low for a given coating-substrate combination, the feedstock particles act as erodents and rebound from the surface with no deposition taking place [17,21,40]. By varying the process parameters, V_p for a given coating-substrate combination can increase to be equal to or greater than the critical velocity,

in which the particles can deform plastically and adhere to the substrate [21,40]. The influence of particle velocity on the deposition properties further substantiates the theory of a window of deposition as depicted in *Figure 2.8* [40]. Low particle velocities and temperatures typically result in substrate erosion and no coating deposition. At higher parameter settings, in which V_{crit} has been achieved, deposition starts to occur. Further increases in the deposition parameters reintroduces the occurrence of coating erosion, therefore, decreasing the deposition efficiency [17,40].

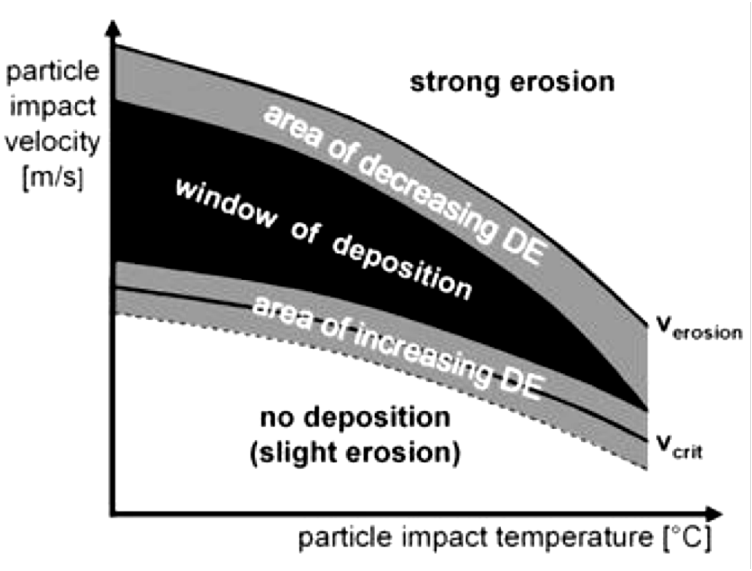

Figure 2.8: Window of deposition for CGDS [40].

2.3.4. Cold gas dynamic spraying of WC

It is generally challenging to deposit WC particles using CGDS, due to its hard and brittle nature. The particles tend to shatter upon impact and may erode the substrate, resulting in an effect similar to activation of the surface or grit blasting [16-17,35]. Since the successful deposition and adhesion of the cold spray coatings is significantly reliant on the plastic deformation of the powder particles, the deposition of carbide materials can be achieved by the addition of a suitable ductile metallic binder [21,43]. Therefore Co, Cu, Ni and Al have been used to co-deposit WC in the form of a cemented carbide or a metal matrix composite [21,43-45]. The purpose of the binder material would be to facilitate the adhesion of the hard WC particles which become embedded in the metal matrix during deposition [17,21,43-45].

Most of the research undertaken on cold sprayed WC-Co based coating has been conducted using high pressure systems which produce dense coatings with thickness and hardness values comparable to those produced by HVOF techniques [35,45]. On the other hand, the impact velocities generated in low pressure systems are not sufficient to cause the adequate shearing and deformation of Co required for bonding [17,21]. To overcome this challenge the WC-Co powders can be co-deposited with more ductile metal binders, such as Cu, Ni and Al, to form metal matrix composite coatings [17,21,43-44]. Wang et al. [21] studied this effect by contrasting the deposition efficiency of mechanically mixed WC-Al and WC-Cu powders with their metal-encapsulated counterparts produced by chemical vapour deposition (CVD). It was found that the encapsulated WC feedstock powders retained higher percentages of the WC phase in the resultant coatings, compared to the mechanically blended powders. The addition of a ductile metal layer around the hard, brittle carbide particles appeared to improve the solid-state particle-to-substrate and particle-to-particle bonding; as a result, the encapsulated hard WC particles behaved like regular soft metal powders during impact [21].

Previous studies indicate that the morphology of the starting WC-Co power is vital to the deposition and mechanical properties of the resultant coatings [35,44]. Ang et al. [35] studied the effect of powder particle size on the deposition efficiency of WC using helium (1450 kPa) as a carrier gas. Three WC-17 wt% Co powders, differing in particle size and morphology, were cold sprayed onto mild steel substrates using a high pressure system. A coarse-grained powder (PM17) with a grain size of 2-3 μm, and two nano-structured WC-17 wt% Co powders (IN17 and BN17) with grain sizes of 40-700 nm and 80-800 nm respectively, were used in the study. It was found that the nano-sized particles had superior deposition efficiencies, and formed coatings with higher hardness values, and fewer pores and cracks. The mechanism of deposition of the three powders is depicted in *Figure 2.9* [35]. The coating thickness of the PM17 powder was limited to about 20 μm; however, the nanostructured IN17 and BN17 powders achieved coating thicknesses greater than 500 μm. The lack of coating build-up of the PM17 powder was attributed to the morphology of the large WC particle size which enhanced the erosion of the coating layers compared to the two nano-structured powders. In such instances, a higher content of Co binder phase is required to facilitate the coating adhesion and limit coating-substrate erosion [35].

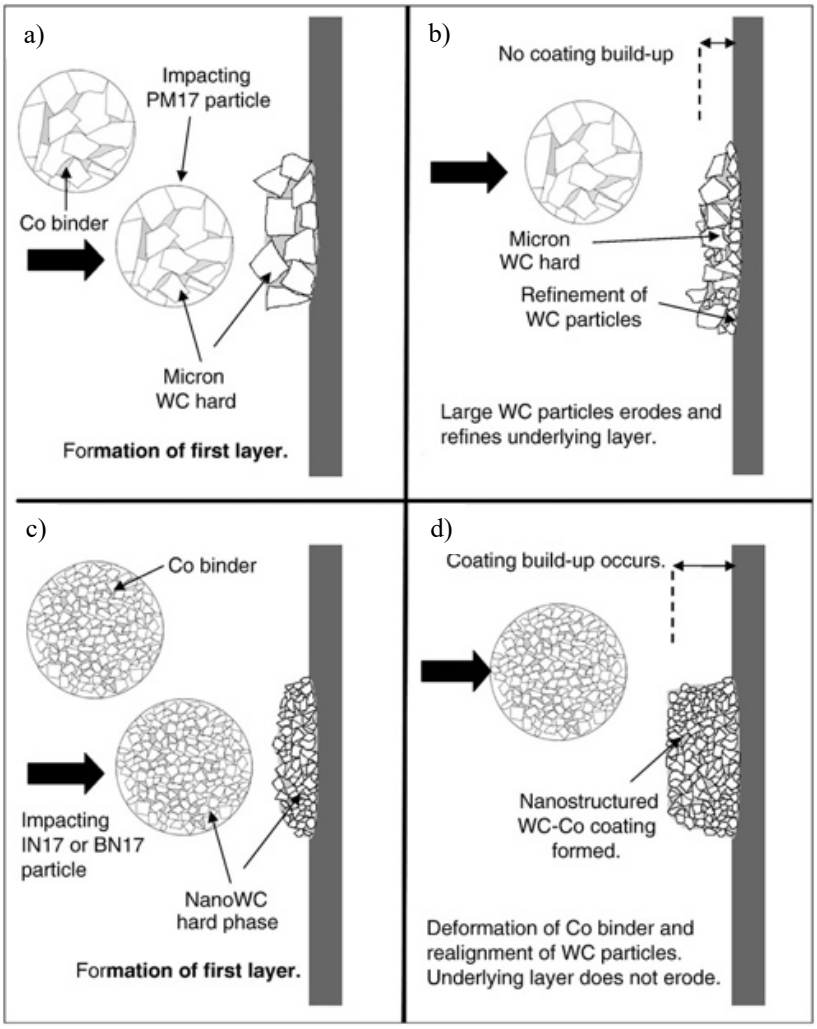

Figure 2.9: Coating formation of cold sprayed WC-17 wt% Co powders differing in particle morphology [35].

No evidence of decarburization or phase changes was observed in the resultant coatings; however, the micron-sized PM17 particles underwent particle refinement upon impact with the substrate [35]. The occurrence of grain refinement was evident from the diffraction peaks of the WC-Co coatings that had broadened significantly compared to the patterns obtained for the feedstock powder. The nano-structured IN17 and BN17 powders, on the other hand, underwent particle refinement to a lesser extent. Similar studies conducted by Kim et al. [15] also demonstrated that nanosized WC-Co particles were more advantageous over micro-sized ones as they were able to fabricate coatings with low porosity, high hardness (2050 HV) and thickness (900 μm) properties. Nanoscale particles were also able to lower the critical velocity required for the build-up of the cold spray coatings compared to the micro-sized WC particles [35].

The porosity of the parent powders also plays a significant role in the deposition behaviour of WC-Co powders [44,47]. Gao et al. [47] investigated the effect of feedstock porosity on WC-Co coatings deposited using a high pressure CGDS system. Three nano-structured, agglomerated and sintered WC-12 wt% Co powders, differing in porosity were used for the study; the high (HP), medium (MP) and low porosity (LP) powders had porosity levels of 43.8 %, 29.8 % and 4.9 % respectively. The study revealed that a certain degree of powder deformability is required to deposit the hard WC-Co cermet coatings [47]. The HP particles experienced extensive deformation upon impact, as presented in *Figure 2.10 a-b* [47], due to their porous structure which facilitated adhesion and coating build-up. The LP particles suffered less deformation during impact, thereby decreasing their deposition efficiency as seen in *Figure 2.11 e-f* [47]. Both the HP and MP powders were able to deposit thick coatings, compared to the thin coatings formed by the LP powders. The study demonstrates that cermet powder particles, therefore, need to be carefully designed to enable a certain degree of deformability during CGDS. Even though porosity is required, the particles should also possess sufficient cohesive strength to minimise the disintegration of the particles during flight or impact [47].

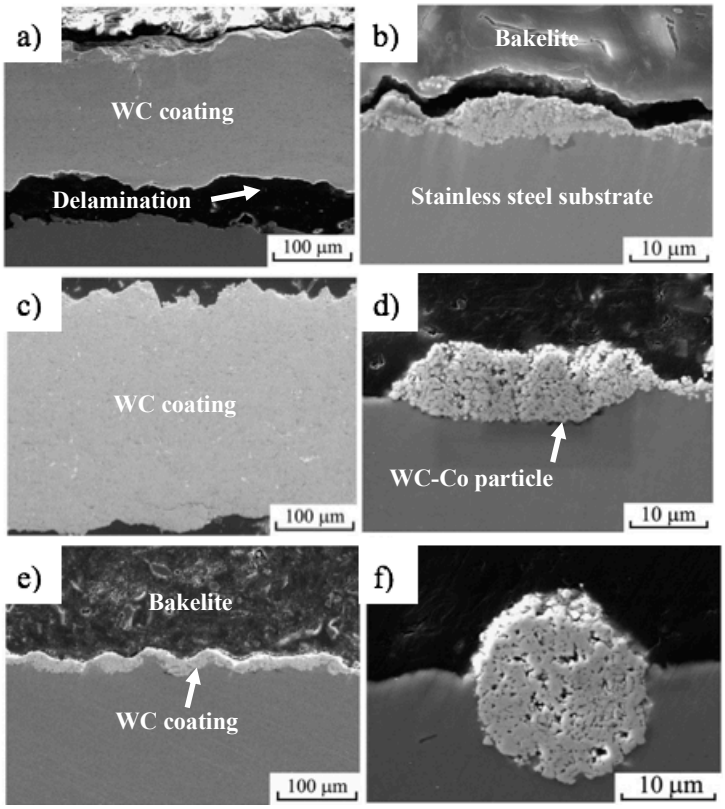

Figure 2.10: Resultant WC-12 wt% Co coatings formed from (a-b) high porosity powders demonstrating powder disintegration and lack of coating adhesion, (c-d) medium porosity powders demonstrating powder deformation and coating build-up and (e-f) low porosity powders demonstrating less powder deformation and coating build-up [47].

The binder content of the WC-Co powders also plays a significant role in the deposition efficiency of the carbide particles for both low and high pressure systems. Melendez et al. [43] used a low pressure system to successfully deposit sintered and crushed WC-12 wt% Co powders mechanically mixed with varying amounts of Ni to form dense coatings (*Figure 2.11*) [43].

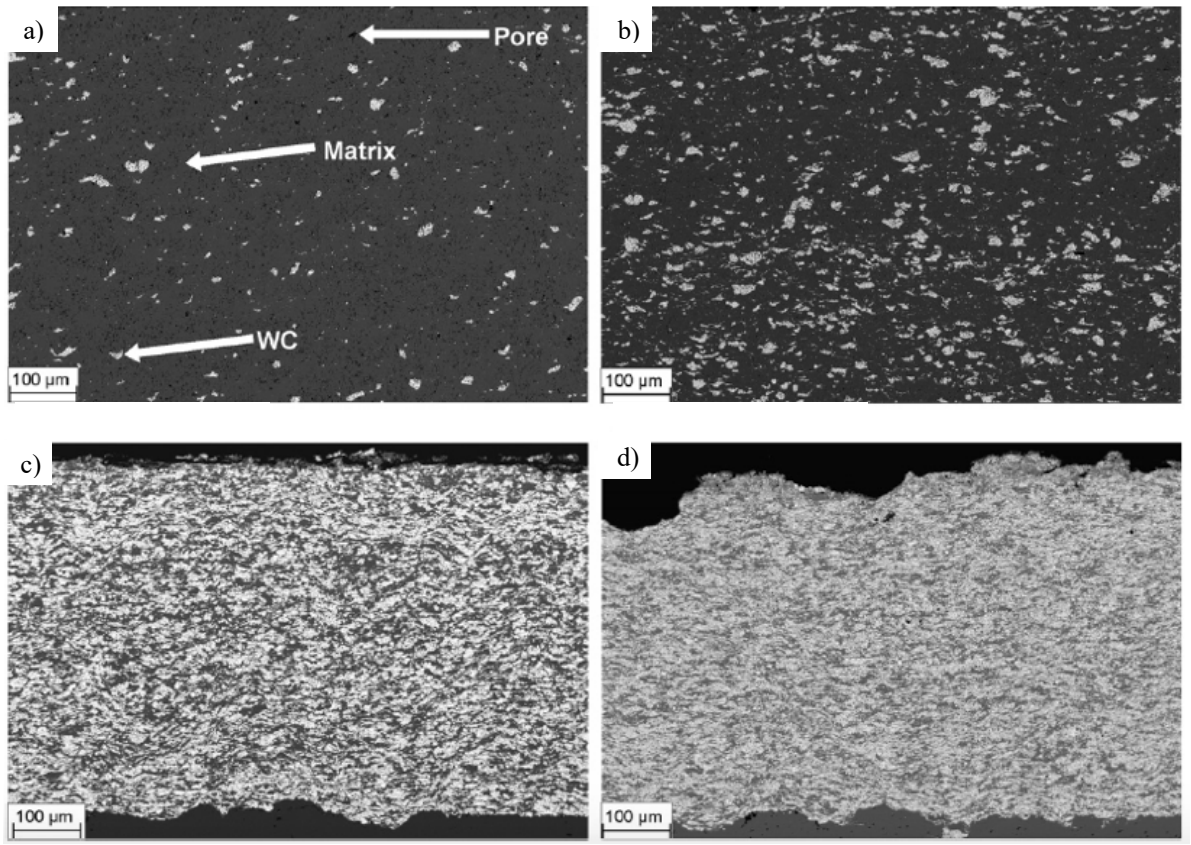

Figure 2.11: Microstructure of WC-based coatings with feedstock composition of (a) WC-50 wt% Ni, (b) WC-25 wt% Ni, (c) WC-8 wt% Ni and (d) WC-4 wt % Ni [43]. Bright phase = WC, grey phase = Ni, dark phase = porosity.

The content of WC in the resultant coatings was then compared to that of the mechanically blended parent powders. The authors found a non-linear increase in the WC retained within the coating as the wt. %WC in the parent powders increased, as illustrated in *Figure 2.12* [43] . It was noted that the WC-12 wt% Co particles were inhomogeneously distributed in the coatings, as some areas were rich in Ni, while other areas had high concentrations of WC grains as seen in *Figure 2.13* [43]. The inhomogeneous structure can be attributed to the difference in the deposition characteristics of the constituent powders. Nickel was preferentially deposited compared to the WC-12 wt% Co particles, due to its softer, more ductile nature.

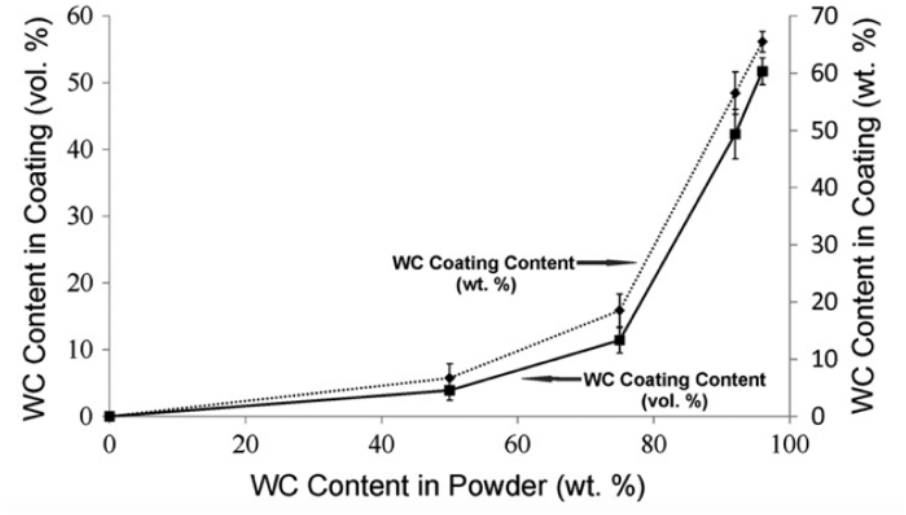

Figure 2.12: Comparison of the WC content in the coating and feedstock powder [43].

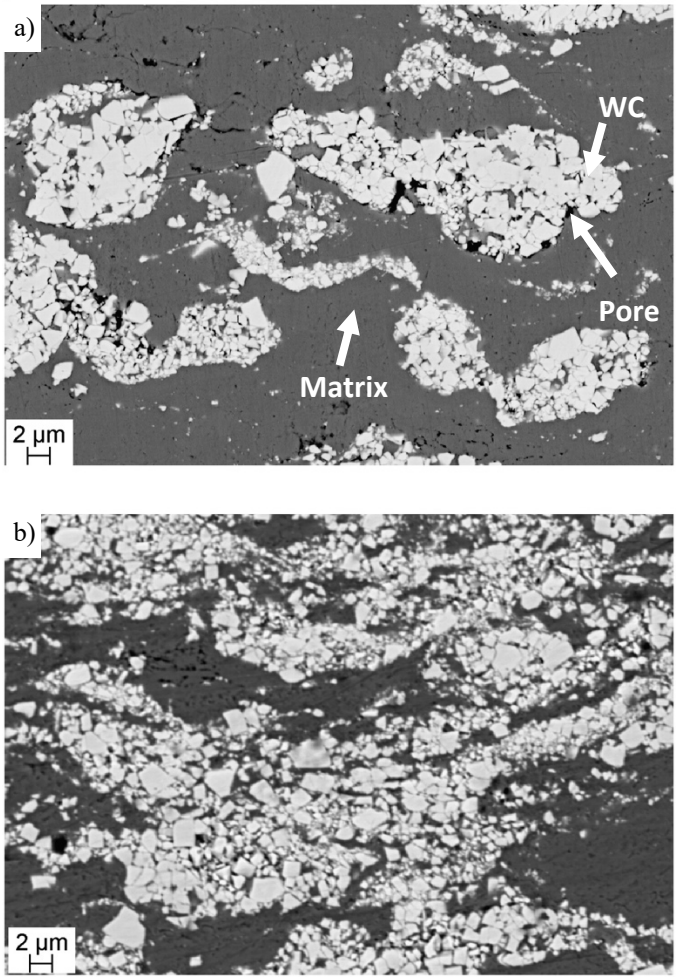

Figure 2.13: High magnification images of the WC-Ni MMC coatings fabricated from (a) WC-50 wt% Ni and (b) WC-4 wt% Ni powder combinations [43].

A higher WC content in the feedstock powder was found to decrease the porosity of the final coating, which was attributed to the impact action of the hard WC particles during deposition[43-44]. Coatings with a maximum hardness of 533 $HV_{0.3}$ and carbide retention of approximately 65 wt. % (see *Figure 2.12* [43]) were achieved for the WC-4 wt% Ni composition produced by Melendez [41]. Nunthavarawong et al. [48] was able to achieve even higher coating hardness values (planar and transverse hardness were 468 and 626 $HV_{0.3}$ respectively) by making use of fine grain WC-5 wt% Ni powders (– 0 + 4 µm) illustrated in *Figure 2.14* [48].

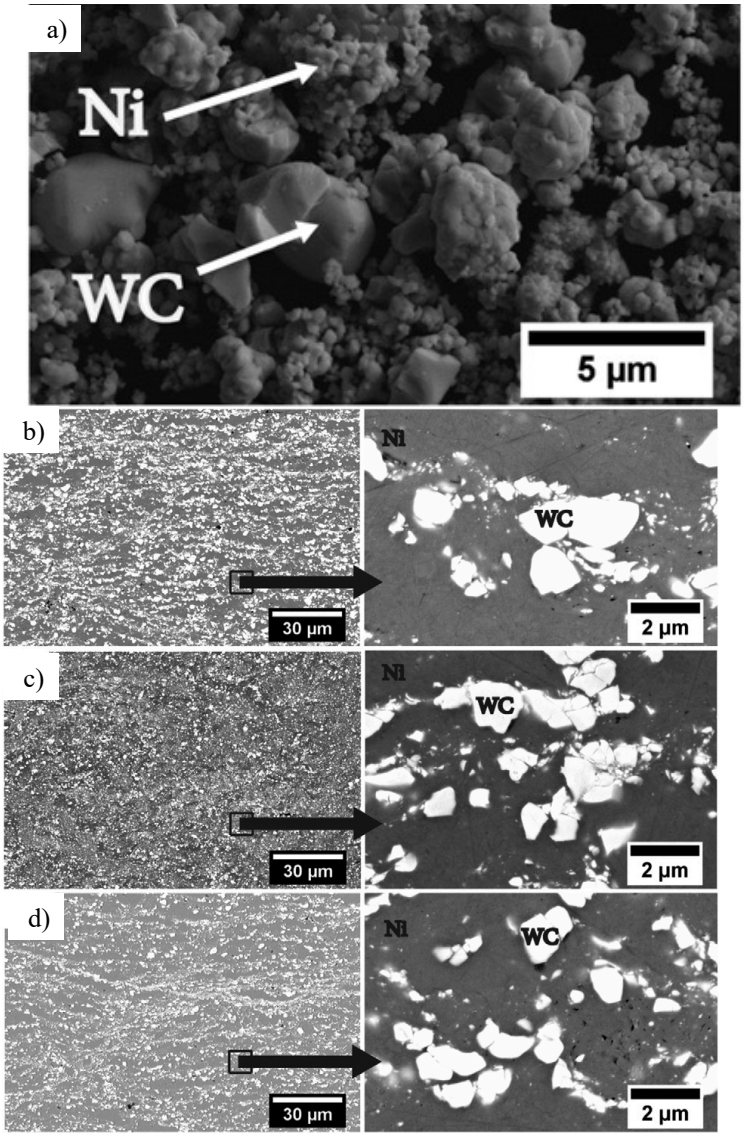

Figure 2.14: SEM micrographs of a) fine WC-5 wt% Ni powder; microstructure of resultant cold sprayed coatings at powder feed rates of (b) 50% (c) 75% and (d) 100%. Bright phase = WC, grey phase = Ni, dark phase = porosity. [48].

2.4. Wear fundamentals

Wear is defined as the progressive deformation and the subsequent removal of material as a result of the interaction of two surfaces moving relative to one another [49]. In material finishing operations such as sandblasting and polishing, wear is desirable [49]. However, in many cases wear leads to an increase in maintenance and repairs, mechanical failure and power consumption [49-51]. Wear resistance is not an intrinsic property of a material as it depends on the operating tribological system [49]. In general, factors such as the properties of the interacting materials, the presence and size of any abradants within the tribosystem, operating conditions, and the environment determine the wear mechanisms [49].

The wear process occurs in 3 different stages namely the primary stage in which the surfaces adapt to one another, and the wear rate is relatively low; the secondary stage which primarily determines the operational life of the components in contact and the tertiary stage where the component fails rapidly [49]. The secondary stage is shortened by conditions within the tribosystem which accelerate the wear process such as the presence of hard abradants, an increase in the applied normal load and high temperatures, etc. There are a variety of wear mechanisms which can take place namely, erosion, adhesive, abrasive, sliding, fretting and corrosive wear [49]. Wear mechanisms do not always act independently; often two or more modes of wear can take place simultaneously [49]. In the current investigation, the major wear mechanism for the WC-based coatings will be slurry erosive wear which may also display characteristics of abrasive and corrosive wear [49].

2.4.1. Slurry erosion

Erosion is caused when discrete hard particles, carried by either a gas or liquid stream, strike the surface of a material leading to damage [49]. If the hard particles are carried by a fluid, for example the transportation of sand water within a pipeline, the mode of wear is known as slurry erosion. Several factors influence the slurry erosion resistance of materials. These include the erodent properties, such as shape, hardness, size and impact angle, the slurry medium, the velocity of the medium and the properties of the counter surface [49]. The wear rate of a material is strongly dependent on the shape of the erodent which has the ability to increase the rate of material removal by a factor of ten or more. Studies quantifying and correlating particle angularity to the wear rate have been conducted [49]. Angular particles generally cause more

damage than spherical ones. Rounded particles lead to less localised deformation, and more impacts are therefore required to remove each fragment of debris [49]. Smaller particles cause less wear than larger particles, with particles between the range of 5 and 500 μm leading to the most amount of damage [49].

The impact angle of the erodent also influences the nature and extent of the damage caused to the surface of the materials. Ductile materials tend to experience peak erosion rates at impact angles of 20-30° and are usually most resistant to erosion at impact angles of 90° [49]. Low impact angles maximise the shear stresses encountered by a surface, leading to high levels of plastic deformation and material damage. Higher impact angles lead to excessive strain hardening due to the material's ability to deform and absorb energy upon the impact of the hard particles. On the contrary, brittle materials experience peak erosion rates at an impact angle of 90° as they have a limited ability to deform and absorb the impact energy before fracture. The normal load and impact energy of the erodent are minimised at lower angles, resulting in reduced wear rates by brittle fracture. The relationship between the erosion rate and impact angle of brittle and ductile materials is summarised in *Figure 2.15* [52].

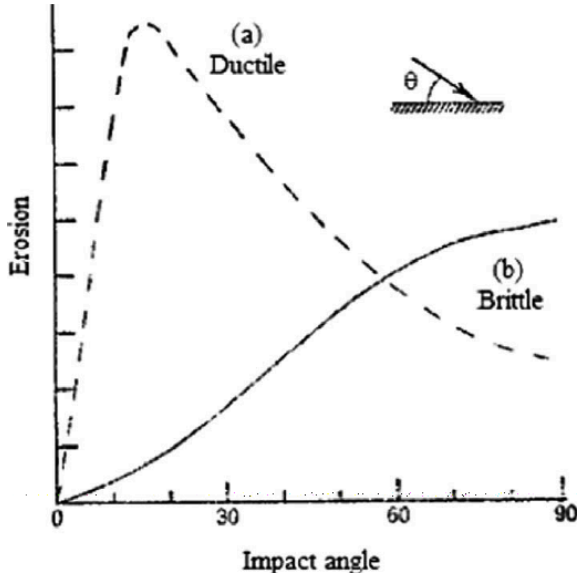

Figure 2.15: Influence of impact angle on the erosion rate for brittle and ductile materials [52].

2.4.1.1. Slurry erosion mechanism

Erosive wear of materials can induce plastic deformation and/or brittle fracture damage mechanisms. Erosion by brittle fracture is characterised by the occurrence of severe cracking, grain pullout and debris formation [49]. Models for material removal by brittle erosion are based on the formation and intersection of Hertzian cracks, leading to fracture as depicted in *Figure 2.16* [53].

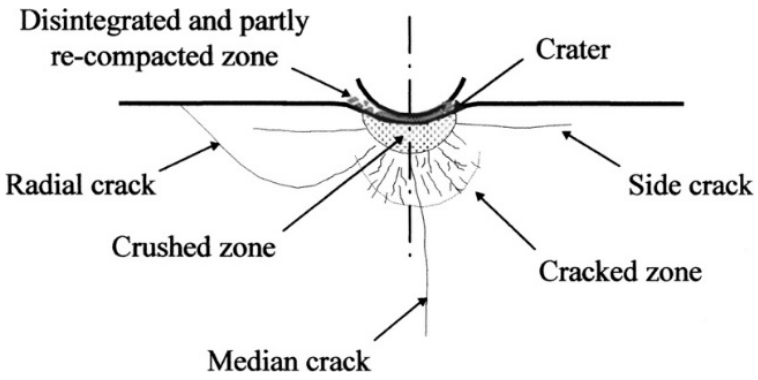

Figure 2.16: The formation of Hertzian cracking leading to erosive wear by brittle fracture [53].

Hertzian cone cracks are formed when a spherical particle is indented onto the plane surface of a brittle material at an angle of 90°. Side and radial cracks are formed when the applied normal load exceeds a critical value, which depends on the fracture toughness and hardness of the material (See *Equation 2.2* [49]). The volume of material removal is then calculated using the contact force and the depths of the side cracks formed.

$$\boldsymbol{w} \propto \left(\frac{\boldsymbol{K_c}}{\boldsymbol{H}}\right)^{\boldsymbol{3}} \boldsymbol{K_c} \qquad \text{Equation 2.2 [49]}$$

Where

w is the volume of material removed
K_c and H are the fracture toughness and hardness of the material respectively.

Angular and small particles lead to more plastic fracture. Studies have indicated that if the erodent particles are sufficiently small, the load carried by each particle may be below the threshold *w* needed to cause cracking. Below this threshold, the hard particles will only cause plastic deformation and wear will occur by plastic processes. This phenomenon is illustrated in *Figure 2.17* [49] in which lime glass, a material conventionally thought of as brittle,

displayed erosion by plastic deformation upon impact with small particles. Higher loads and larger particle lead to the reversion of brittle fracture and higher wear rates [47,52]

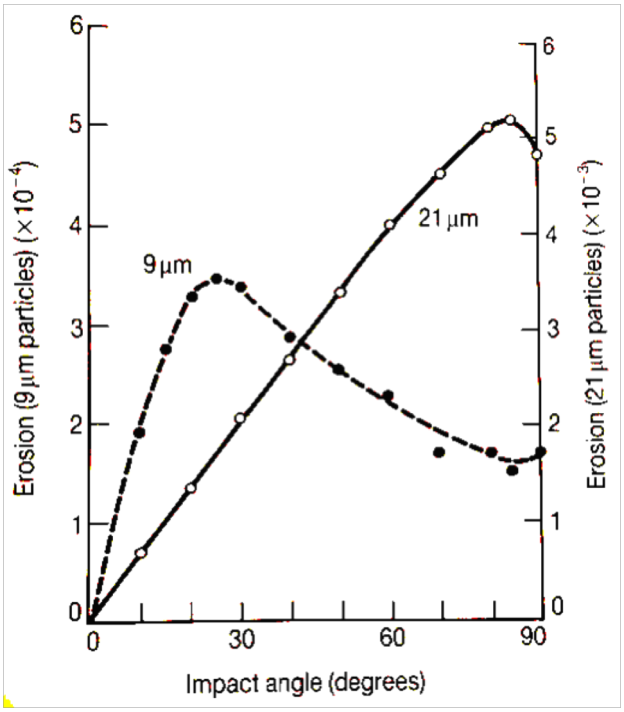

Figure 2.17: Dependence of erosion rate on impact angle for soda lime glass eroded by 9 µm and 21 µm silicon carbide particles at 136 $m.s^{-1}$ [49]

The classification of erosion by plastic deformation is also complex due to the occurrence of several types of damage that can be caused by the erodents. Depending on the shape and angle of the erodent, the following types of damage can occur, as summarised in *Figure 2.18* [54]:

1. *Crater formation*. This occurs when rounded particles deform the surface by displacing the material to the side and the front of the erodent. Further impacts on neighbouring areas lead to the detachment of the heavily strained material from the rim of the crater or the terminal lip.
2. *Type I Cutting* occurs when the erodent particles roll forward, indenting the surface and raising the material into a prominent flake. The raised material is more vulnerable to removal by subsequent nearby impacts.
3. *Type II Cutting* is less prominent and occurs when the erodent particle rolls backwards. A true machining action can occur in which the sharp corner of the erodent cuts a chip away from the surface. However, this type of deformation only occurs over a narrow range of particle geometries and impact angle [49,54].

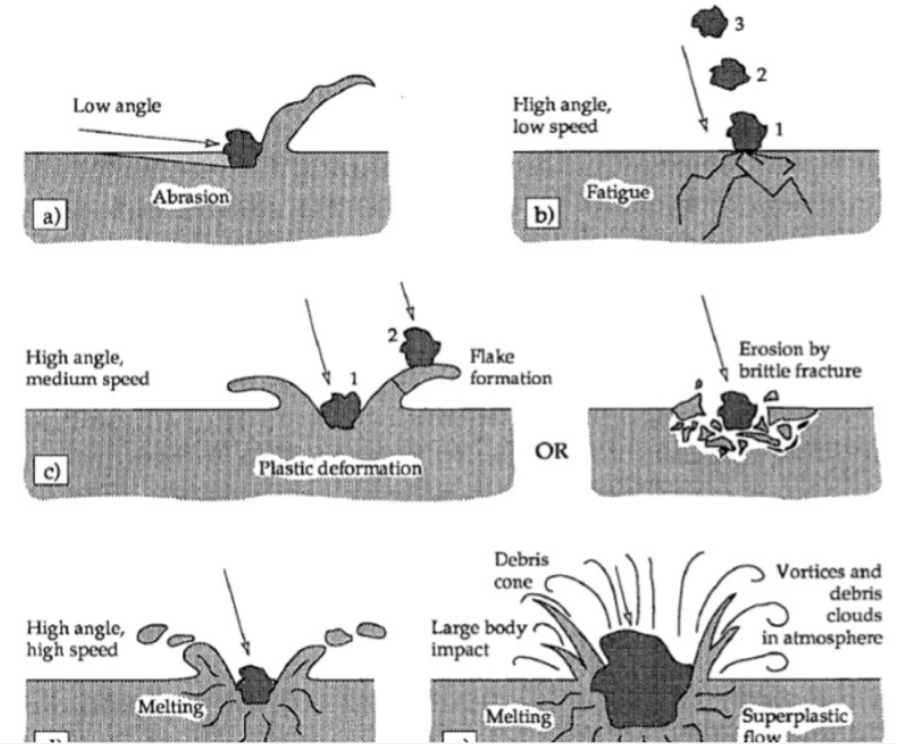

Figure 2.18: Summary of the forms of damage that can occur by plastic erosion [54].

Models on the mechanism of erosion by plastic flow and brittle fracture have been proposed. These calculations are mostly complex and are not always representative of the true mechanism of erosion as a combination of two or more wear modes can take place simultaneously. These models predict that the hardness of the surface is the primary determinant for erosion by plastic deformation, while fracture toughness is more important for brittle erosion [49]. The models also assume that the eroded materials are homogenous and isotropic; however, many engineering materials such as composites, ceramics and cemented carbides, are composed of multiple phases materials which significantly impacts the type and extent of wear taking place [49].

2.4.2. Abrasion

Upon impact with the surface, the flow of the slurry medium may lead to the lateral movement of the erodents which then leads to a 2-body-abrasion wear mechanism. Abrasion is defined as the loss of material due to interfacial hard particles or hard surface protuberances that are forced against and move along a solid surface [49].The difference between erosion and 2-body abrasion is depicted in *Figure 2.19* [49].

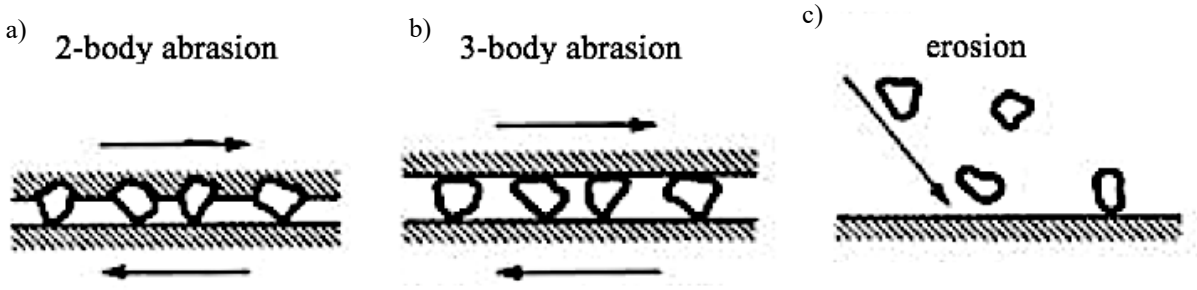

Figure 2.19: Schematic illustration of a) 2-body erosion 2, b) 3-body abrasion and c) erosion wear mechanisms [49].

Similarly to erosion, abrasive wear can occur by plastic deformation, brittle fracture or a combination of the two modes. Three distinct modes of plastic deformation due to the sliding action of a hard particle over the surface can occur as depicted in *Figure 2.20* [49,54] namely:

1. *Ploughing*. A shallow groove is formed on the surface of the material, and repeated loading is necessary to indent the surface.
2. *Microcutting*. The material flows up the front face of the particle and is removed in the form a chip, generating long, curled ribbon-like particles as wear debris.
3. *Wedge formation* is an intermediate between the two extreme modes. The ridge of the deformed material is pushed along ahead of the particle in the same way that a wrinkle can be pushed along a piece of cloth lying on a table.

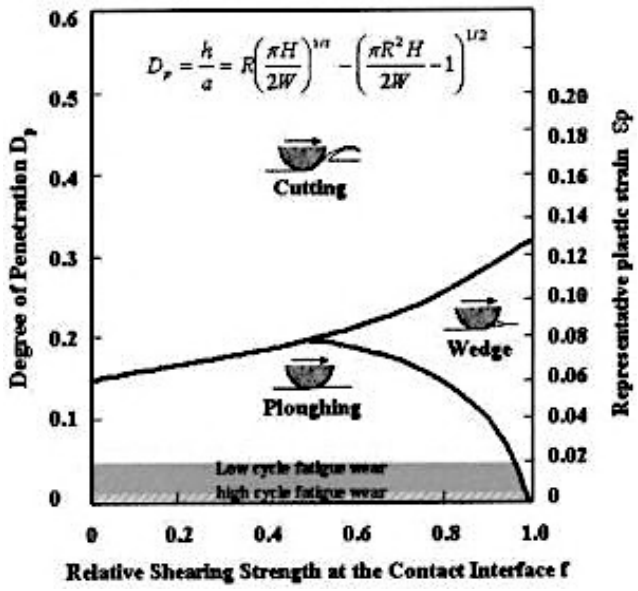

Figure 2.20: A wear mode diagram for abrasive wear of cutting, wedge forming and ploughing [49].

Abrasion by brittle fracture occurs by the formation and coalescence of Hertzian cone cracks on the plane surface of a brittle material [49,54]. As the sliding of the abrasive particle proceeds and grain pull-out occurs (see *Figure 2.21 d* [54]), the generated wear debris can accumulate between the two surfaces and act as third bodies thereby changing the system into a 3-body-abrasion wear mechanism [49].

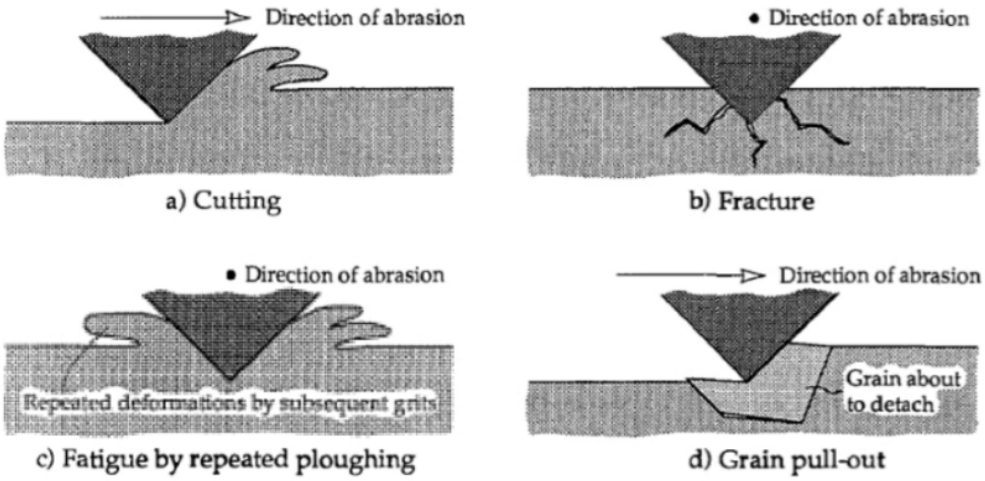

Figure 2.21: Summary of the forms of damage that can occur by abrasive wear. [54]

2.5. Wear of cold sprayed coatings

Various authors have demonstrated the feasibility of using high and low pressure CGDS to deposit wear resistant WC-based coatings. Both systems are able to form coatings with abrasion and sliding wear resistances comparable to and sometimes higher than those produced by high temperature HVOF spray techniques [11-12, 45-56].

Couto et al. [23] performed a comparative study between WC-12 wt% Co and WC-17 wt% Co coatings deposited by HVOF and CGDS. Although the HVOF WC-12 wt% Co and WC-17 wt% Co coatings possessed higher hardness values of 1536 $HV_{0.3}$ and 1379 $HV_{0.3}$ respectively, compared to the CGDS coatings (1419 and 1223 $HV_{0.3}$), the cold sprayed coatings had higher abrasive wear resistances, as illustrated in *Figure 2.22* [23]. Similar results were also observed for the sliding wear tests. The WC-12 wt% Co HVOF coatings had a volume loss of 0.00929 mm^3 while the CGDS coatings had a lower volume loss of 0.0038 mm^3. Similarly, the material volume loss of the WC-17 wt% Co CGDS coatings was 0.0086 mm^3 compared to the material

volume loss of 0.03041 mm^3 observed for the HVOF coatings. The main reason cited for these differences was that cold spraying did not produce the decarburization or dissolution typical observed during the high-temperature HVOF technique which produces the brittle W_2C phase detrimental to the wear resistance of the coatings [23].

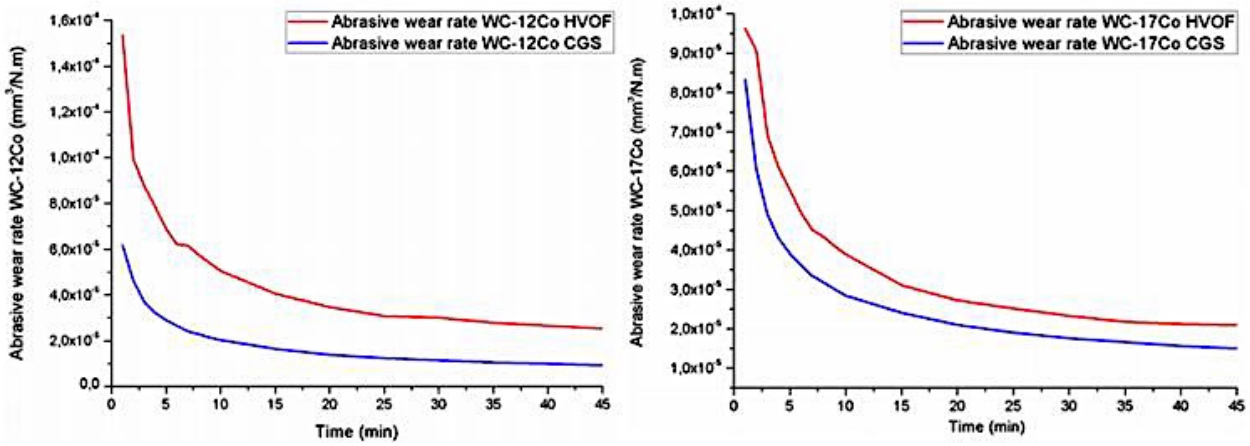

Figure 2.22: Graphs comparing the abrasive wear rate of (a) WC-12wt%Co and (b) WC-17wt%Co coatings produced using HVOF and CGDS [23].

Melendez et al. [56] studied the dry abrasion wear of WC-12 wt% Co-Ni coatings deposited onto low carbon steel substrates using a low-pressure CGDS system. From the study, it was found that as the hardness and the percentage of WC retained within the coating increased, the wear rate consequently decreased. The relationship between hardness and wear rate for the coatings was almost linear, as seen in *Figure 2.23* [56] suggesting that hardness contributed significantly to the abrasive wear resistance [56]. Although hardness is typically used as a first-order approximation of wear rate for WC-based materials, carbide grain size and binder content have been shown to have an impact on the wear resistance [57].

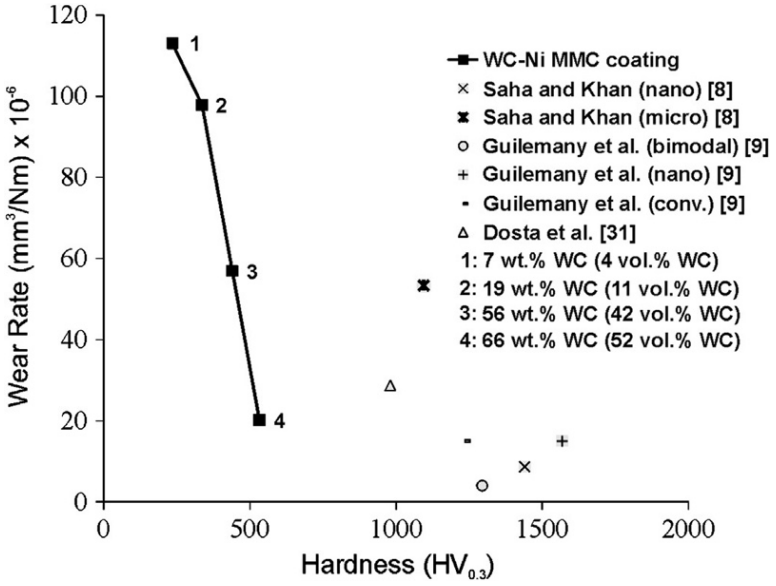

Figure 2.23: Curve of wear rate versus hardness, showing the respective WC content in the coating [56].

The authors also compared the wear rates of the cold sprayed coating with the highest retained WC content of 66 wt % to HVOF sprayed WC-Co coatings with 83 wt. % retained WC. Once again, the same trend observed by previous authors was found here; The CGDS coatings had better wear resistances compared to the HVOF coatings, despite the higher hardness of the HVOF coatings (1100 HV compared to 533 HV). This was attributed to the negative impact of WC decarburization as a result of the high-temperature process. The ductility and toughness of the cold sprayed WC-Ni matrix also contributed to the improved wear resistance. The WC particles reinforced the coating, minimising the damage to the surface of the coatings. The binder mean free path, which dictates the distance between the reinforcing WC particles within the metallic matrix, may be used to describe the mechanical properties of WC-based coatings. Such a correlation was conducted by Melendez et al. [56] who used the Ni mean free path to explain the changes in the wear rate of the WC-12wt% Co-Ni coatings. The authors found that the wear rate of the coatings decreased significantly as the mean free path between the WC-based reinforcing particles shortened, as illustrated in *Figure 2.24* [56]. The primary wear mechanism observed was the plastic deformation of the soft Ni matrix, while the hard WC particles appeared to remain undamaged [56].

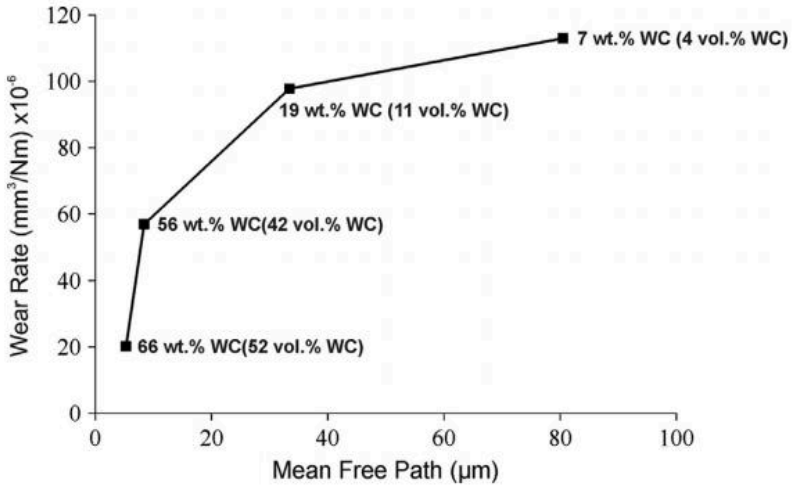

Figure 2.24: The effect of binder mean free path on the wear rate of cold sprayed WC-12wt%Co-Ni coatings [56].

Dosta et al. [45] performed ball-on-disk and dry abrasion tests on WC-25 wt% Co coatings deposited onto carbon steel and Al7075-T6 substrates, using a high-pressure CGDS system. The abrasion tests showed that the uniform WC particle size and the distribution of the carbide particles within the metallic Co matrix resulted in highly abrasion resistant coatings. Low sliding wear rates were observed for both coatings; the wear mechanism identified was the non-uniform extraction of some WC particles from the matrix. The remaining carbides embedded within the Co matrix maintained their wear resistance function, leading to low wear rates. The Energy Dispersion Spectroscopy (EDS) analysis of the debris detected at the edges of the wear tracks confirmed the presence of oxides which were formed as a result of the high temperatures reached during sliding. The presence of oxides may have led to a lubricating effect, therefore decreasing the wear rates, and/or they could have resulted in 3-body abrasion [45,49] .

2.6. Corrosion fundamentals

The chemical nature and velocity of the slurry medium used to transport the erodent particles also play a vital role in the degradation of the material; this is mainly characterised by the corrosive properties of the solution [58-59]. Corrosion can be described as the gradual deterioration of materials by chemical and electrochemical reaction with their environment. The process is initiated by the loss of electrons, also known as the oxidation reaction [58-59]. Metals are more likely to undergo oxidation in comparison to other materials due to their tendency to donate surface electrons in an attempt to lower their energy state and be in a more

thermodynamically stable state with their environment. The released electrons then flow through the metal towards the cathodic reaction site, where they are consumed by the reduction of oxygen dissolved in the solution as depicted in *Figure 2.25* [60]; this is known as the reduction reaction. The rate of electron transfer depends on both the metal and its environment and governs the rate of corrosion [58,59,60,61,62,63].

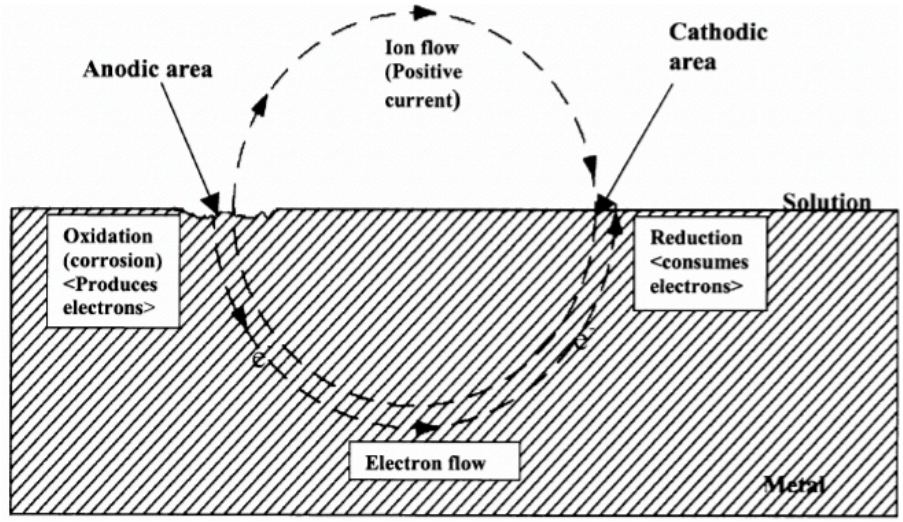

Figure 2.25: Schematic diagram for metal corroding in an electrolyte [60].

When the oxidation and reduction reactions are in equilibrium, the flow of electrons from each reaction is balanced, and there is no net current to be measured. The potential (V) at this state of equilibrium is known as the equilibrium potential (E_{corr}). Materials with more positive E_{corr} values are less likely to undergo corrosion, while those with more negative E_{corr} values are thermodynamically less stable and are therefore more prone to corrosion. The value of either the anodic or cathodic current at this thermodynamic state is called the corrosion current, I_{corr}; high corrosion current values are indicative of rapid corrosion rates [58-63].

Open circuit potential (OCP) and polarisation curves are usually used to describe the corrosion properties of a material within the surrounding medium. Open circuit potential is the equilibrium potential measured when no external potential or current is applied to the system and can be used to indicate if the material is in equilibrium with the electrolyte. Similarly to E_{corr} values, high OCP values are indicative of superior thermodynamic stability within the surrounding medium, while materials with a low OCP value are more likely to undergo corrosion [58-63].

Polarization curves, schematically shown in *Figure 2.26* [64], are graphical plots of the electrode potential versus current of both the anodic (oxidative) and cathodic (reductive) reactions when an external voltage is applied. The intersecting point of the anodic and cathodic polarization curves is an estimation of the equilibrium corrosion potential (E_{corr}) and current (i_{corr}). Tafel extrapolation and polarization resistance are methods conventionally used to measure the corrosion rates of materials rapidly and accurately. Polarization resistance (R_p) is estimated using the slope (dE/di) of the polarisation curves and represents the rate of general corrosion (i_{corr}) for metals at or near their corrosion potential, E_{corr}. The current density, i_{corr}, is related to the polarisation resistance by the Stern-Geary coefficient, B as presented in *Equations 2.3 to 2.5* [61].

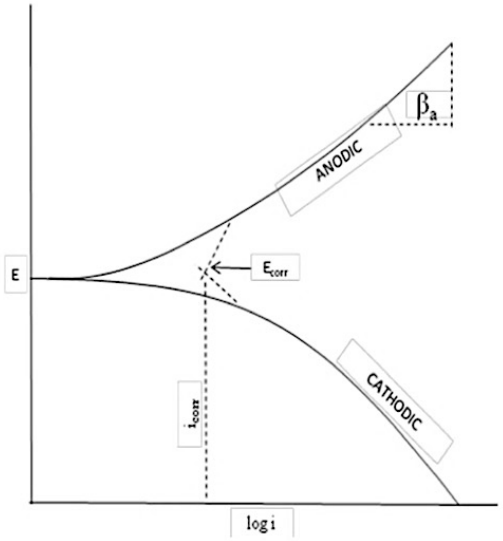

Figure 2.26: Generic polarization curve illustrating cathodic and anodic reactions [64].

$$R_p = \frac{\partial E}{\partial i}$$ Equation 2.3 [61]

$$i_{corr} = 10^6 * \frac{B}{R_p}$$ Equation 2.4 [61]

Where:

R_p in ohm-cm^2, icorr in µA/cm^2, and B in V.

$$B = \frac{b_a b_c}{2.303(b_a + b_c)}$$ Equation 2.5 [61]

Where b_a and b_c, are the anodic and cathodic Tafel slopes respectively measured in V.

The corrosion rate, CR, of the material in mm/year can then be determined using *Equation 2.6* [61] where EW is the equivalent weight of the corroding species in grams and ρ is the density of the corroding material in g.cm^{-3} [61].

$$CR = 3.27\ x\ 10^{-3}\ \frac{i_{corr}EW}{\rho}$$ Equation 2.6 [61]

2.6.1. Passivation

In certain chemical environments, the corrosion of the metal can become passive, creating a protective oxide film which inhibits further corrosion [63]. *Figure 2.27* [60] illustrates the typical behaviour of a metal that forms a passive metal oxide film during corrosion. The corrosion of these types of metals can be categorised into three stages, namely, active, passive and transpassive corrosion. During the active phase, the corrosion of the metal occurs normally. However, by the addition of an oxidising agent into the system, a protective film begins to form which is more thermodynamically stable than the metal and causes a sudden drop in corrosion current density. The passive state has lower current densities compared to the active state, and its stability predominantly depends on the cathodic process of hydrogen evolution and the reduction of oxygen and the metal ions [63]. Further increases in the oxidising agent, leads to a breakdown of the protective film and transpassive corrosion occurs in which the corrosion rate proceeds normally [62-63].

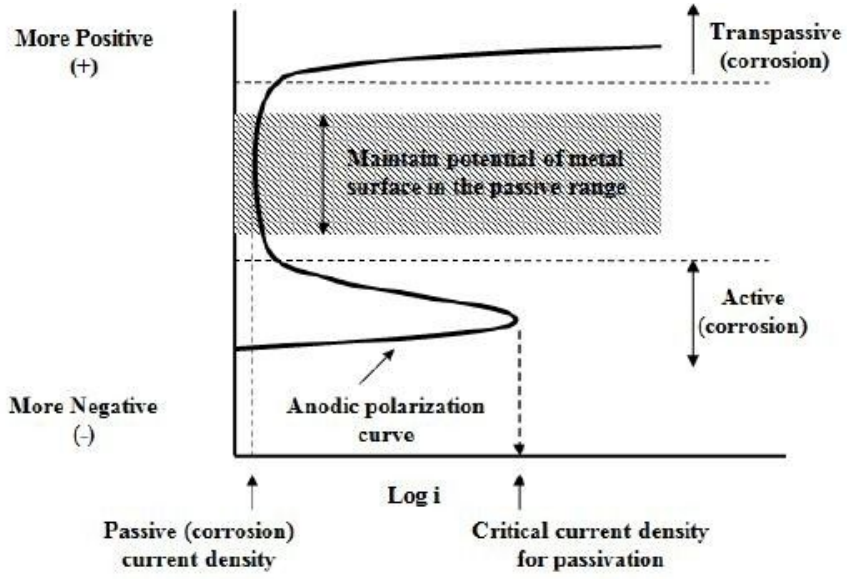

Figure 2.27: Hypothetical cathodic and anodic polarization plots for a metal undergoing passivation [60].

2.7. Corrosion of WC-based coatings

Carbides are well known for their chemically resistant nature; however, the corrosion resistance of thermal sprayed WC cermets is primarily determined by the corrosion properties of their metallic binders [3]. Cobalt (Co) which is the best-known binder metal for WC has poor corrosion properties, making WC-Co unsuitable for corrosive aqueous environments such as seawater [3]. In corrosive mediums, Co gradually becomes depleted resulting in the rapid detachment of the hard carbide grains. More corrosion resistant metals such as Ni, Cr, Ru and its alloys usually replace or are added to the Co binder system to improve the corrosion resistance of the coatings [1,3]. Tungsten carbide - Nickel (WC-Ni) remains the optimum choice for most corrosive environments as this cermet remains resistant down to a pH level of 2-3 [24]. Previous studies have indicated that the corrosion properties of cemented carbides can further be improved by the addition of refractory metal carbides such as TiC, TaC, Cr_3C_2, VC and Mo_2C [24-26,61].

Previous studies on the corrosion of HVOF hardmetal coatings have indicated a strong correlation between coating porosity and the corrosion rate [2]. Pores and microcracks become microchannels for the corrosive medium to reach the underlying substrate. It is therefore imperative that high quality coatings of low porosity, high density and superior coating-substrate bond strength are obtained [23,25-26,65]. Prior research on the corrosion properties of cold sprayed WC based coatings indicates that the process produces coatings with excellent anti-corrosion performance, similar to those of the parent material [45,56]. Dosta et al. [45] demonstrated that WC-25 wt% Co coatings deposited using a high-pressure cold gas dynamic system were more corrosion resistant in a 3.5% NaCl solution than WC-12 wt% Co coatings produced using HVOF techniques. The high-temperature process leads to the formation of oxides which results in inferior corrosion resistance when compared to parent material of the same composition. The superior chemical resistance of the cold sprayed coatings was attributed the formation of homogenous, oxide-free, low porosity coatings without cracks or delamination that prevented the electrolyte from attacking the Co matrix interface and the substrate [45].

2.8. Erosion-Corrosion

Industrial components mainly used in the oil, gas and mining industries such as centrifuges, propellers, impellers and pipes are subjected to extreme solid-particle erosion and corrosion during the transportation of slurries [1,49]. These two synergistic degradation processes have different material selection criteria. It is therefore imperative that the careful selection of the materials be conducted to prevent the damage caused by both erosion and corrosion.

Erosion-corrosion, depicted in *Figure 2.28* [66], can be described as the deterioration of a surface due to the synergistic action of erosion and corrosion, in which the rate of material degradation is greater than the sum of their individual effects [49]. The process is mainly characterised by grooves, gullies, waves, rounded holes, and directional valley patterns, and can occur by various mechanisms [49]. Erosion-corrosion can occur by the dissolution of the metal surface into metal ions and the subsequent removal by the moving fluid. The process can also occur when the protective oxide layer on the metal surface, formed during passive corrosion, is removed due to the action of a rapidly moving fluid. The exposed metal surface then corrodes and forms the protective oxide layer again, resulting in the cyclic formation and removal of the oxide layer. The repeated impact of corrosive gaseous and liquid droplets can also lead to erosion-corrosion. Damage by the synergistic effect of erosion-corrosion is usually found at high flow rates around tube blockages, tube inlet ends, or in pump impellers and can be mitigated by streamlining the piping to reduce turbulence, decreasing the fluid velocity or using more resistant materials [49,54,58-59,62-63].

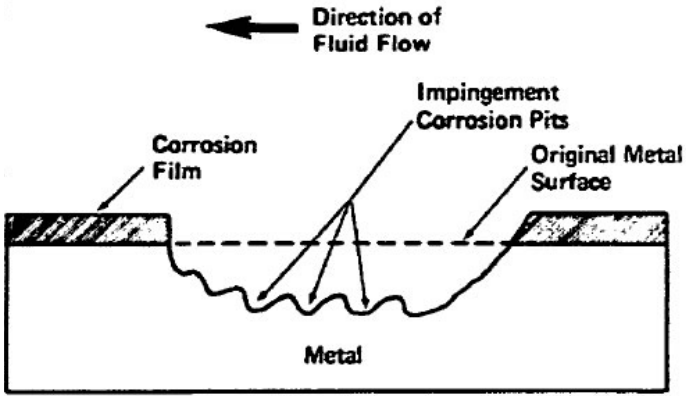

Figure 2.28: Schematic illustration of material degradation by erosion-corrosion [66].

2.9. Experimental parameter optimization

Experiments enable researchers to refute or validate a particular hypothesis and provides insight into the cause-and-effect of a given system, with the aim of gaining a better understanding it [67-68]. Very often, the system under study is composed of numerous input variables that influence its operation and resultant feedback [67-69]. Consider the hypothetical example where cold spray deposition is to be used to develop WC-Co coatings with a thickness of 500 μm, a hardness 1500 $HV_{0.3}$ and 0.5% porosity. Parameters such as the powder composition, deposition temperature, gas pressure and combustion gas composition greatly influence the properties of the resultant coating as discussed previously in *Section 2.3.3*. Each of these process parameters have ranges of values in which they can operate as summarised in *Table 2.3*. However, between the numerous combinations which may be used, there exists an optimal setting which will produce a coating with the prescribed properties. Testing each variable one at a time would be resource intensive and may complicate the understanding of the impact that each variable has on the system. Design of experiments (DoE) techniques, therefore, enable researchers to efficiently organise experiments, reduce the number of possible combinations to be tested and understand the influence of process parameters within a given system without fully exploring the full range of settings.

Table 2.3 Hypothetical process parameters for the deposition of WC-Co coatings using CGDS spraying.

Process parameter	**Range of values**
Co content in WC-Co powder	4-25 wt. %
Deposition temperature	400-500 °C
Deposition pressure	100-250 psi
Propellant gas	Air, H_2, N_2, or He.

There are several methods for designing experiments. These include but are not limited to [70]:

1. Randomized experimental design

   Parameter groups in an experiment are assigned at random, so that each individual of the population has the same chance of becoming a participant in the study [70].

2. Factorial design

A factorial experiment consists of two or more factors, each with discrete possible values or "levels", and whose experimental units take on all possible combinations of these levels across all such factors [70]. For example, a system with four factors (n) each with three levels (k) would require 3^4 (k^n) = 81 combinations to be tested. Even though this technique informs researchers of all the combination to be tested, its major disadvantage is its inefficiency and that it requires symmetry, if you have k factors, all of them must have n levels.

3. Blocking

Blocking is the non-random arrangement of experimental units into similar groups [70]. Blocking reduces known but irrelevant sources of variation between units and thus allows greater precision in the estimation of the source of variation in the study.

4. Orthogonality

An orthogonal design is an experimental design constructed to allow the independent analysis of each single factor and the interactions between all factors [67-70]. Taguchi Orthogonal Array (OA) design is a type of general fractional factorial design based on a design matrix proposed by Dr Genichi Taguchi [67-69]. Unlike factorial design, this technique allows one to consider a selected subset of combinations of multiple factors at multiple levels. The Taguchi arrays are also balanced to ensuring that all levels of all factors are considered equally and is the preferred technique for many researchers [67-69].

The use of the Taguchi DoE technique for the deposition of CGDS coatings has been recorded in literature. Goyal et al. [71-73] investigated the optimization of multiple response parameters in low-pressure cold sprayed Cu coatings using the Taguchi method and utility concept. In the study, the input variables were powder feed type, substrate material, stand-off distance, stagnation pressure and temperature and the responses to be optimised were coating density, thickness and surface roughness. The optimal parameter values were determined by calculating the signal to noise ratios (SNRs) for each response, which also served as an indication of the contribution that each parameter had on the responses measured. The variables yielding the greatest SNR values were an indication of the optimal parameters. Using this technique, the authors successfully optimised the response variables, identified the percentage contribution of each input parameter and accurately predicted the values of the optimal responses. The average

coating thickness was found to be 72.36 mm which fell within the confidence interval of 71.69 < μ < 74.13 mm predicted by the optimal coating thickness response [71-73].

To the current authors' knowledge, a systematic approach to determine the optimal spray parameters for WC-Ni systems, using low-pressure CGDS, has not been conducted and was, therefore, the main focus of the current research study. The experimental technique proposed by Goyal et al. [71-73] was implemented in the present study as it was considered to be a more accurate and efficient manner of determining the optimal spray deposition parameters for CGDS.

3. Materials and Methods

This chapter outlines the materials used and the experimental procedure that was followed to deposit the optimal WC-Ni based coatings using a low-pressure cold gas dynamic spray (CGDS) system. The section also describes the methods used to determine the slurry erosion and corrosion properties of the selected WC-Ni based coatings.

3.1. Powders preparation

Three different types of WC-based powders were used in this study; namely, an oxide reduced WC powder (FloMaster, will be referred to as WC_{ox}), and two agglomerated and sintered powders namely WC-12 wt% Co (Sulzer Metco, will be referred to as WC_{12Co}) and WC-10 wt% Ni (Polymet, will be referred to as WC_{10Ni}). All three powders are depicted *Figure 3.1(a)* to *(c)*. Nickel (Ni) powder (Centerline SST-N5001), refer to *Figure 3.1 (d)*, was blended with the carbide powders to facilitate adhesion during the coating deposition process. The Ni content was varied between 4-50 wt%, as summarised *Table 3.1*, to study its effect on the deposition and coating properties.

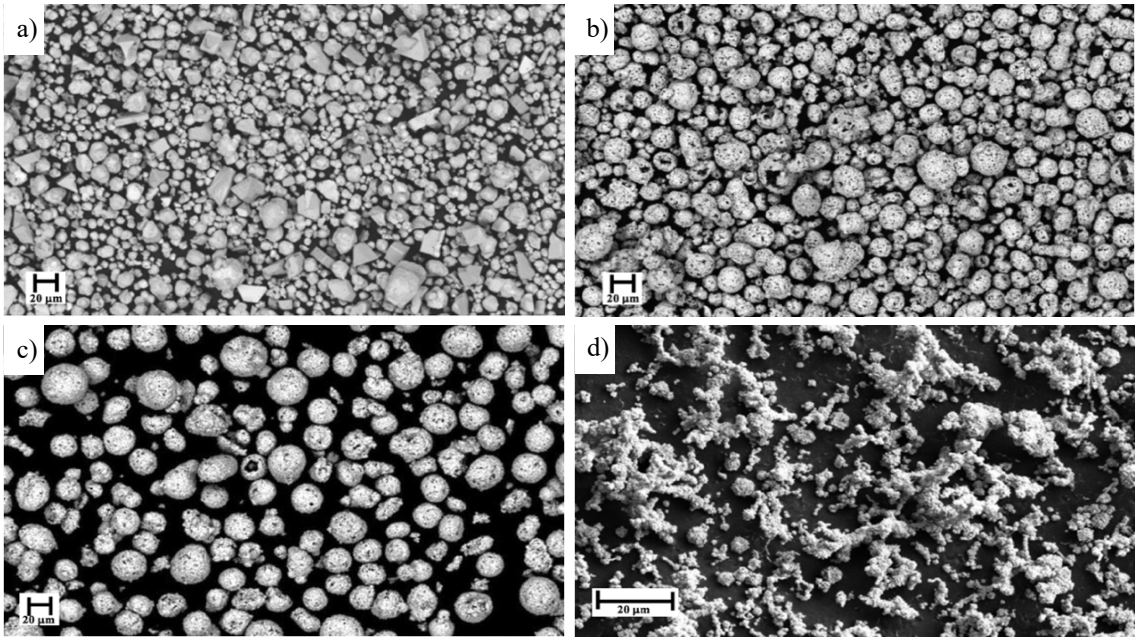

Figure 3.1: Morphology of the (a) oxide reduced WC_{ox} powder; agglomerated and sintered (b) WC_{12Co}, (c) WC_{10Ni} and (d) Ni powder.

Table 3.1: Composition of the mechanical powder blends.

Mechanical blend	wt% WC	wt% Co	wt% Ni
WC_{ox}-4Ni	96	0	4
WC_{ox} -10Ni	90	0	10
WC_{ox} -25Ni	75	0	25
WC_{ox} -50Ni	50	0	50
WC_{12Co} -4Ni	84	12	4
WC_{12Co} -10Ni	78	12	10
WC_{12Co} -25Ni	63	12	25
WC_{12Co} -50Ni	38	12	50
WC_{10Ni} (as-received)	90	0	10
WC_{10Ni} -25Ni	75	0	25
WC_{10Ni} -50Ni	50	0	50

Once the optimal deposition and coating properties were determined using the Taguchi mixed level Design of Experiments (DoE) technique (refer to *Section 3.2*), 1 wt% Molybdenum (Mo) powder (FloMaster) and 10 wt% Titanium Carbide (TiC) powder (FloMaster) were added to the optimal WC-X wt % Ni coating. This was done in order to assess if the coating properties could be further enhanced. Molybdenum is known to increase corrosion resistance while TiC is for improved coating hardness, wear and corrosion resistance. [74].

3.1.1. Mechanical mixing

A 100-watt rotary ball mill with a speed of 66 revolutions per minute (rpm) was used to blend the powders for 2 hours. Steel balls with a shot ratio of 2:1 were used along with a 99% pure ethanol solvent. The aim of the procedure was to achieve a near uniform dispersion of the powders with minimal powder comminution. The powder slurry was then dried into a powder at 60 °C using a Heidolph Laborator 4010 Digital rotary evaporator. Each powder was stored in airtight containers in preparation for the subsequent characterisation tests and the cold spray deposition process.

3.1.2. Powder characterization

The as-received and milled powders were characterised according to the following properties:

3.1.2.1. Particle size distribution

A Microtac S3500 particle size analyser was used to determine the particle size distribution of the as-received and milled powders. One gram of each powders was first dispersed in a solution of distilled water and sodium hexametaphosphate to prevent particle agglomeration prior to size analysis. One millilitre of the powder solution was then poured into the analyser, followed by a 2 minute sonication process to disperse any remaining powder agglomerates. The Microtac S3500 made use of a three-laser system and lenses with a refractive index of 1.33 to determine the size distribution of the powders.

3.1.2.2. Powder morphology and composition

A Carl Zeiss Sigma field emission scanning electron microscope (FESEM) coupled with an energy dispersive X-ray spectroscope (EDS), was used to study the morphology and analyse the elemental composition of the as-received and milled powders.

3.1.2.3. Phase analyses

X-ray diffraction (Bruker D2, Phaser with a Lynx Eye detector) analysis of the powders was conducted for phase identification. A cobalt anode, with X-ray generator settings of 30 kV and 10 mA, was used for the analysis. The measurements were made from 10° to 90° at a rate of 0.026° per second.

3.2. Deposition parameter optimization

Once the powders had been mechanically blended as listed in *Table 3.1*, a Taguchi mixed level design of experiments (DoE) technique was constructed to determine the optimal spray parameters for each powder combination. Four input parameters, also referred to as the controlling factors, were considered for the optimisation study, namely wt% Ni, the cold spray

deposition temperature, stagnation pressure and gun-substrate stand-off distance (SOD). An L16 orthogonal array matrix comprised of 2 factors with 2 and 4 levels respectively was selected to organise the experiments as summarised in *Table 3.2*. Only 16 spray parameter combinations, forming 132 coatings, had to be tested to determine the optimal setting for each factor. Without the use of a DoE technique to find the optimal parameter settings for each of the 3 WC-Ni powder types, a total of 64 spray combinations would have had to be tested, requiring the fabrication of 528 coatings.

Table 3.2: Cold spray parameters determined using the Taguchi method for each blend.

Process parameter	Level 1	Level 2	Level 3	Level 4
Nickel content (wt. %)	4	10	25	50
Stagnation pressure (kPa)	690 (100 psi)	793 (115 psi)	896 (130 psi)	1000 (145 psi)
Temperature (°C)	450	550	-	-
Standoff distance (mm)	10	15	-	-

The Ni content levels were varied in accordance with work previously conducted by Melendez et al. [43] in order to compare their resultant coating properties with those obtained in this study. The levels of the deposition temperature, pressure and SOD were varied within the ranges recommended by Centerline Windsor Limited for the deposition of Ni powder and the cold spray system's maximum operational capacity as summarised in *Table 3.3* [75].

Table 3.3: Recommended spray parameters for the deposition of Ni powder (Centerline SST-N5001) [75].

Temperature	450-550 °C
Pressure	690-1720 psi
Carrier gas	Air or Nitrogen
Standoff distance	10-25 mm
Feedrate	12-18 g/min
Gun transverse speed	10-250 mm/s depending on the process settings and target thickness
Surface preparation	SST G0002 commercial blast at 620 kPa

The 4-level factors were assigned to the Ni content and stagnation pressure parameters due to the significant gap between the ranges of their values, while the 2-level factors were assigned to the deposition temperature and SOD parameters whose values differed to a lesser extent. Minitab® 16.2.4, a robust statistical computing software package, was then applied to generate the L16 orthogonal array matrix presented in *Table 3.4*. This matrix provided the combination of input parameters to be tested for the optimisation process.

Table 3.4: L16 orthogonal array matrix with pre-determined combination of input parameters to be tested for the optimisation process.

OA Experiment No.	Nickel content	Pressure	Temperature	SOD
1	4	100	450	10
2	4	115	450	10
3	10	130	550	10
4	10	145	450	10
5	25	100	550	10
6	25	115	550	10
7	50	130	450	10
8	50	145	450	10
9	4	130	550	15
10	4	145	550	15
11	10	100	450	15
12	10	115	450	15
13	25	130	450	15
14	25	145	450	15
15	50	100	550	15
16	50	115	550	15

Coating thickness and hardness were used as the output responses to be measured as these properties were considered to be a critical selection criterion for the erosion and corrosion properties of the coatings. Each set of parameters was repeated three times, and their responses averaged.

Similarly to the work conducted by Goyal et al. [71-7], a signal to noise ratio (SNR) for each response was then calculated using *Equation 3.1* [71].

$$S/R = \mathbf{-10\ log}\ \left[\frac{1}{R}\sum_{j=1}^{R}\frac{1}{Y_j^{\,2}}\right] \qquad \text{Equation 3.1 [71].}$$

Where Y_j j = 1,2… n are the response values under the trial conditions repeated R times, being hardness and coating thickness for the current study.

The SNR served as an indication of the contribution that each parameter had on the responses measured, as previously discussed in *Section 2.9*. Since coating thickness and hardness are both 'the higher, the better' type responses, the spray parameters giving the highest signal to noise ratio (SNR) were selected as optimal. It is also important to note that one set of experiments can optimise one output response while diminishing the other. A trade-off is often required between responses, hence the average SNR of both the coating hardness and thickness was used to determine the optimal parameter setting for each factor. The SNR values and the utility concept were also applied to predict the coating thickness and hardness values of the optimal WC-Ni based coatings [71-73].

3.3. Coating deposition

3.3.1. Substrate preparation

The WC-Ni based powders were deposited onto mild steel substrates cut into samples 20 mm × 20 mm × 3 mm in dimension. Prior to the deposition process, the substrates were activated by grit blasting using alumina particles (Centerline SST-G0002) with mesh sizes with −300 + 100 μm [17]. The parameters used for grit blasting are summarised in *Table 3.3*.

3.3.2. Cold spray deposition process

A Centreline SST Series P low-pressure cold spray machine, shown in *Figure 3.2*, was used to deposit the WC-Ni based powders onto the mild steel substrates. Air was used as the carrier gas in which a CompAir external air compressor with a maximum capacity of 1034 kPa (150 psi) was used to generate the air flow required to achieve the air pressures used in this study. An integrated, dual-hopper, non-pressurized vibratory powder feeder with a machine feed rate setting of 5% was used to introduce the powder particles into the moving gas stream. A convergent-divergent De Laval nozzle with a length of 120 mm and an entrance and exit diameter of 2.5 mm and 6 mm respectively was used to transmit the powders to the substrate. The deposition temperature, stagnation pressure and standoff distance used in the study were presented in *Table 3.2*. The movement of the spray gun was controlled by a programmable robotic system. Eight passes of powder were sprayed onto the substrates using an automated gun moving at a transverse velocity of 3 $m \cdot s^{-1}$.



Figure 3.2: Centreline SST Series P low pressure cold spray machine.

3.4. Coating characterization

3.4.1. Sample preparation

The coatings were cut along the cross-section in order to obtain a representative analysis of the resultant coating and substrate properties. Cutting was achieved using a Struers Secotom-10 precision cutting machine fitted with a 12 cm diameter Struers diamond coated cutting disk. A cutting speed and feed rate of 45 $m.s^{-1}$ and 0.02 $mm.s^{-1}$ respectively, with water as a cooling lubricant, was used during the cutting process. The cross sections were hot mounted in Struers Polyfast conductive resin for SEM analysis and Bakelite for non-SEM samples using a Struers CitoPress-10 mounting press under a pressure and temperature of 5000 kPa and 200 ºC respectively. Samples subjected to XRD analysis were sectioned and left unmounted. All samples were ground and then polished according to the procedure listed in *Table 3.5*.

Table 3.5: Grinding and polishing procedure for the cold sprayed coatings.

	Grinding			**Polishing**	
Step	Planar grinding	Fine Grinding 1	Fine Grinding 2	Polishing 1	Polishing 2
Surface	MD-Piano 220	MD-Piano 1200	MD-Largo	MD-Dac	MD-Nap
Abrasive	None	None	9 µm DP-Suspension	10 µm DP-Suspension	11 µm DP-Suspension
Lubricant	Water	Water	DP-Blue	DP-Blue	DP-Blue
Speed (rpm)	300	150	150	150	150
Force (N)	80	80	80	80	80
Time (min)	Until planar	5	10	15	15

3.4.2. Coating properties

The cold sprayed coatings were characterized according to the following properties:

3.4.2.1. Coating thickness

Low magnification (×50, ×100, ×200, ×500 and ×1000) optical microscopy (LEICA DM6000 M, attached with a LEICA DFC490 camera) was used to observe the coating build-up. Optical images and coating thickness measurements were acquired using Leica Application Suite image processing software. A total of 3 thickness measurements were taken per coating and the average thickness calculated.

3.4.2.2. Coating hardness

Vickers micro-hardness tests, using a 300 gf load with a dwell time of 10 s, were conducted on the transverse sections of the coatings. A total of 12 indents were made per coating in accordance with the ASTM C1327 [76] which requires that each indent be spaced at a distance of at least four times the diagonal of the previous indent as depicted in *Figure 3.3* [76]. This procedure ensures that the effects of strain hardening and cracking which may be introduced in the coatings during indentation do not influence the subsequent hardness readings.

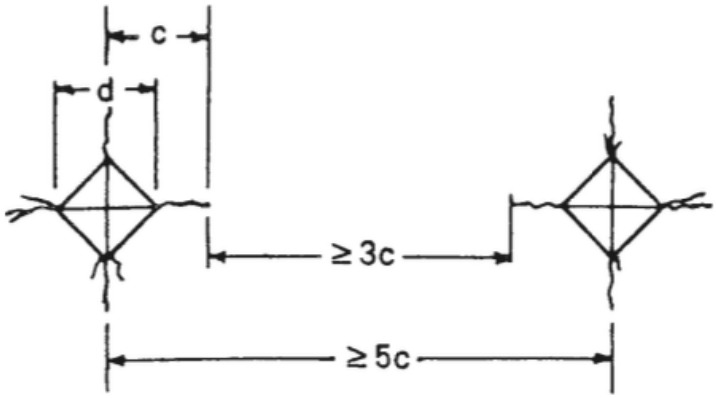

Figure 3.3: Closest permitted spacing for Vickers indentations where c represents the crack length induced from the indentation [76].

3.4.2.3. Elemental composition analyses

Field emission scanning electron microscope (FESEM) and energy dispersive X-ray spectroscope (EDS) analysis were used to characterise the microstructure and composition of the coatings and substrate. The wt % values of the W atoms, together with the known C:W weight ratio of 0.0613 was used to calculate the percentage of WC retained in the coatings. Elemental composition maps were compiled to assess the homogeneity of each element and to investigate the occurrence of coating-substrate diffusion.

3.4.2.4. Phase analysis

X-ray diffraction analysis of the coatings was conducted for phase identification using the same operating parameters described in *Section 3.1.2.3*. These results were then compared to those obtained from the corresponding feedstock powders to detect if any phase changes, usually prevalent in the high temperature deposition of WC-based coatings [4,5], had occurred during the cold spray deposition process.

3.4.2.5. Porosity

The percentage porosity of each coating was determined using low magnification (×1000) SEM micrographs of the coating cross-section obtained and ASTM E2109-01[77]. This test method is used to determine the area percentage porosity and stipulates that the micrographs should be representative of the coatings whilst ensuring that the resolution of the pores is well defined.

ImageJ analysis software was used to calculate the percentage of black areas within the images which was synonymous with the pores within the coatings.

3.4.2.6. Binder mean free path and WC grain size

The binder mean free path and WC grain size were calculated according to *Equation 3.2 [*78]. This linear intercept method was implemented using SEM micrographs at a magnification of ×1000.

$$\lambda = (1-f)/NL \qquad \text{Equation 3.2 [78].}$$

Where *f* is the volume fraction of the dispersed phase determined from the image and *NL* is the number of non-contiguous carbide grains intersected on a metallographic plane by a line of unit length.

3.5. Slurry erosion and corrosion testing

3.5.1. Slurry erosion test

A slurry jet impingement rig based on the design developed by Zu et al. [79] was used to conduct the erosion tests. Images of the erosion rig and its primary mechanism of operation are shown in *Figure 3.4* [79]. The operational parameters used in the experiments are summarised in *Table 3.6*. An impact angle of 90° was used in order to compare the findings with those obtained for the WC-Co based coatings deposited using HVOF spraying by Ogunmuyiwa [96].

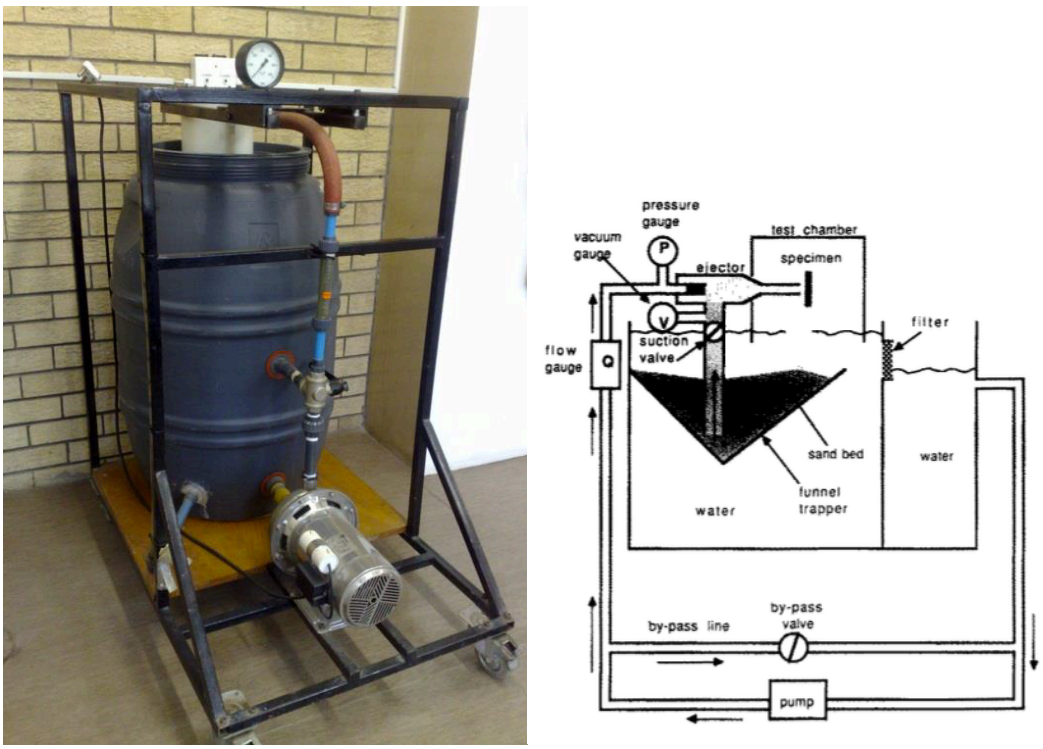

Figure 3.4: a) Slurry jet impingement rig used to conduct erosion tests; b) schematic diagram of the rig's operating mechanism [79].

Table 3.6: Parameter settings used for the slurry erosion tests.

Operating parameter	**Value**
Erodent	Silica sand
Carrier fluid	Tap water
Operating temperature	25 ± 3 ^{o}C
Erodent concentration of slurry	16 wt%
Impact velocity	6.4 ms^{-1}
Impact angles	90°
Test time	120 minutes

Prior to testing the coatings were ground and polished to a 1 μm surface finish. Each erosion test was conducted for 120 minutes, in which the mass loss of the sample was recorded every 5 minutes for the first 10 minutes, followed by measurement at 10-minute intervals. The samples were cleaned with water and then weighed before each erosion test and between each measurement interval. Mass loss versus time graphs were plotted from the obtained data. Fresh silica was used for each test; with time the edges of the silica particles erode thereby changing

their morphology which in turn influences the wear rates and mechanisms of the coatings. Each test was repeated 3 times per coating in order to obtain the average of the wear rate.

3.5.2. Corrosion tests

Corrosion tests were conducted to determine the corrosion rate, corrosion mechanism and the effect of Mo and TiC additions on the chemical behaviour of the coatings. Tap water was used as the corrosive medium in order to determine its contribution to the damage of the coatings observed during the slurry erosion testing.

Potentiostatic, potentiodynamic and 12-hour open circuit potential measurements were used to analyse the corrosion characteristics of the coatings. A Metrohm Autolab PGSTAT302 potentiostat comprising of a 500 ml cylindrical Pyrex glass corrosion cell and the conventional three-electrode system, namely a 3 M silver (Ag)/ Silver chloride (KCl) reference electrode, a graphite counter electrode and a working (i.e. the WC-Ni based coating) electrode was used to conduct the corrosion tests. An insulated copper wire was first attached to the surface of the coating using aluminium tape before being cold mounted face-down in EpoFix resin and polished to a 1 μm finish. The corrosion cell was then filled with 500 ml of tap water as illustrated in *Figure 3.5*. The water was replaced after each polarisation scan to maintain a consistent electrolyte composition throughout the tests.

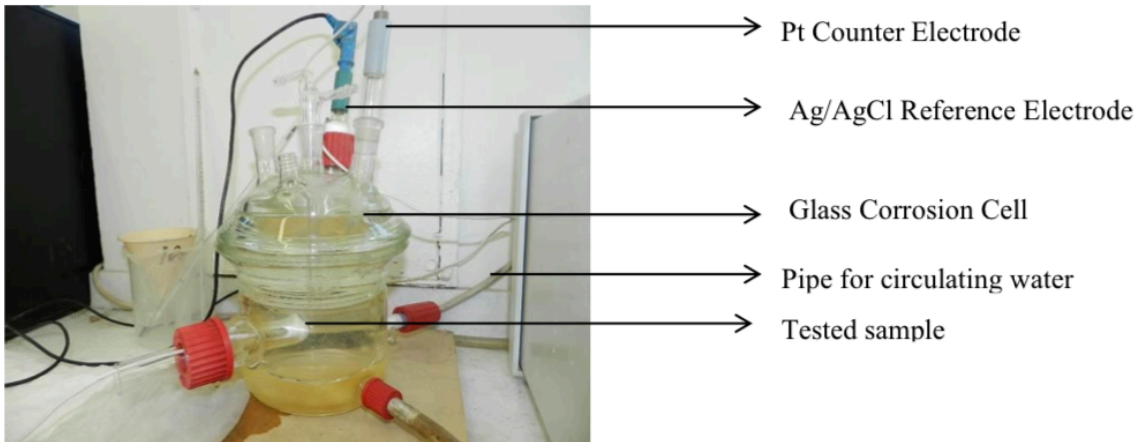

Figure 3.5: Autolab corrosion cell used for electrochemical testing.

Polarization curves were obtained by applying an external voltage from −800 mV to 1200 mV at a constant scan rate of 1 mV/s. Autolab Nova version 1.10.1.9 software was used to determine the open circuit potential (OCP), corrosion potential (E_{corr}), corrosion current (I_{corr}) and corrosion current density (i_{corr}). The linear polarisation resistance method, in which the slope of the potential versus current curve is manually calculated, was applied to calculate corrosion rate of the coatings in accordance with *Equation 3.3* [61]. ASTM G3-89 (2010) [80], ASTM G5-94 (2011) [81], ASTM 102-89-e1 (2015) [82], ASTM G59-97 (2014) [61], and NACE/ASTM G193-12d (2012) [83] standards were applied for the electrochemical measurements.

$$CR = \mathbf{3.27x10^{-3}}\ \frac{i_{corr} EW}{\rho} \qquad \text{Equation 3.3 [61]}$$

Where CR is corrosion rate in mm/year, *EW* is the sample equivalent weight, ρ is the sample density and i_{corr} is the corrosion current density.

3.5.3. Wear scar and corrosion damage analysis

The analyses of the wear scars and corroded surfaces were critical in understanding the wear and corrosion mechanisms which had taken place during testing. These damaged surfaces were studied using FESEM and EDS.

4. Results

4.1. Powder characterization

4.1.1. As-received powders

4.1.1.1. Oxide reduced WC_{ox} powder

The oxide reduced WC_{ox} powder was composed of two different morphologies, namely angular (to a minor extent), and spherical and agglomerated particles as observed in *Figure 4.1*. Overall, the powder had a particle size distribution of –45 and +3 µm with a D_{50} size of 22.03 µm, as indicated in *Figure 4.2*, which was within the ideal size range of 1-50 µm for the cold spraying process [17]. The EDS and XRD analyses, depicted in *Figure 4.3*, confirmed the presence of elemental W and C in the form of WC and that trace amounts of W_2C crystals were also present in the as-received powder.

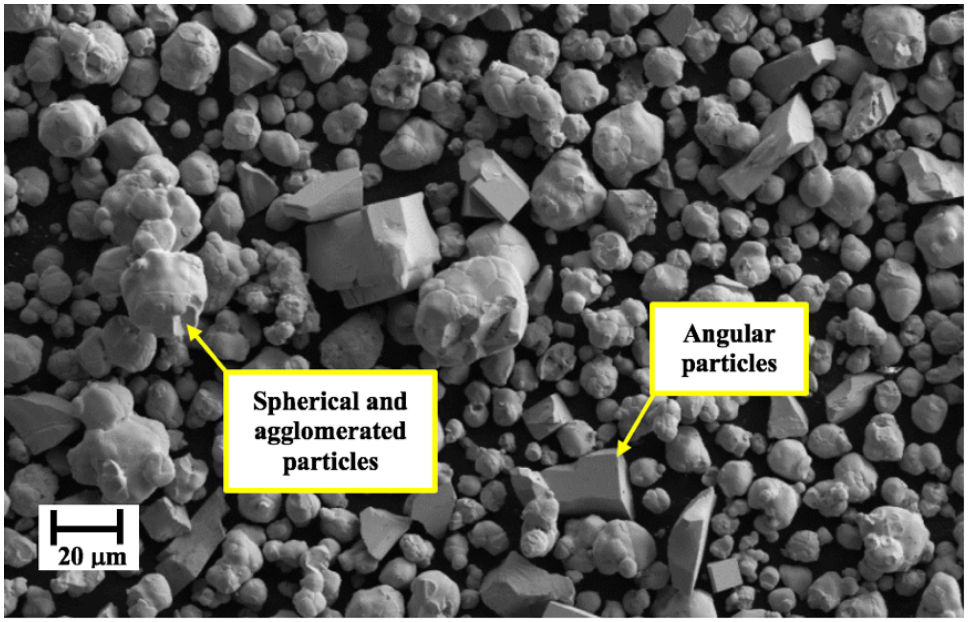

Figure 4.1: FESEM micrographs of as-received oxide reduced WC_{ox} powder.

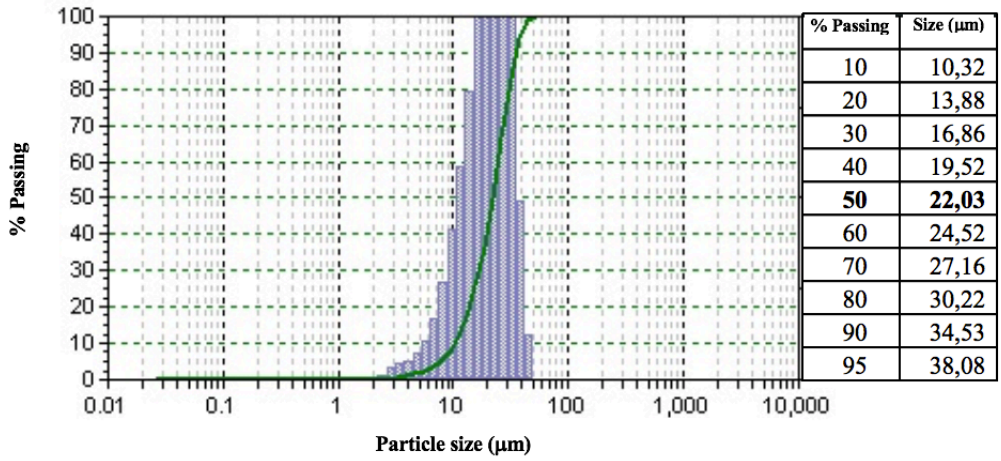

% Passing	Size (µm)
10	10,32
20	13,88
30	16,86
40	19,52
50	**22,03**
60	24,52
70	27,16
80	30,22
90	34,53
95	38,08

Figure 4.1: Particle size distribution of the as-received oxide reduced WC_{ox} powder.

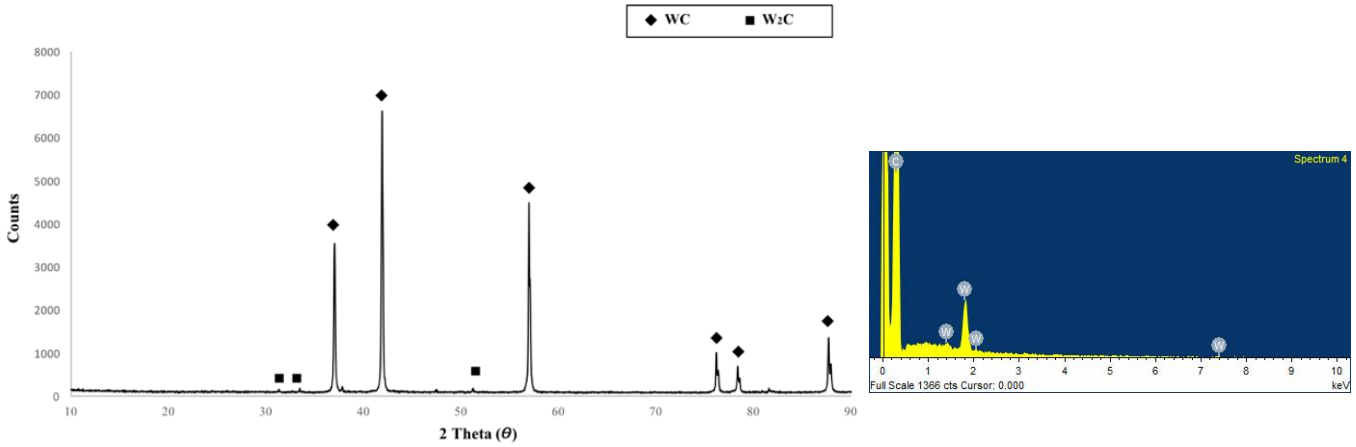

Figure 4.3: XRD pattern of the as-received oxide reduced WC_{ox} powder.

4.1.1.2. Agglomerated and sintered WC_{12Co} powder

The agglomerated and sintered WC_{12Co} powder was mainly composed of highly porous spherical particles with a few oblong-shaped particles as seen *Figure 4.4*. Each micron-sized particle was composed of many nano-sized WC crystals embedded within a Co metal binder. The EDS and XRD analyses presented in *Figure 4.5* confirmed that only WC and Co were present with no deleterious phases detected. The powder particle distribution was – 66 +13 µm with a D_{50} of 34.80 µm as indicated in *Figure 4.6*.

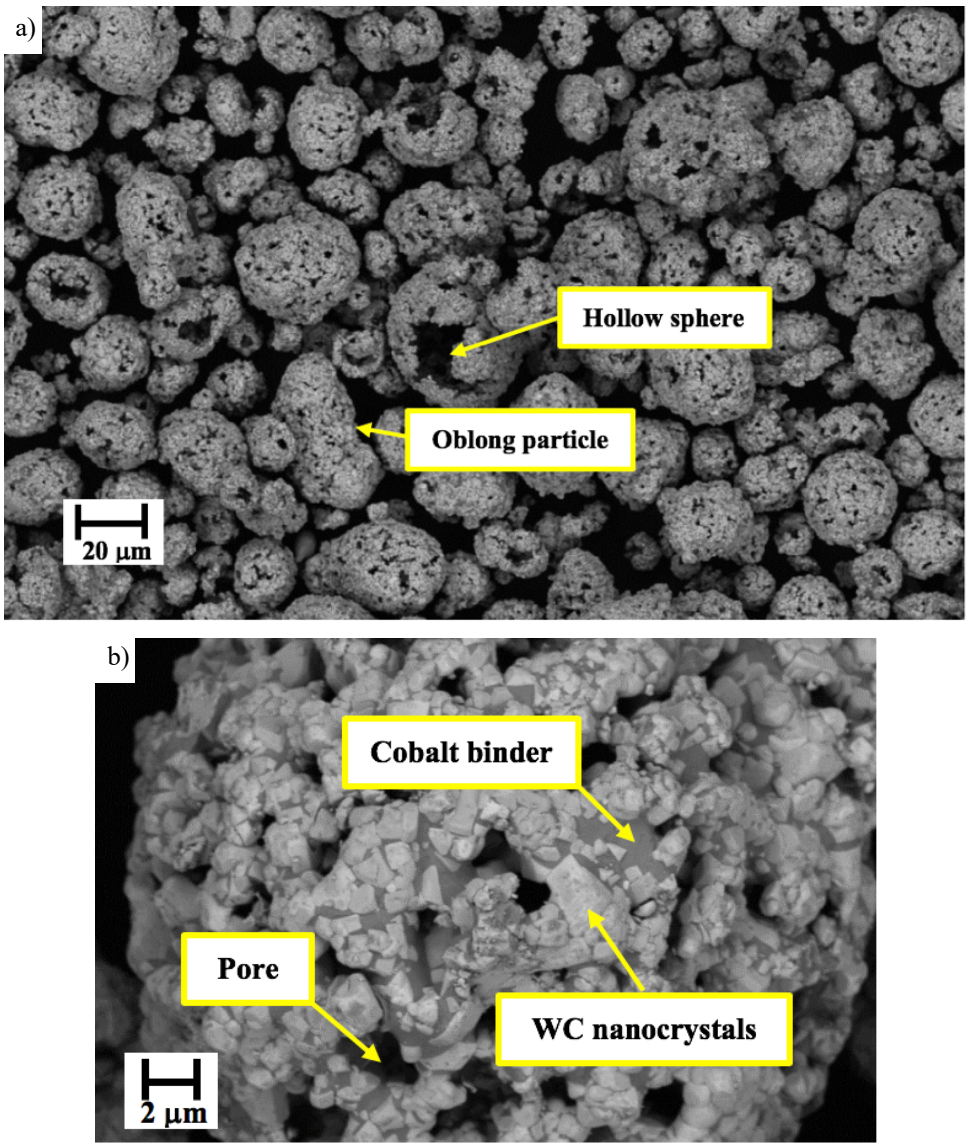

Figure 4.4: FESEM micrographs of a) the as-received spherical and agglomerated WC_{12Co} powder in low magnification and b) the WC_{12Co} particle in high magnification.

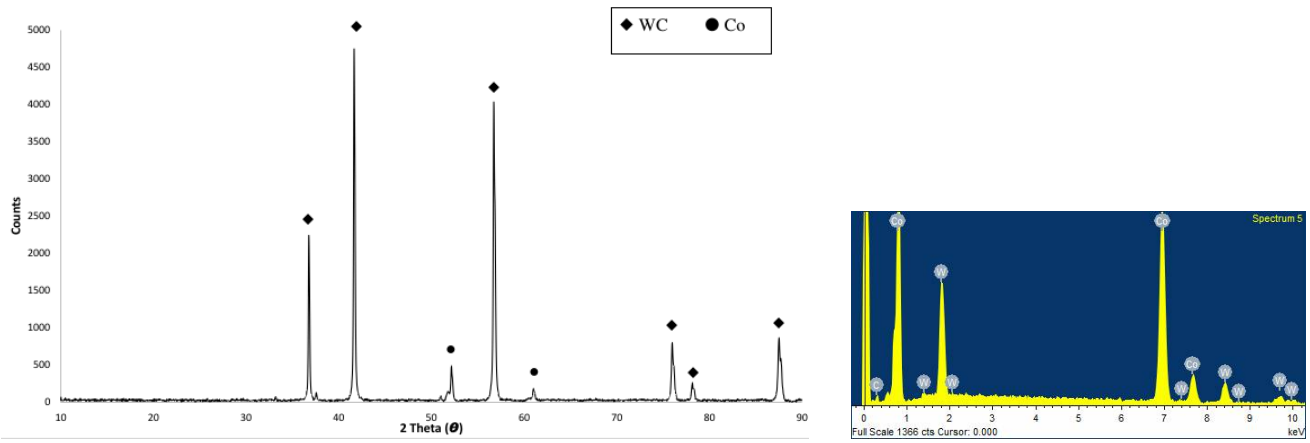

Figure 4.5: XRD pattern of the as-received spherical and agglomerated WC_{12Co} powder.

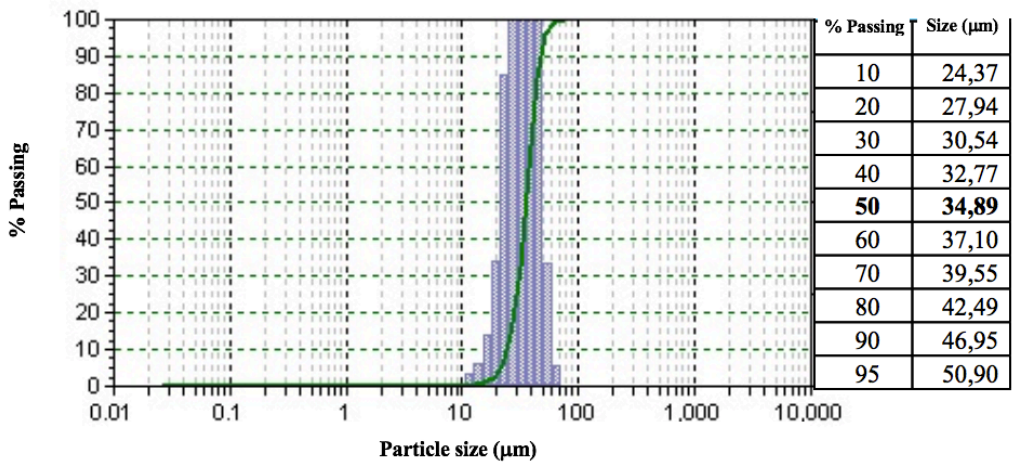

% Passing	Size (µm)
10	24,37
20	27,94
30	30,54
40	32,77
50	**34,89**
60	37,10
70	39,55
80	42,49
90	46,95
95	50,90

Figure 4.6: Particle size distribution of the as-received spherical and agglomerated WC_{12Co} powder.

4.1.1.3. Agglomerated and sintered WC_{10Ni} powder.

The SEM micrographs of the WC_{10Ni} powder are presented in *Figure 4.7.* The morphology of the agglomerated and sintered WC_{10Ni} powder was similar to the WC_{12Co} powder. The WC_{10Ni} powder particles were also spherical and oblong shaped and comprised of nanosized WC crystals fused together by a Ni matrix. The XRD analyses presented in *Figure 4.8* indicated only the presence of WC and Ni, while trace amounts of oxygen were detected in the EDS analyses of the powder. The powder particle distribution was – 66 +13 µm with a D_{50} of 34.56 µm as indicated in *Figure 4.9*. This particle size was also within the size range recommended for the cold spraying process [17].

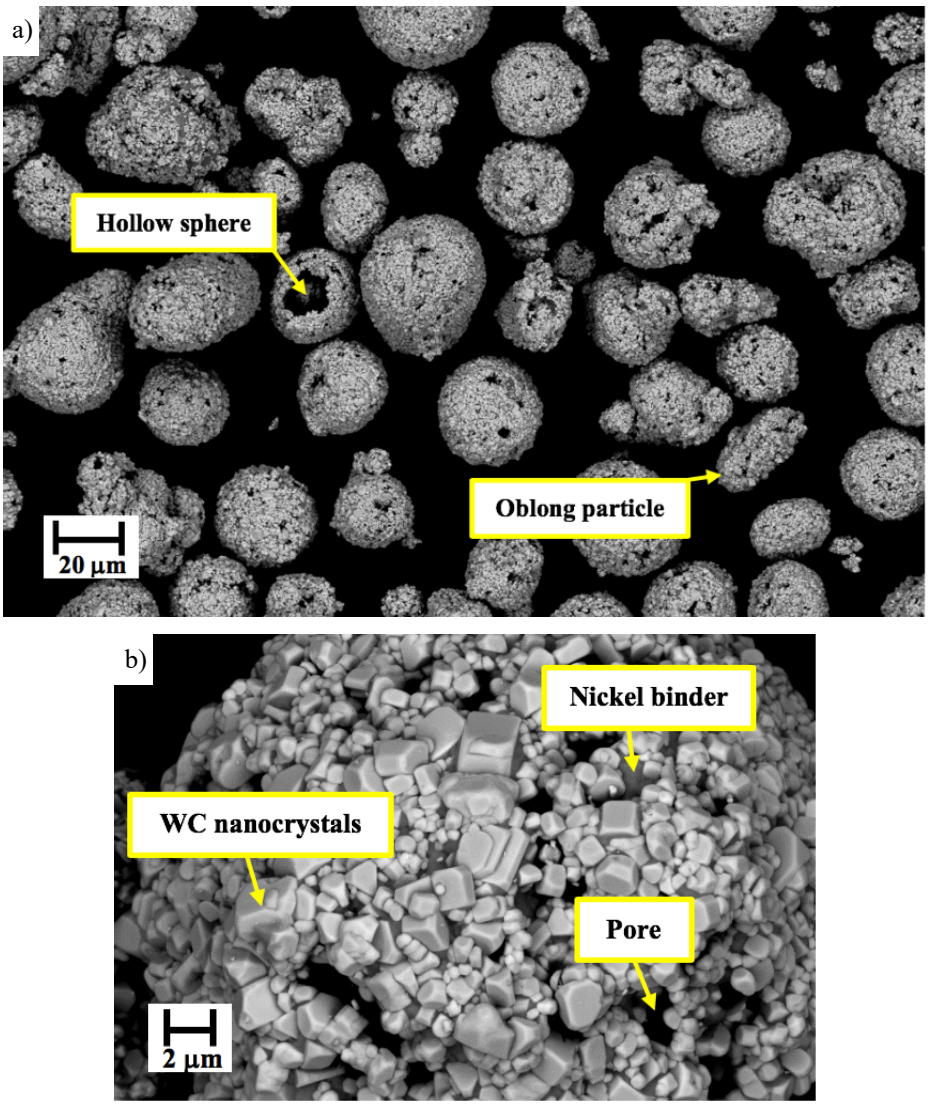

Figure 4.7: FESEM micrographs of a) the as-received spherical and agglomerated WC_{10Ni} powder in low magnification and b) the WC_{10Ni} particle in high magnification.

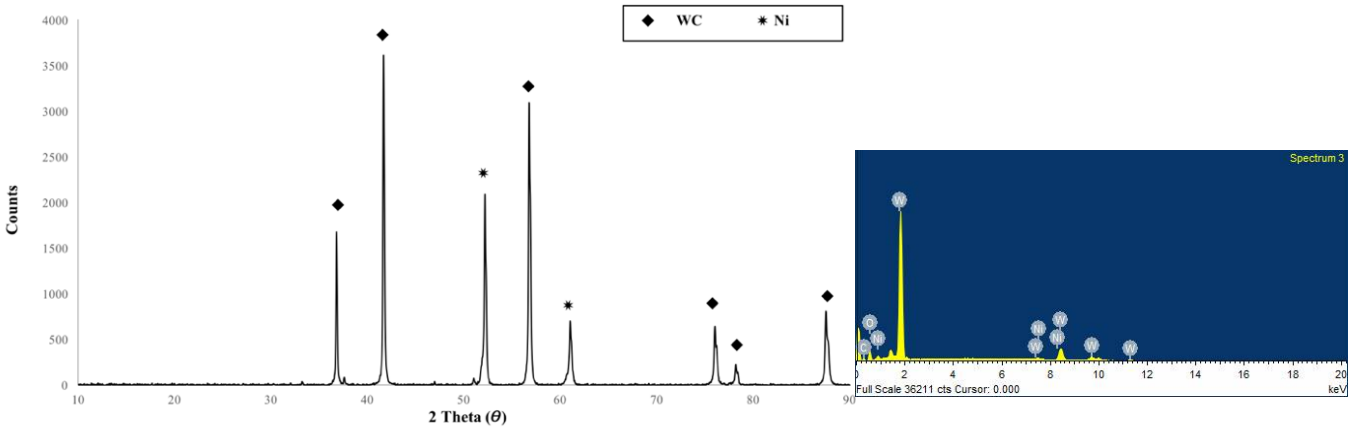

Figure 4.8: XRD pattern of the as-received spherical and agglomerated WC_{10Ni}.

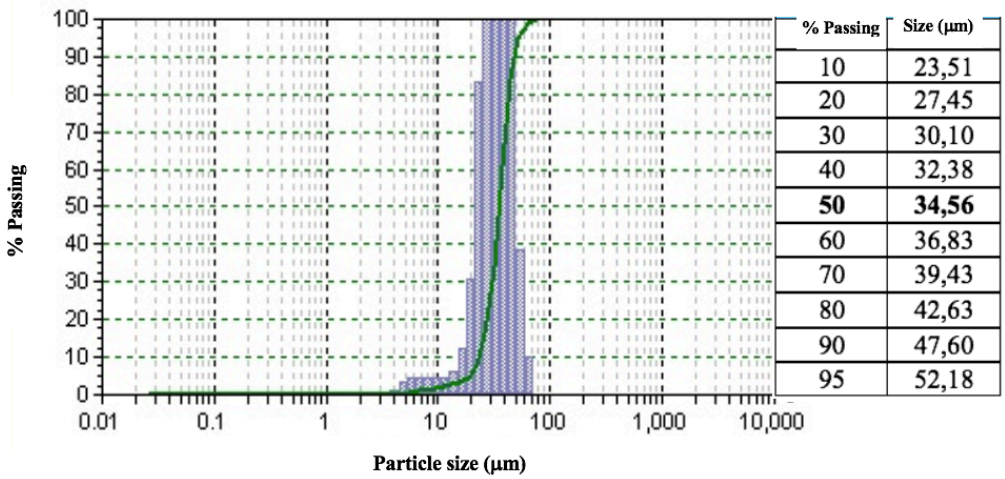

% Passing	Size (µm)
10	23,51
20	27,45
30	30,10
40	32,38
50	**34,56**
60	36,83
70	39,43
80	42,63
90	47,60
95	52,18

Figure 4.9: Particle size distribution of the as-received spherical and agglomerated WC_{10Ni}.

4.1.1.4. Nickel powder

The morphology of the Ni powder, presented in *Figure 4.10,* differed from what was observed with the WC-based powders. The powder particles were mainly composed of dendritic crystals, giving rise to a high surface area. A few near-spherical particles of varying sizes were also observed. The XRD pattern indicate the presence of Ni and that trace amounts of oxygen were detected in the EDS analysis of the powder as indicated in *Figure 4.11*. Overall, the powder particles had a wide particle size distribution of – 37+ 0.9 µm and a D_{50} of 8.68 µm (*Figure 4.12*).

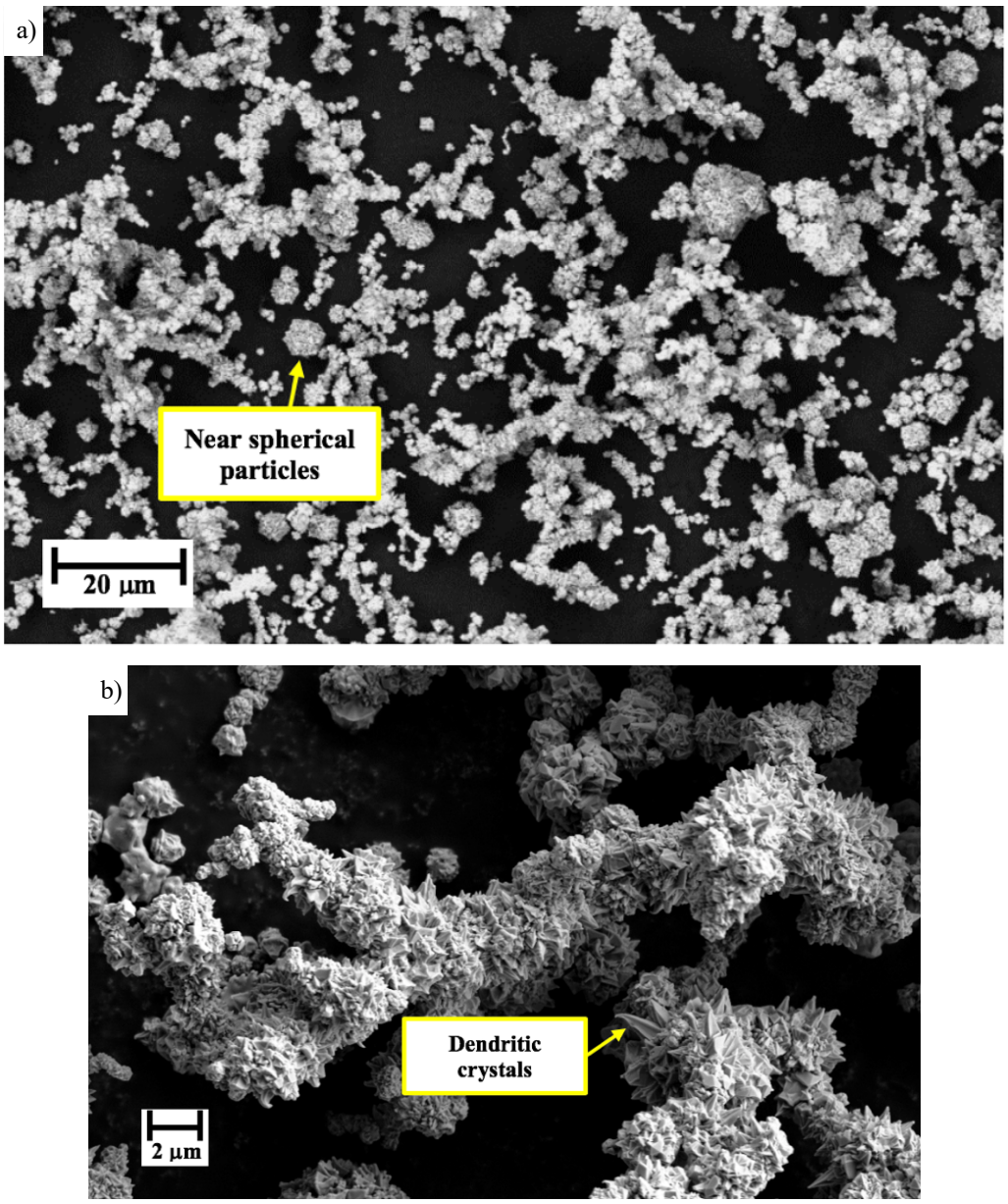

Figure 4.10: FESEM micrographs of the as-received Ni powder in a) low magnification and a) high magnification.

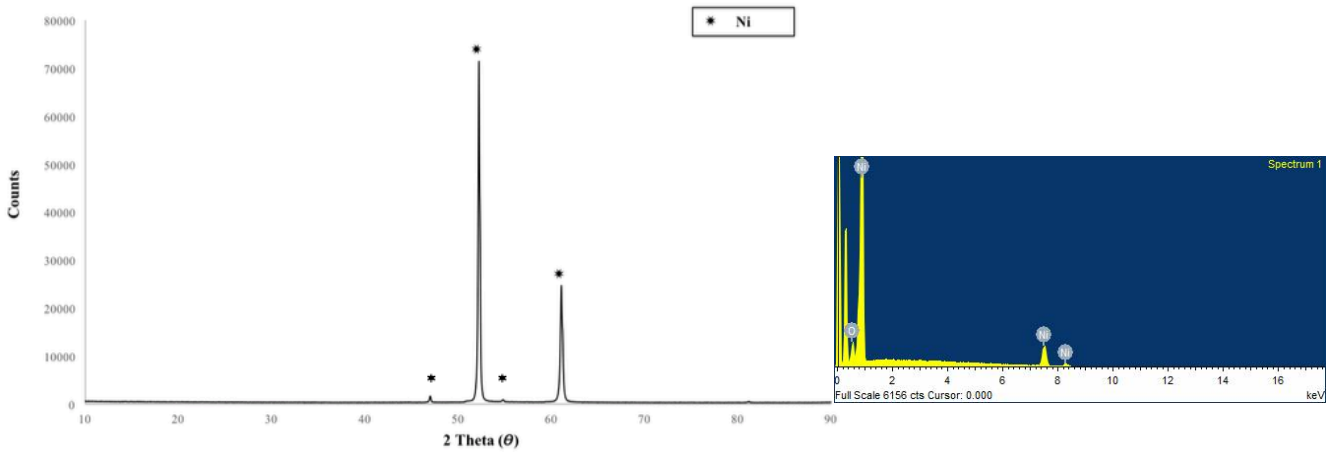

Figure 4.11: XRD pattern of the as-received Ni powder.

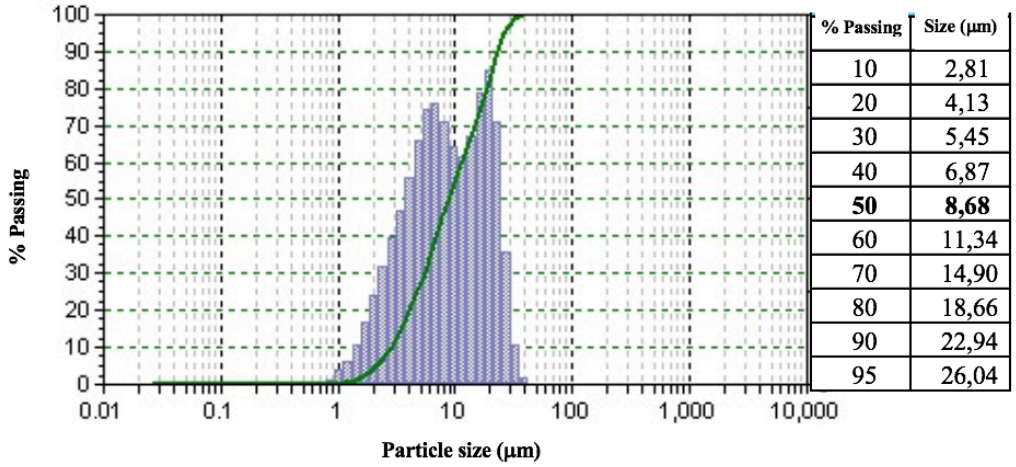

% Passing	Size (µm)
10	2,81
20	4,13
30	5,45
40	6,87
50	**8,68**
60	11,34
70	14,90
80	18,66
90	22,94
95	26,04

Figure 4.12: Particle size distribution of the as-received Ni powder.

4.1.2. Mechanically mixed powders

Eleven powders were prepared for deposition by cold gas dynamic spraying as listed in *Table 3.1* in *Section 3.1*. The light mechanical milling technique resulted in well-mixed powders with a relatively homogenous distribution of carbide and Ni particles as seen in *Figure 4.13*.

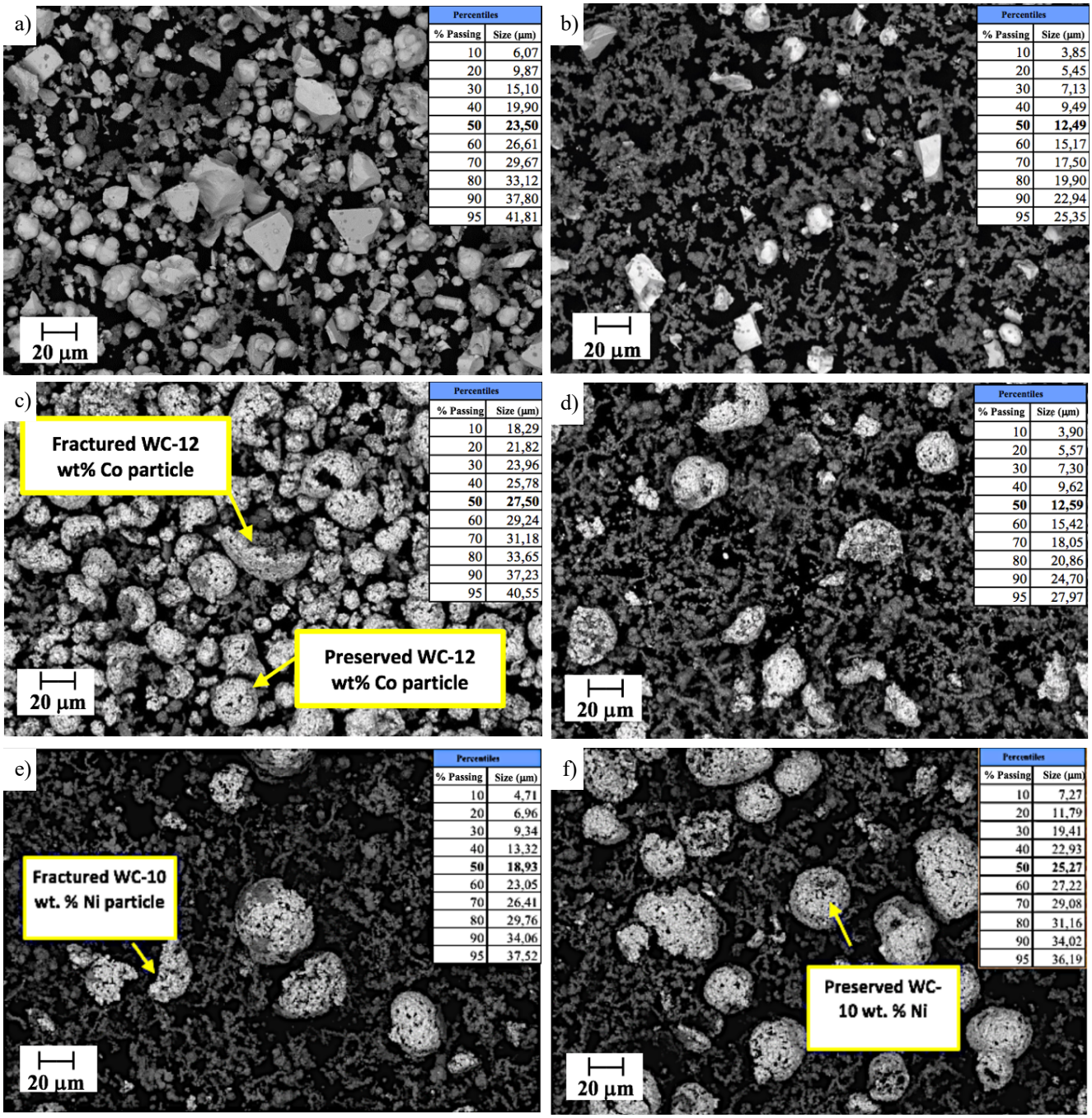

Figure 4.13: SEM micrographs of the milled, oxide reduced a) WC_{ox}-4Ni, b) WC_{ox}-50Ni, c) WC_{12Co}-4Ni, d) WC_{12Co}-50Ni, e) WC_{10Ni} -25Ni and f) WC_{10Ni} -50Ni powders.

A few fractured WC particles can be observed indicating that powder comminution occurred which was likely caused by the impact of the carbide particles and steel balls. The reduction in the average particle size of the milled powders with increasing Ni content was also noted across all powder types. This was because the Ni particles were significantly smaller and present in larger volumes compared to the carbide particles. The average particle size across all powder

blends ranged from 27.50 to 12.49 μm, as summarized in *Table 4.1,* and were still within the recommended particle size suitable for CGDS [17].

Table 4.1: D_{50} of the WC-Ni based powder particles used in the current study.

Mechanical blend	**D_{50} (μm)**
WC_{ox}-4Ni	23.50
WC_{ox} -10Ni	16.30
WC_{ox} -25Ni	16.81
WC_{ox} -50Ni	12.49
WC_{12Co} -4Ni	27.50
WC_{12Co} -10Ni	25.12
WC_{12Co} -25Ni	21.47
WC_{12Co} -50Ni	12.59
WC_{10Ni} (as-received)	34.56
WC_{10Ni} -25Ni	25.27
WC_{10Ni} -50Ni	18.93

Smearing of the Ni powder onto some of the WC particles was also observed, while a few Ni particles become embedded within the pores of the spherical and agglomerated type carbide particles, as indicated in *Figure 4.14.*

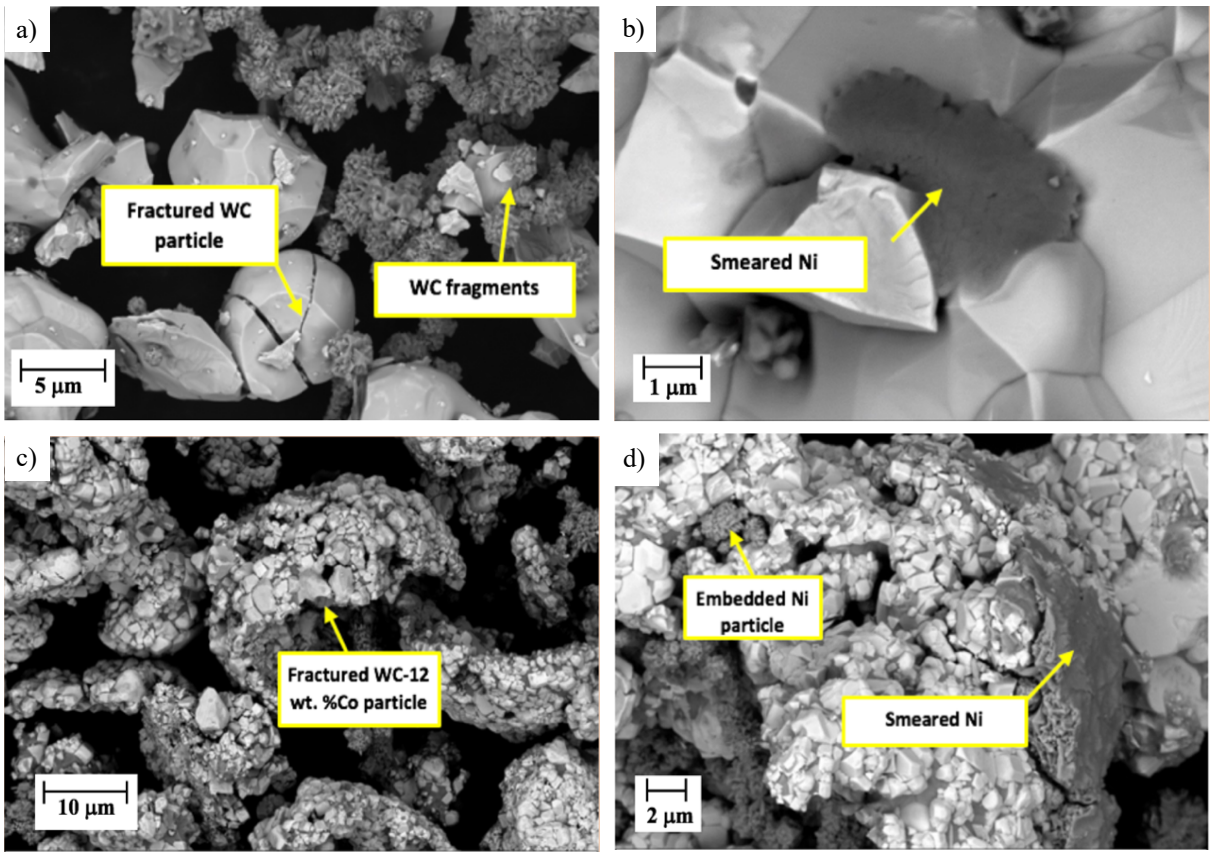

Figure 4.14: a) Fracture of the oxide reduced WC_{ox} particles; b) smearing of Ni onto the surface of the carbide particles as a result of milling process; c) fractured spherical and agglomerated WC_{12Co} particles; and (d) smeared and embedded Ni particles on the surface of the carbide particles as a resultant of milling process.

4.2. Parameter optimisation

This section highlights the results obtained from the Taguchi DoE technique used to determine the optimal spray parameters for the WC-Ni based powder combinations listed in *Table 3.1.* A signal-to-noise ratio (SNR) for each output response was calculated for the deposition parameter combinations used in this study. Refer to *Section C* of the *Appendix* for the formulas and full set of calculations.

4.2.1. Oxide-reduced WC_{ox}-Ni powders

Figure 4.15 summarize the SNR values of the coating hardness, coating thickness and the average between these two properties for each process parameter used to deposit the WC_{ox}-Ni based powders.

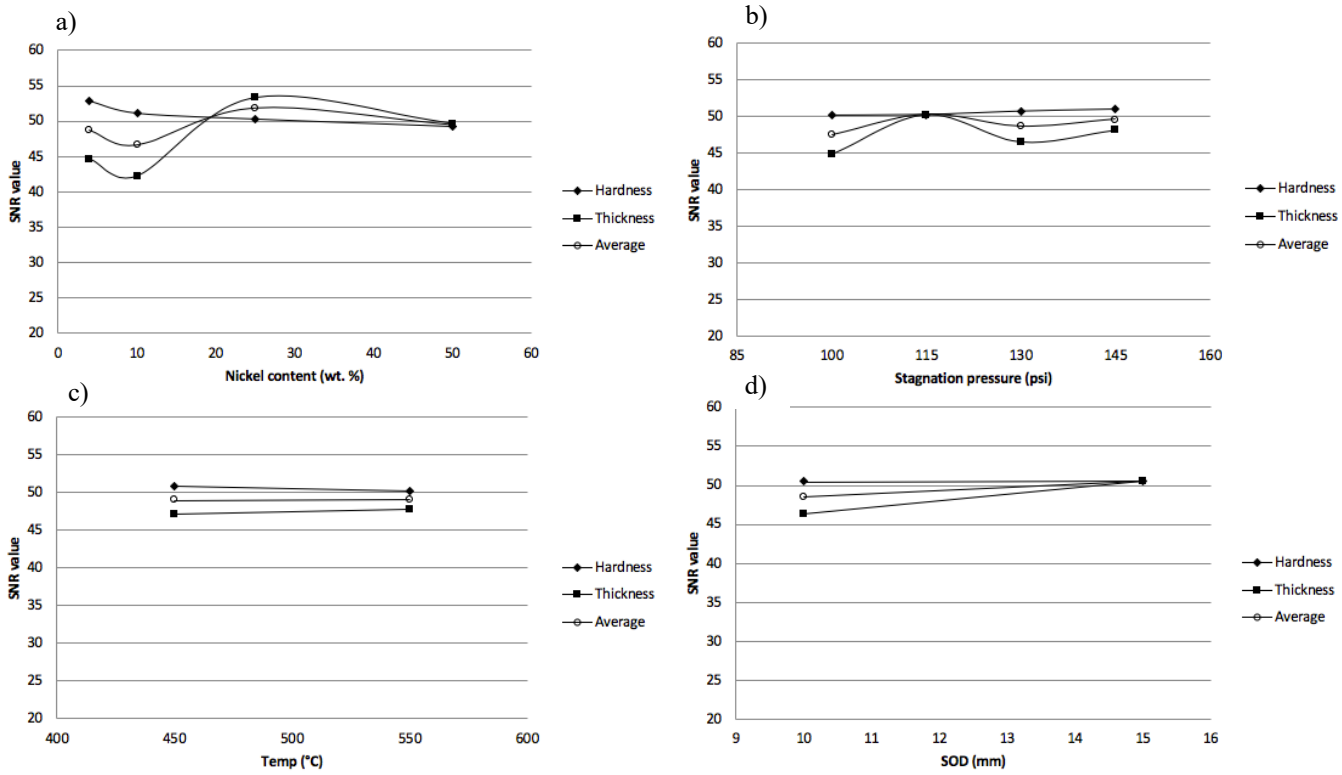

Figure 4.15: SNR values for the oxide-reduced WC_{ox} powder as a function of a) wt% Ni, b) stagnation pressure, c) temperature and d) standoff distance.

Figure 4.15 (a) represents the effect that the Ni content had on the coating thickness and hardness. From the graph, it can be deduced that the WC_{ox}-4Ni powder blend produced the hardest coatings. Further increases in the Ni content led to reduced coating hardness; this was expected as the Ni (210 HV [75]) binder was significantly softer than the oxide reduced WC_{ox} (2400 HV [3]) particles. A proportional relationship between the Ni content and coating thickness was also expected as higher binder contents lead to greater deposition efficiencies [43]. However, no distinct correlation was obtained as the WC_{ox}-10Ni powder produced the thinnest coatings while the WC_{ox}-25Ni powder resulted in the thickest coatings. From the average SNR result, a 25 wt% Ni content was the optimal parameter setting for both the coating hardness and thickness.

The coating hardness was proportional to the deposition pressure with a maximum setting of 145 psi resulting in the hardest coatings as observed in *Figure 4.15 (b).* The lowest pressure setting of 100 psi resulted in poor coating buildup as highlighted by the low SNR value, however, a slight increase in pressure to 115 psi produced the optimal coating thickness. Overall, a stagnation pressure of 115 psi was the optimal parameter setting for both the coating hardness and thickness.

The temperature settings of 450°C and 550°C had a minor impact on each of the output responses measured. A higher temperature setting of 550 °C had a positive impact on the coating thickness; however, was detrimental to the coating hardness of the oxide reduced WC-Ni based coatings. Overall, the combined effect of this input variable on the average SNR result was negligible as seen in *Figure 4.15 (c).*

The SOD settings of 10 and 15 mm had a minimal effect on the coating hardness; however, had an impact on the coating thickness, with a higher SOD of 15 mm being ideal for the latter property. Overall, a SOD of 15 mm away from the substrate was the optimal parameter setting for the deposition of the WC_{ox}-Ni based powders.

In summary, a Ni content of 25 wt% deposited using a stagnation pressure, deposition temperature and SOD of 115 psi, 550 °C and 15 mm respectively, yielded the optimal average hardness and thickness values for the WC_{ox}-xNi based coatings.

4.2.2. Spherical and agglomerated WC_{12Co}-Ni powders.

Figures 4.16 summarises the SNR values of the coating hardness, coating thickness and the average between these two properties, obtained for each process parameter used to deposit the spherical and agglomerated WC_{12Co}-Ni based powders.

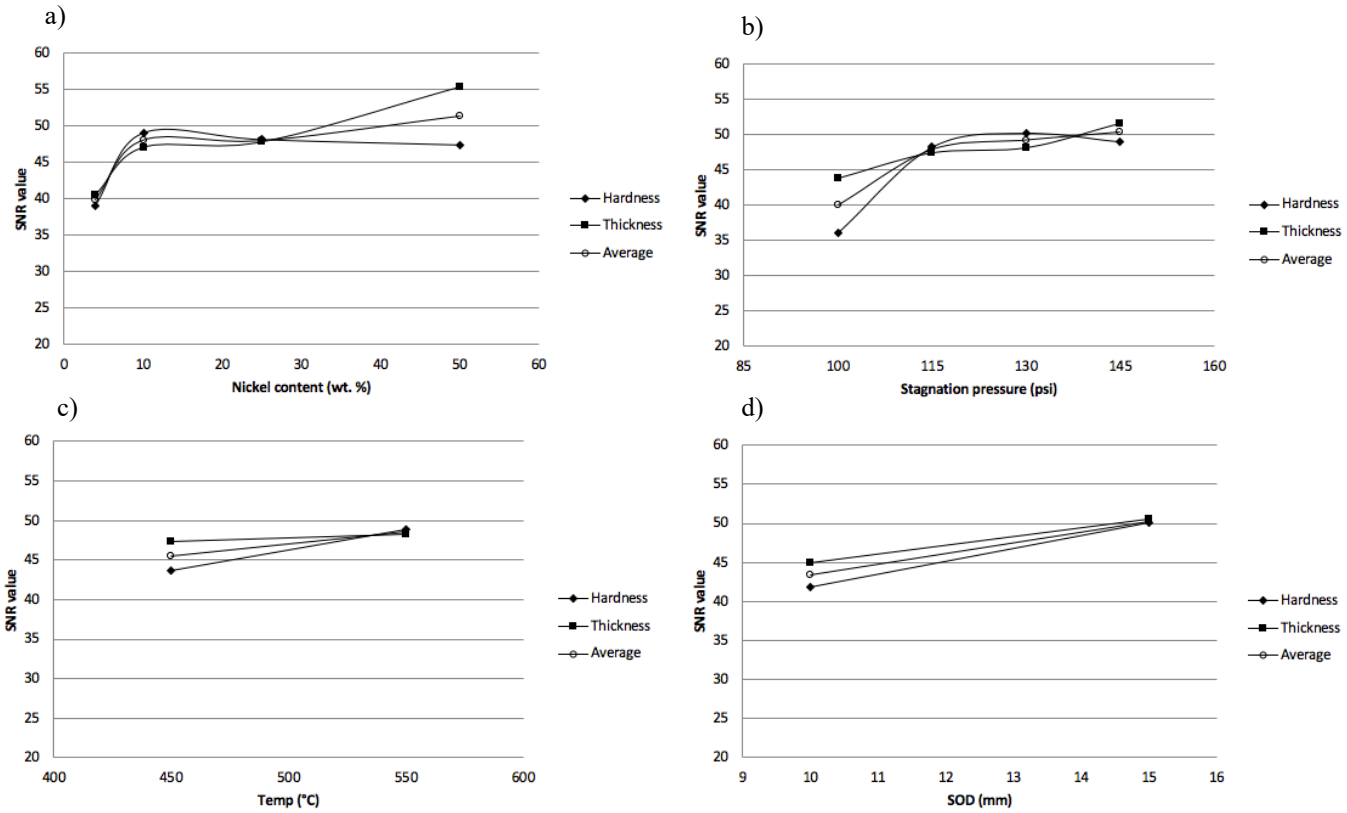

Figure 4.16: SNR values for the WC_{12Co} powder as a function of a) wt %Ni, b) stagnation pressure, c) temperature and d) standoff distance.

The graph presented in *Figure 4.16 (a)* indicates that increasing the Ni content above 4 wt% enhanced the coating buildup properties of the WC_{12Co} powder, with the 50 wt% Ni addition producing the thickest coatings. The effect of Ni additions on the coating hardness was not as conclusive as the hardness of the WC_{12Co}-10 Ni coating was higher than the one measured for the WC_{12Co}- 4 Ni composition. Overall, a 50 wt % Ni content was the optimal parameter setting for both the coating hardness and thickness as indicated in *Figure 4.16 (a)*.

The hardest WC_{12Co}-Ni based coatings were obtained at a pressure of 135 psi as indicated in *Figure 4.16 (b)*. Increasing the stagnation pressure had a positive effect on the coating thickness with the maximum thickness being obtained at 145 psi. Although the maximum coating hardness was obtained at 130 psi, the optimal parameter setting for both the coating hardness and thickness was 145 psi.

For the WC_{12Co}-Ni coatings, a higher deposition temperature of 550°C was ideal for both the coating thickness and hardness. Similarly to the oxide reduced WC_{ox}-Ni powder, a higher SOD setting of 15 mm was ideal for both the coating thickness and hardness of WC_{12Co}-Ni based coating, as seen in *Figure 4.16 (d)*.

In summary, a Ni content of 50 wt% deposited using a stagnation pressure, deposition temperature and SOD of 145 psi, 550 °C and 15 mm respectively, yielded the optimal average hardness and thickness values for the WC_{12Co}-xNi based coatings.

4.2.3. Spherical and agglomerated WC_{10Ni} -Ni powders

The suitable deposition of the as-received WC_{10Ni} powder, without additional Ni powder, could not be achieved due to the powder's inferior deposition properties which resulted in thin coatings as observed in *Figure 4.17*. Therefore, the coating thickness and hardness SNR calculations required for the optimization of this powder could only be based on the WC_{10Ni}-25Ni and WC_{10Ni}-50Ni powder combinations. The results are summarised in *Figure 4.18*.

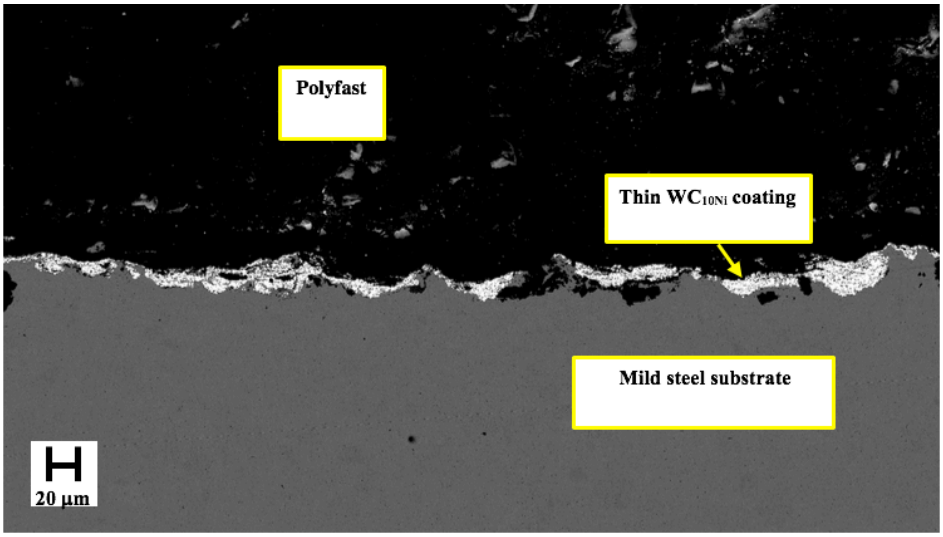

Figure 4.17: Cross section of the deposited as-received WC_{10Ni} coating, indicating the poor coating build-up properties of the powder.

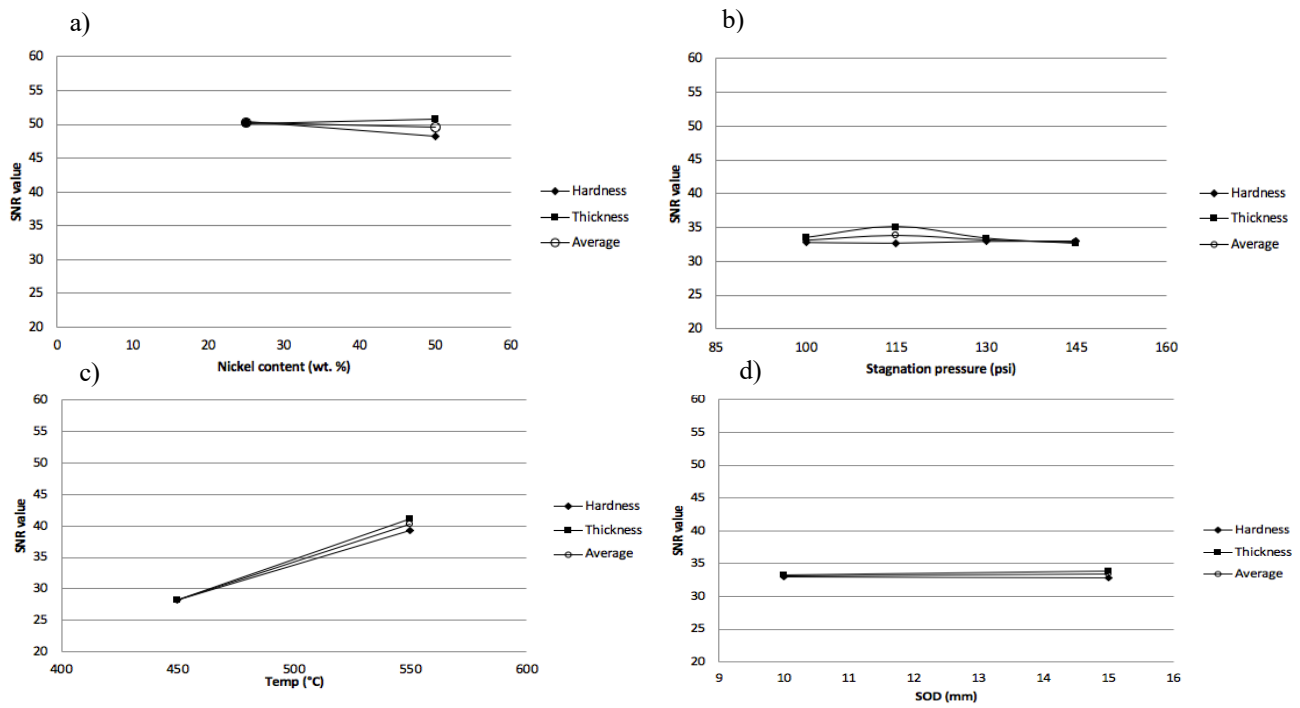

Figure 4.18: SNR values for the WC_{10Ni} powder as a function of a) wt %Ni, b) stagnation pressure, c) temperature and d) standoff distance.

Although the addition of Ni powder assisted in the deposition of the as-received WC_{10Ni} powder and resulted in superior coating build up, increasing the Ni content from 25 to 50 wt% Ni led to a decrease in the coating hardness as highlighted in *Figure 4.18 (a)*.

The variation in the stagnation pressures had a slightly higher impact on the coating thickness compared to the coating hardness of the WC_{10Ni} -Ni based powders as seen in the SNR values presented in *Figure 4.18 (b)*. Overall, a pressure setting of 115 psi resulted in the optimal parameter setting for both the coating hardness and thickness.

The deposition temperature had the most significant impact on the coating hardness and thickness of the WC_{10Ni} -Ni based powders, with a temperature setting of 550 °C being the most ideal for the two properties as seen in *Figure 4.18 (c)*. The SOD had a negligible effect on the measured coating properties, however, similarly to the WC_{ox}-Ni and WC_{12Co}-Ni powders, a higher SOD of 15 mm was more favourable.

In summary, a Ni content of 25 wt% deposited using a stagnation pressure, deposition temperature and SOD of 115 psi, 550 °C and 15 mm respectively, yielded the optimal average hardness and thickness values for the WC_{10Ni}-xNi based coatings.

4.2.4. Overall summary: Coating thickness and hardness

A summary of the optimal spray parameters obtained for each powder combination based on the calculated SNR data is presented in *Table 4.2* and illustrated in *Figure 4.19.* The values in bold represent the optimal settings for each WC-Ni based powder type.

Table 4.2: Summary of optimal spray parameters obtained from Taguchi DOE technique.

Mechanical blend	Pressure	Temperature	Standoff distance	Measured average coating hardness	Measured average coating thickness
	(psi)	(°C)	(mm)	HV	µm
WC_{ox}-4Ni	145	550	15	464 ± 15	422 ± 307
WC_{ox} -10Ni	115	450	15	361 ± 14	413 ± 148
WC_{ox} -25Ni	**115**	**550**	**15**	**349 ± 6**	**1005 ± 421**
WC_{ox} -50Ni	130	450	10	274 ± 6	443 ± 139
WC_{12Co}-4Ni	145	550	15	449 ± 0.4	273 ± 35
WC_{12Co}-10Ni	115	450	15	296 ± 64	469 ± 225
WC_{12Co}-25Ni	145	450	15	312 ± 18	664 ± 189
WC_{12Co}-50Ni	**145**	**550**	**15**	**232 ± 9**	**964 ± 457**
WC_{10Ni}	-	-	-	-	-
WC_{10Ni} -25Ni	**115**	**550**	**15**	**312 ± 7**	**3222 ± 210**
WC_{10Ni} -50Ni	115	550	15	257 ± 7	792 ± 276

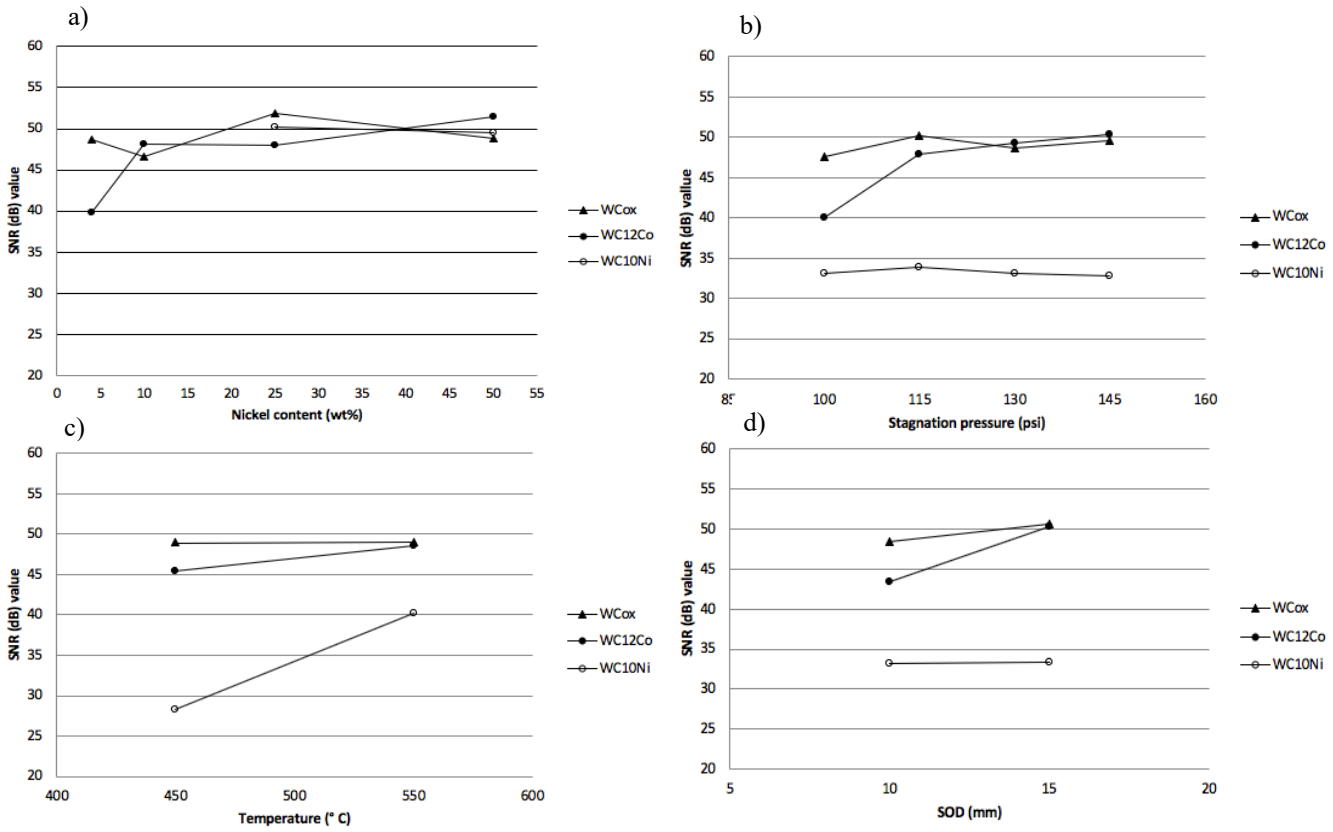

Figure 4.19: Comparison of the resultant SNR values obtained for coating thickness and coating hardness for each

feedstock powder.

4.2.5. Comparison of the experimental and theoretical coating thickness and hardness results

A summary of the experimental thickness and hardness data for the optimal WC_{ox}-25Ni, WC_{12Co}-50Ni and WC_{10Ni}-25Ni coatings, extracted from *Table 4.2* for ease of comparison, along with the theoretical data obtained using the Taguchi DoE and utility concept is presented in *Table 4.3*. As can be observed in the latter table, none of the coating thickness and hardness values obtained experimentally fell within the range predicted using the method. For the WC_{ox}-25Ni powder, both the experimental thickness and hardness values were higher than those predicted by the method and equation, while lower experimental hardness values were observed for both the WC_{12Co}-50Ni and WC_{10Ni}-25Ni coatings. The complete set of experimental data and the theoretical calculations for all the coatings can be found in *Section C* of the *Appendix*.

Table 4.3: Theoretical predictions vs. experimentally obtained output parameters of optimal powder combinations.

Powder composition	Experimental		Theoretical	
	Thickness (μm)	Hardness (HV_{300gf})	Thickness (μm)	Hardness (HV)
WC_{ox}-25Ni	1005 ± 421	349 ± 6	602-754	287-335
WC_{12Co}-50Ni	964 ± 457	232 ± 9	755-954	297-357
WC_{10Ni}-25Ni	3222 ± 210	312 ± 7	417-540	350-450

4.3. Coating microstructure and phase analyses

The XRD patterns of the powders and corresponding optimised coatings are depicted in *Figures 4.20 to 4.22.* It is evident from the patterns that no decarburization occurred in any of the coatings during deposition. In addition, peak broadening and phase changes are not evident from the patterns, implying that the chemical properties of the feedstock powders remained unchanged.

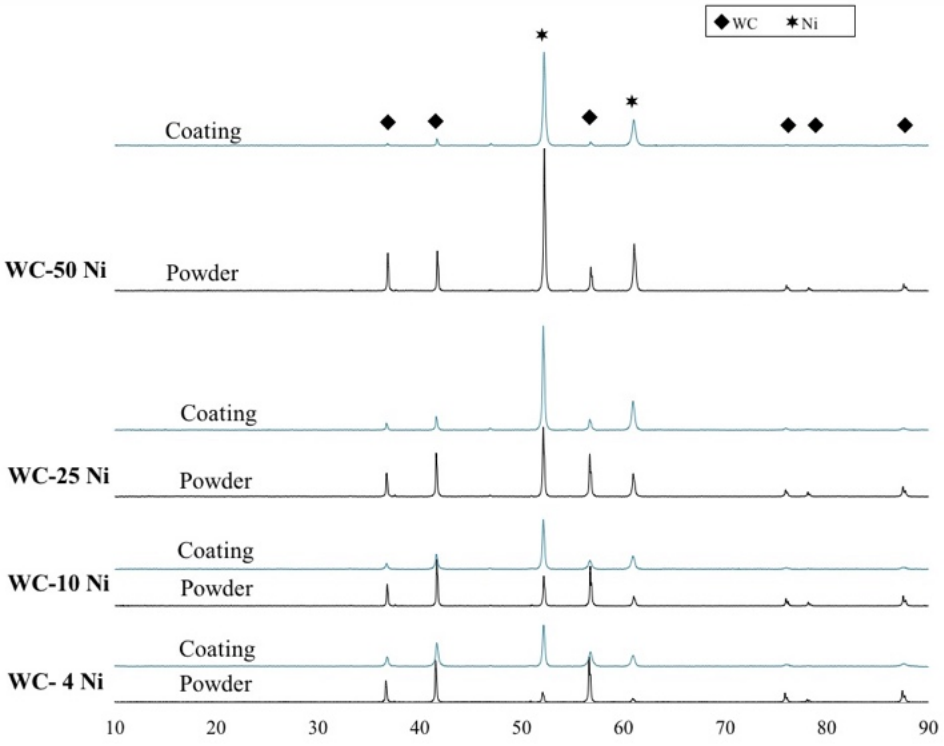

Figure 4.20: XRD patterns of the WC_{ox}-x wt.% Ni parent powders and corresponding coatings.

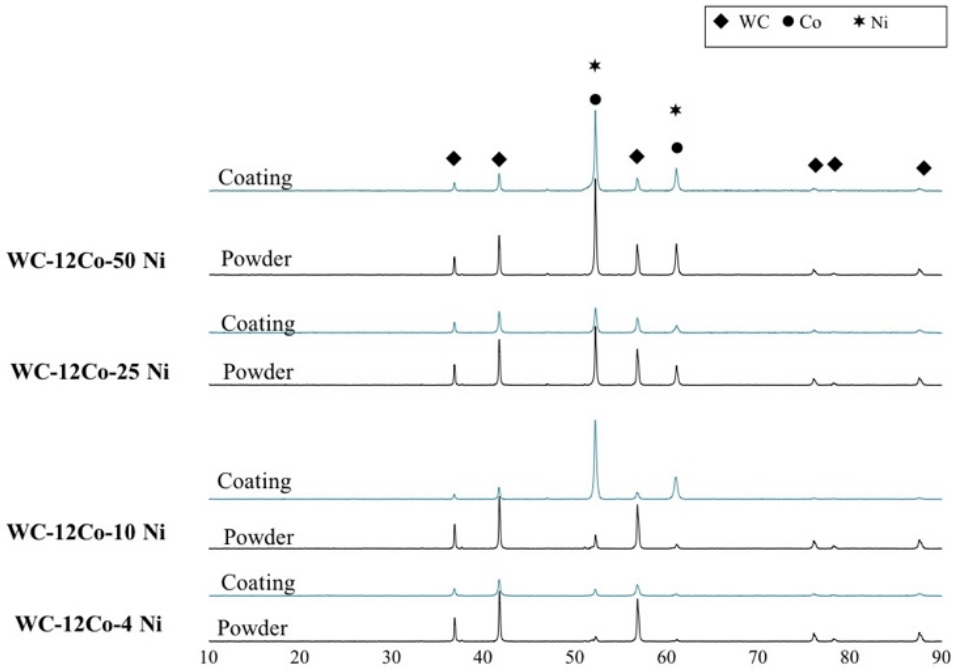

Figure 4.21: XRD patterns of the WC_{12Co}-xNi parent powders and corresponding coatings.

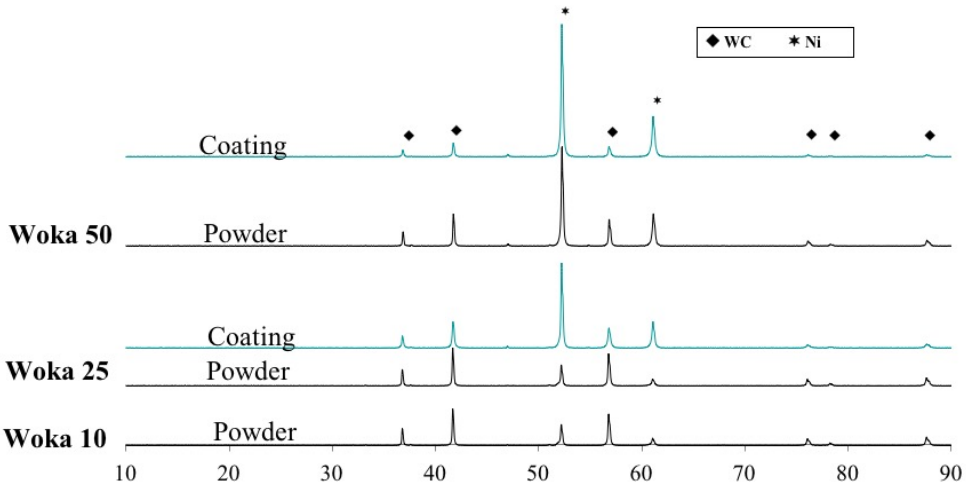

Figure 4.22: XRD patterns of the WC_{10Ni}-xNi parent powders and corresponding coatings.

The microstructures of the optimised coatings are shown in *Figure 4.23 (a)-(k)*. Superior coating build-up can be observed across all the WC-Ni based coatings, except for the as-received WC_{10Ni} powder which exhibited poor deposition properties (see *Figure 4.23 (i)*). Low pressure CGDS was able to produce coatings as thick as 3222 μm, as observed for the WC_{10Ni}-25Ni powder. A maximum thickness of 81 μm was obtained for the as-received WC_{10Ni} based coatings, further demonstrating its inferior adhesion properties in comparison to the other compositions. A non-homogenous distribution of the WC_{ox}, WC_{12Co} and WC_{10Ni} particles

(white phase) with some porosity (black phase) can be observed within the Ni matrix (grey phase) across all the coatings. These microstructures demonstrate that this technique can be used to deposit the carbide powders provided that they are co-deposited with a suitable ductile binder in the form of a metal matrix composite (MMC).

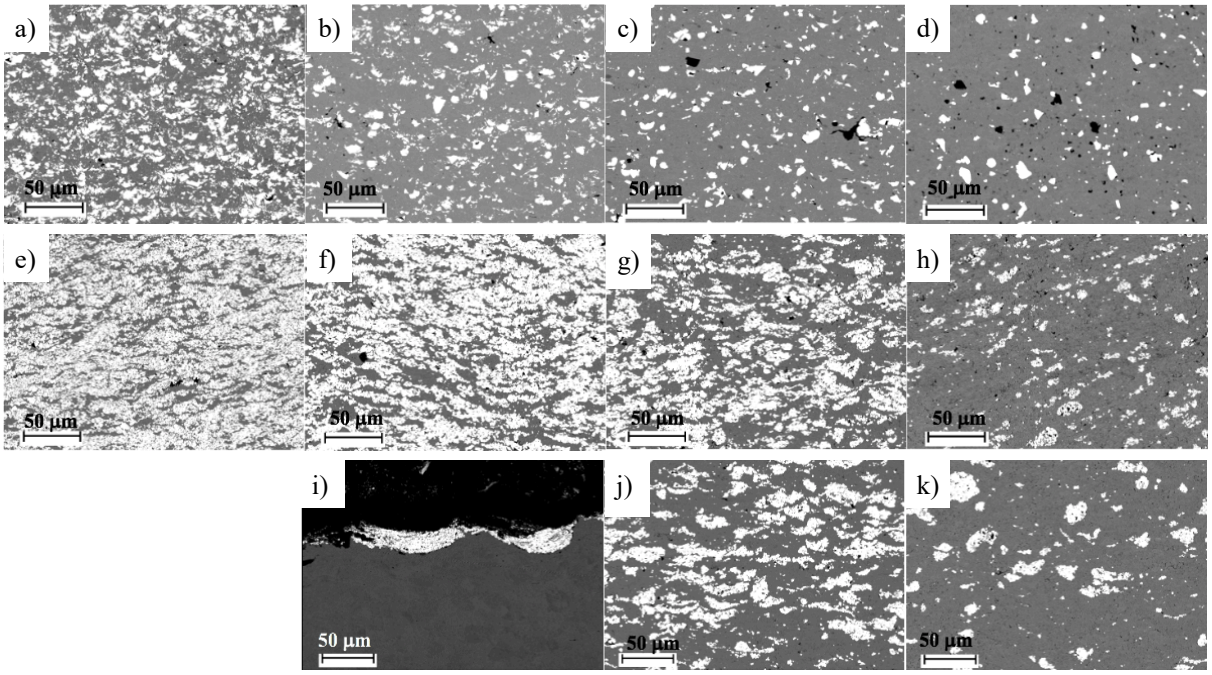

Figure 4.23: Microstructure of (a) WC_{ox}-4Ni, (b) WC_{ox}-10Ni, (c) WC_{ox}-25 Ni, (d) WC_{ox}-50Ni, (e) WC_{12Co}-4Ni, (f) WC_{12Co}-10Ni, (g) WC_{12Co}-25 Ni, (h) WC_{12Co}-50Ni, (i) WC_{10Ni} (as-received), (j) WC_{10Ni} -25Ni and (k) WC_{10Ni}-50 Ni coatings. White phase = WC, light gray phase = Co, dark gray phase = Ni matrix.

Elemental mapping of WC_{ox}-25Ni, WC_{12Co}-25Ni and WC_{10Ni}-25Ni coatings presented in *Figures 4.24 – 4.26* reveal that no atomic diffusion took place at the coating-substrate interphase during deposition.

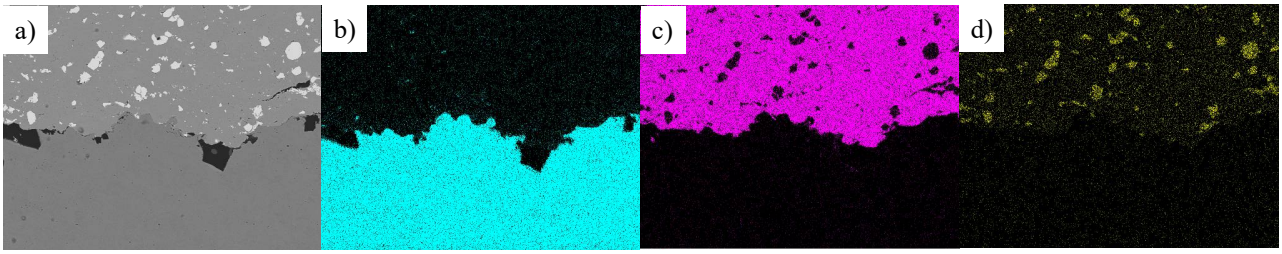

Figure 4.24: Elemental composition maps of the WC_{ox}-25Ni coating. (a) cross-sectional microstructure, (b) Fe, (c) Ni and (d) W.

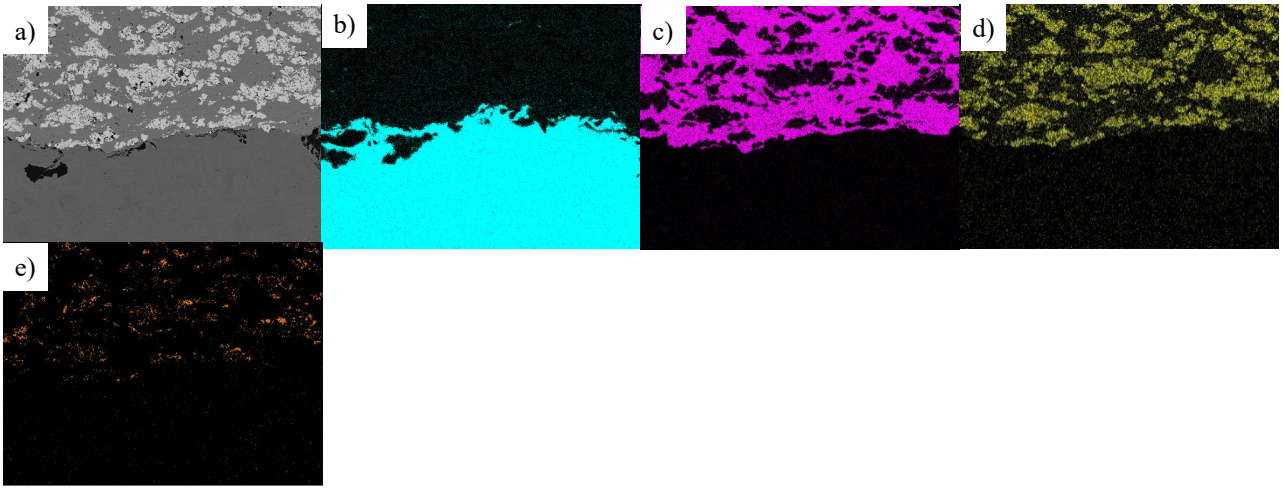

Figure 4.25: Elemental composition maps of the WC_{12Co}-25Ni coating. (a) cross-sectional microstructure, (b) Fe, (c) Ni, (d) W and (e) Co.

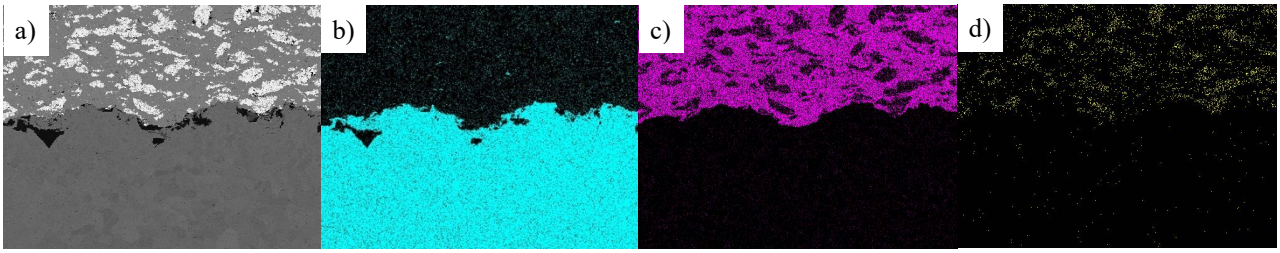

Figure 4.26: Elemental composition maps of WC_{10Ni}-25Ni coating. (a) cross-sectional microstructure. (b) Fe, (c) W and (d)Ni.

Table 4.4 lists the percentage WC retained, calculated porosity and Ni binder mean free path of all the coatings.

Table 4.4: Summary of resultant WC_{ox}-xNi, WC_{12Co}-xNi and WC_{10Ni}-xNi coating properties.

Mechanical blend	Optimal deposition parameters		
	% Porosity	BMFP (µm)	% WC retained
WC_{ox}-4Ni	1.47	5.42	39.89
WC_{ox} -10Ni	2.27	12.54	24.47
WC_{ox} -25Ni	2.70	21.21	17.07
WC_{ox} -50Ni	2.49	48.59	6.92
WC_{12Co}-4Ni	3.51	1.77	74.08
WC_{12Co}-10Ni	3.15	3.10	63.54
WC_{12Co}-25Ni	3.79	4.85	47.92
WC_{12Co}-50Ni	5.11	10.09	27.06
WC_{10Ni}-25Ni	1.22	6.82	35.77
WC_{10Ni}-50Ni	1.55	11.58	16.49

The WC_{ox}-4Ni *Figure 4.23 (a)*], WC_{12Co}-4Ni [*Figure 4.23 (e)]* and the as-received WC_{10Ni} [*Figure. 4.23 (i)*] coatings were able to retain the most carbide particles with the WC_{12Co}-4Ni composition retaining the highest percentage of 74.08 wt% WC. These figures also illustrate that the spherical and agglomerated WC_{12Co} and WC_{10Ni} powders were able to retain more carbide particles than the oxide reduced WC_{ox} powders even at comparable Ni contents.

The 4 wt% Ni addition of the powders yielded the hardest coatings with the WC_{ox}-4Ni combination possessing the highest hardness (496 ± 24 $HV_{0.3}$) of all the coatings. Increasing the Ni content led to a decrease in the coating hardness (see *Table 4.2*) which can also be correlated to the percentage of WC retained and binder mean free path values of the coatings. Overall, the spherical and agglomerated type WC_{12Co}-xNi and WC_{10Ni} -xNi based coatings had shorter binder mean free path distances in comparison to the oxide reduced WC_{ox}-xNi coatings even at similar Ni contents. The WC_{12Co}-xNi type powders yielded the most porous coatings (black phase) in contrast to the WC_{ox}-xNi and the WC_{10Ni} -xNi coatings. It was also observed that increasing the Ni content in the starting powders resulted in increased coating porosity. The exceptions to this trend were the higher porosity values obtained for WC_{ox}-25Ni compared to WC_{ox}-50Ni, and a higher porosity for the WC_{12Co}-4Ni compared to the WC_{12Co}-10Ni powder combinations.

4.4. Characterisation of the TiC and Mo-based coatings

In *Chapter 3, Section 3.1* it was stated that 1 wt% Mo and 10 wt% TiC powders would be added to the best WC-Ni-based coating in an attempt to improve the erosion and corrosion properties of the selected coating. Based on the optimisation results, the oxide-reduced WC_{ox}-4Ni coating had the highest hardness of 496 ± 24 HV and a coating thickness of 422 ± 307 µm, and was thus selected for this part of the study. The measured properties of the 4 coating compositions are summarised in *Table 4.5*.

Table 4.5: Summary of resultant WC_{ox}-4Ni, WC_{ox}-4Ni-1Mo, WC_{ox}-4Ni-10TiC and WC_{ox}-4Ni-1Mo-10TiC coating properties.

Mechanical blend	**Average coating thickness (µm)**	**Average coating hardness (HV0.3)**	**% Retained**			
			WC	**Ni**	**TiC**	**Mo**
WC_{ox}-4Ni	422 ±307	496 ± 24	39.89	60.11	-	-
WC_{ox}-4Ni-1Mo	81 ±19	557 ±39	42.25	44.41	-	0.73
WC_{ox}-4Ni-10TiC	278 ±178	515 ±8	34.06	53.59	4.44	-
WC_{ox}-4Ni-1Mo-10TiC	541 ±315	528 ±26	31.70	55.68	5.63	1.57

The addition of Mo (475 HV [84]) and TiC (3200 HV [85]) caused an increase in the average hardness of the WC_{ox}-4Ni based coatings. The WC_{ox}-4Ni-1Mo coatings were the hardest of the 4 powder combinations and retained the highest amount of WC at 42.25 wt%. The combined effect of the Mo and TiC resulted in the thickest coatings with a relatively high hardness. Good coating build-up was observed across three of the four coatings as indicated in *Tables 4.5* and *Figure 4.27,* with the exception of the WC_{ox}-4Ni-1Mo coating which showed poor deposition properties and coating delamination. It should be noted that a high standard deviation in the values of the coating thickness was observed across all compositions. The black phases dispersed throughout the coatings in *Figures 4.27 (c)* and *(d)* are due to the TiC powder particles embedded within the Ni matrix. The porosity of these coatings could not be accurately determined using the technique described in *Section 3.4.25* of *Chapter 3* as both the pores and TiC particles embedded within the coating appeared black in the FESEM micrographs.

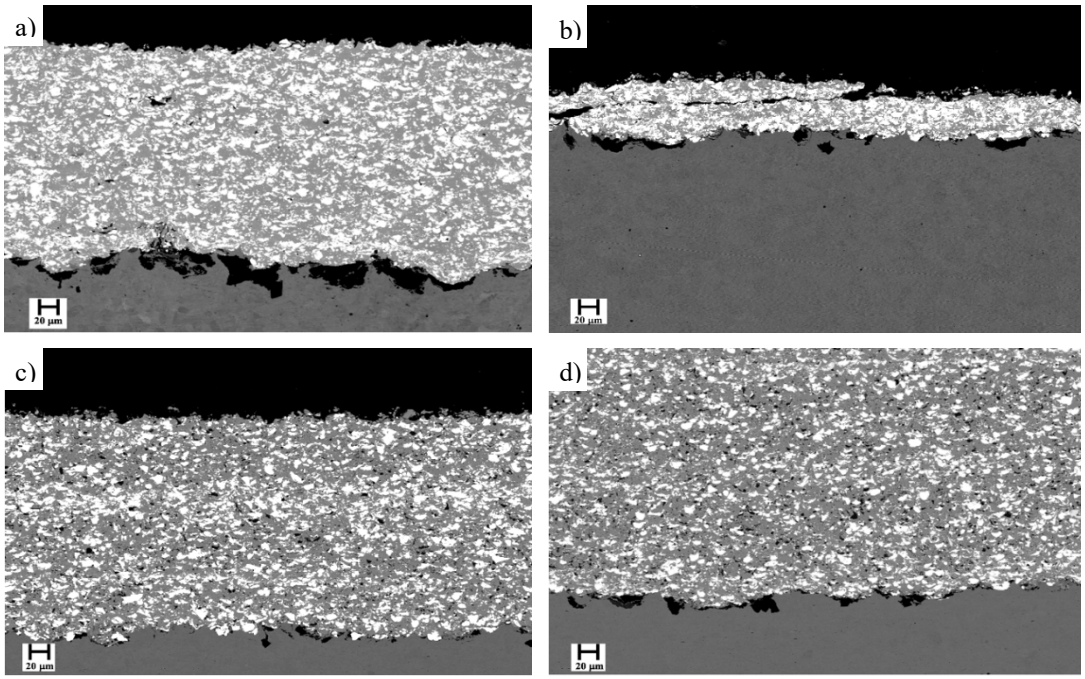

Figure 4.27: Microstructure of the resultant a) WC_{ox}-4Ni ; b) WC_{ox}-4Ni-1Mo ; c) WC_{ox}-4Ni-10TiC and d) WC_{ox}-4Ni-1Mo-10TiC coatings compositions.

The XRD patterns of the powders and corresponding coatings are depicted in *Figures 4.28 to 4.30.* Similarly to the patterns reported in *Section 4.1*, no decarburization occurred in any of the coatings during deposition. In addition, peak broadening and phase changes were not evident from the patterns, implying that the chemical properties of the feedstock powders remained unchanged.

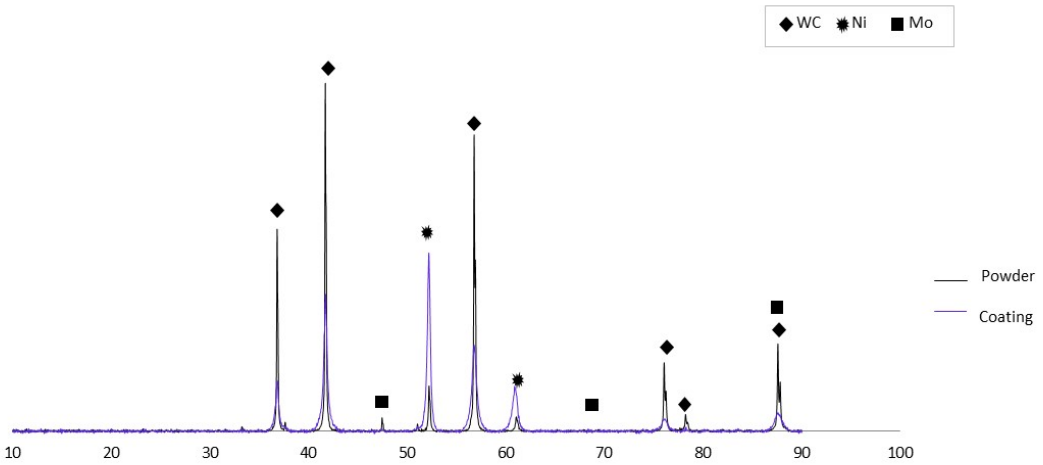

Figure 4.28: XRD patterns of the WC_{ox}-4Ni-1Mo parent powder and corresponding coating.

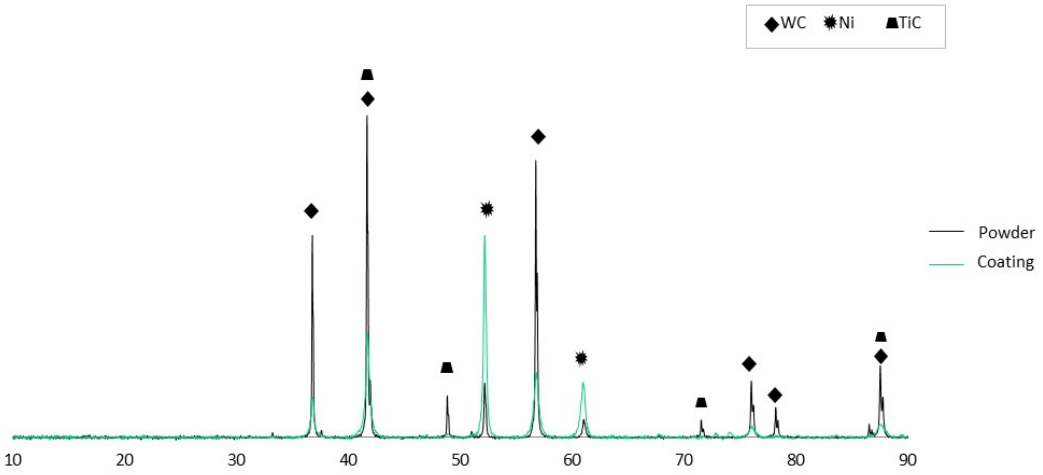

Figure 4.29: XRD patterns of the WC_{ox}-4Ni-10TiC parent powder and corresponding coating.

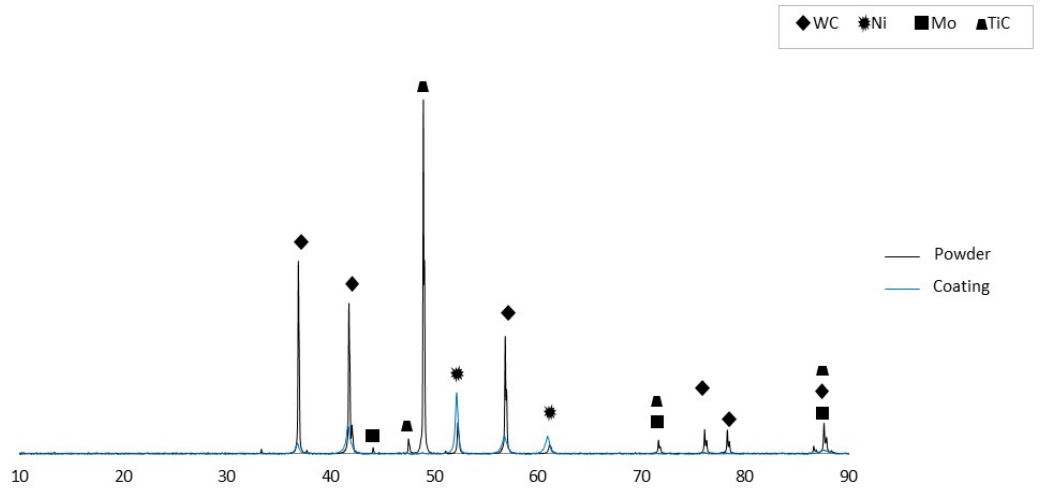

Figure 4.30: XRD patterns of the WC_{ox}-4Ni-1Mo-10TiC parent powder and corresponding coating.

Although the hardness properties of the WC_{ox}-4Ni-1Mo coatings was comparable to the other three coatings this composition was eliminated from the subsequent erosion and corrosion testing due to its inferior coating integrity and build-up properties. The remaining three coatings were then assessed in terms of slurry erosion and corrosion properties.

4.5. Slurry erosion testing

Slurry erosion tests were conducted on three coating compositions namely, WC_{ox}-4Ni, WC_{ox}-4Ni-10 TiC and the WC_{ox}-4Ni-1Mo-10TiC, the justification for the choice of composition was mentioned in *Section 4.4*. The average cumulative mass loss experienced by the coatings and the average wear rates are presented in *Figures 4.31* and *4.32* respectively.

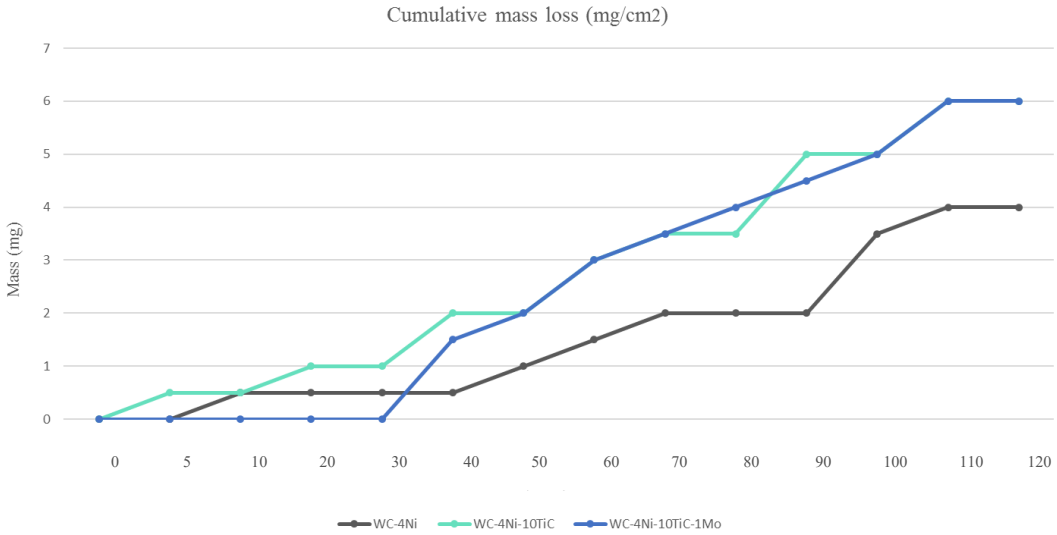

Figure 4.31: Cumulative mass loss per unit area of the optimal WC_{ox}-4Ni based coatings.

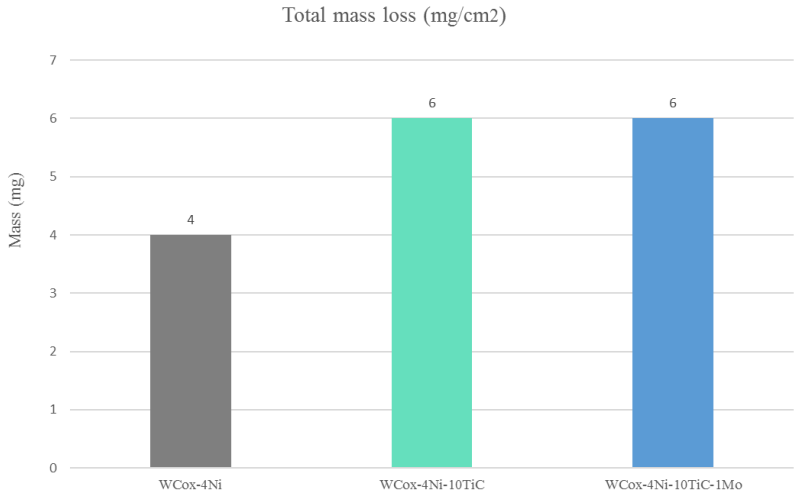

Figure 4.32: Average total mass loss per unit area of the optimal WC_{ox}-4Ni based coatings.

It can be noted that the WC_{ox}-4Ni coatings had the highest wear resistance out of the 3 combinations as it resulted in the least total mass loss of 4 mg/cm^2. The performance of the WC_{ox}-4Ni-10TiC and the WC_{ox}-4Ni-1Mo-10TiC coatings during the wear tests was similar as a total mass loss of 6 mg/cm^2 (*Figure 4.32)* was obtained for both coatings, and their respective cumulative mass loss graphs were comparable as illustrated in *Figure 4.31*. It can also be deduced that the addition of 1 wt% Mo to the WC_{ox} -4Ni -10TiC did not affect the total mass loss of the coatings. However, it did increase the wear resistance of break-in period of the WC_{ox}-4Ni-1Mo-10TiC coating as this composition experienced no mass loss for the first 30 mins of the test, in contrast to the other 2 compositions as observed in *Figure 4.31*.

Figures 4.33 – 4.35 represent FESEM images of the eroded coating surfaces. Damage to the carbide particles and Ni matrix can be observed across all three coating compositions. Two distinct modes of erosion can be identified, namely erosion by brittle fracture and plastic deformation. Brittle erosion is characterised by severe particle fracture and the detachment of the carbide particles from the Ni matrix [49] as observed in the backscatter electron FESEM micrographs of all the eroded coatings [*Figures 4.33-4.35 (a)*]. Scratching, ploughing and cutting within the ductile Ni matrix can also be noticed across all coating compositions which is indicative of erosion by plastic deformation [49] which was more apparent in the secondary electron FESEM micrographs [*Figures 4.33-4.35 (b)*].

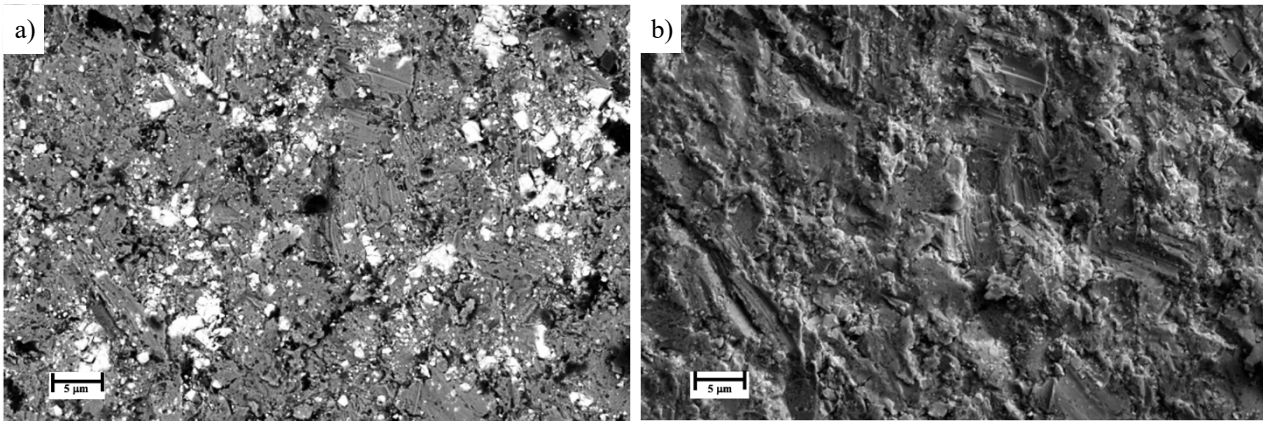

Figure 4.33: (a) Backscatter and; (b) secondary electron FESEM micrographs of the eroded WC_{ox}-4Ni surface.

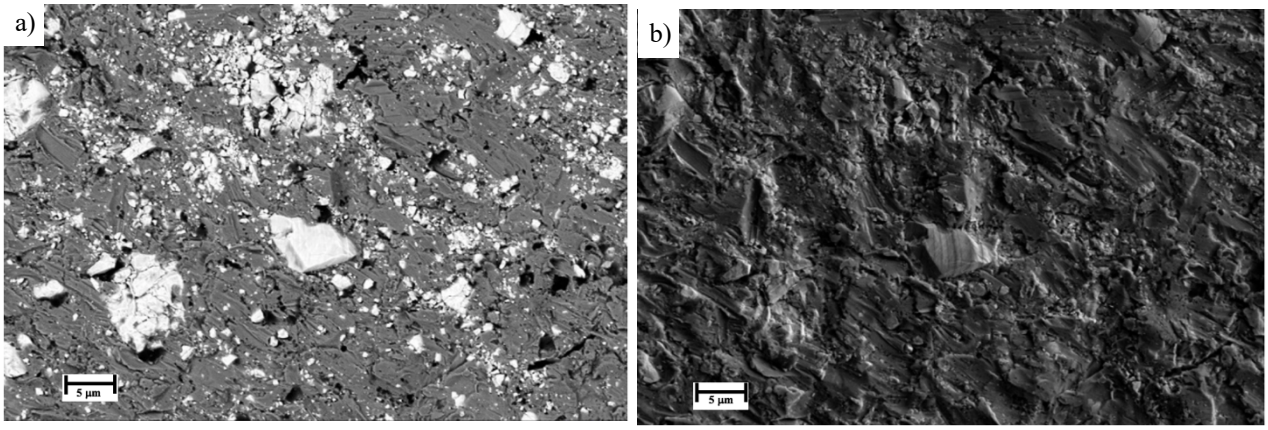

Figure 4.34: (a) Backscatter and; (b) secondary electron FESEM micrographs of the eroded WC_{ox}-4Ni-10TiC surface.

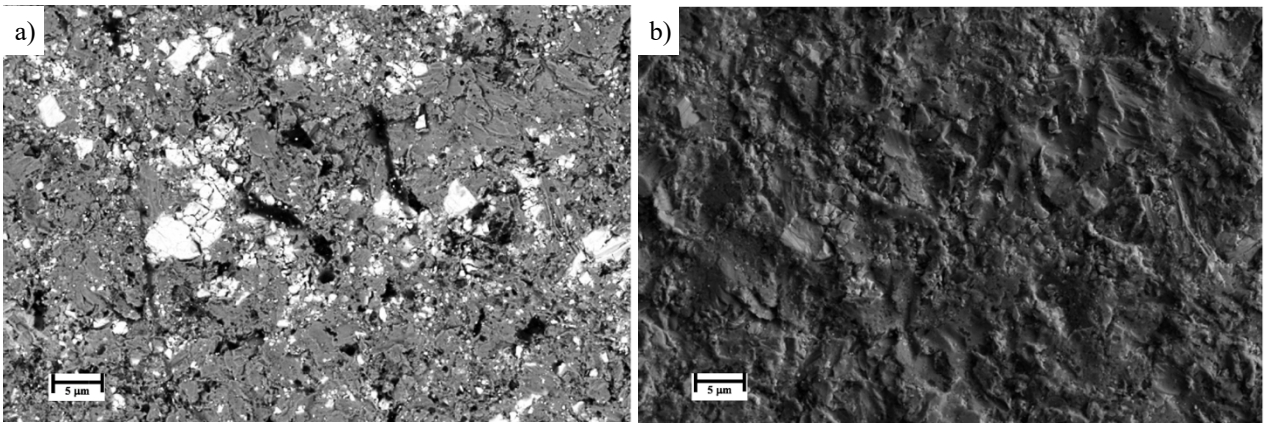

Figure 4.35: (a) Backscatter and; (b) secondary electron FESEM micrographs of the eroded WC_{ox} -4Ni-1Mo-10TiC surface.

4.6. Corrosion testing

The three coatings which were subjected to slurry erosion testing were also tested for corrosion resistance. A summary of the main corrosion results is presented in *Table 4.6* with *Figures 4.36 - 4.39* illustrating the main relationships.

Table 4.6: Summary of the coating corrosion properties.

	WC_{ox}-4Ni	**WC_{ox}-4Ni-10TiC**	**WC_{ox}-4Ni-1Mo-10TiC**
OCP (V)	0.47	0.44	0.42
E_{corr} (V)	0.33	0.30	0.28
i_{corr} (A/cm^2)	0.34	0.38	0.44
CR (mm/yr)	22.18	25.08	28.79

Figure 4.36 represents a plot of each coating's measured potential when no external voltage or current was applied over a period of 12-hours. The WC_{ox}-4Ni coatings had the highest open circuit potential (OCP) value of 0.47 V, followed by the WC_{ox}-4Ni-10TiC (0.44 V) and then the WC_{ox}-4Ni-1Mo-10TiC (0.42V) composition. The high OCP values for the WC_{ox}-4Ni coatings indicate that this composition was the most noble, while the WC_{ox}-4Ni-1Mo-10TiC was most susceptible to corrosion in tap water. The WC_{ox}-4Ni composition was, however, unstable in the solution as noted by the initial erratic potential values, which only stabilized after 22000 seconds (6 hours and 6 mins). On the contrary, the WC_{ox}-4Ni-10TiC and WC_{ox}-4Ni-1Mo-10TiC coatings did not display any signs of erratic chemical behaviour within the

solution. Overall, the OCP values of all 3 coatings steadily increased with time even once stability within the electrolyte had been achieved.

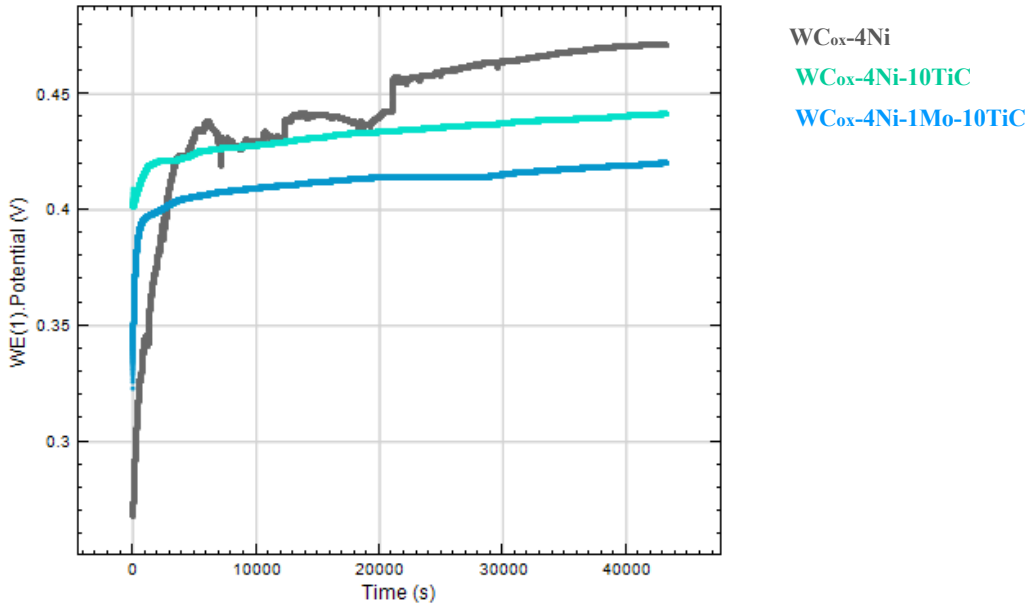

Figure 4.36: OCP plots of the optimal WC_{ox}-4Ni based coatings in tap water at 25°C.

The polarization plots of the 3 coating compositions, in which an external voltage from -0.8 V to 1.2 V was applied, are presented in *Figure 4.37*. From the graphs, it appears that the E_{corr} and corresponding i_{corr} values of the coatings were quite similar. However, the values calculated using the Tafel extrapolation method indicate that the WC_{ox}-4Ni coating was the most resistant as this composition had the highest E_{corr} (0.33 V) and lowest i_{corr} (0.34 A/cm^2) values. The WC_{ox}-4Ni-10TiC, followed by the WC_{ox}-4Ni-1Mo-10TiC were the more chemically active in tap water as confirmed by the OCP values discussed previously. It can also be noticed that the anodic reactions of the all 3 compositions were quite similar. However, around an applied voltage of 0.65 V, the cathodic response of the WC_{ox}-4Ni-1Mo-10TiC coatings differed from the WC_{ox}-4Ni and WC_{ox}-4Ni-10TiC compositions. This behavior is more evident in the graph presented in *Figure 4.38* and can be attributed to the addition of Mo.

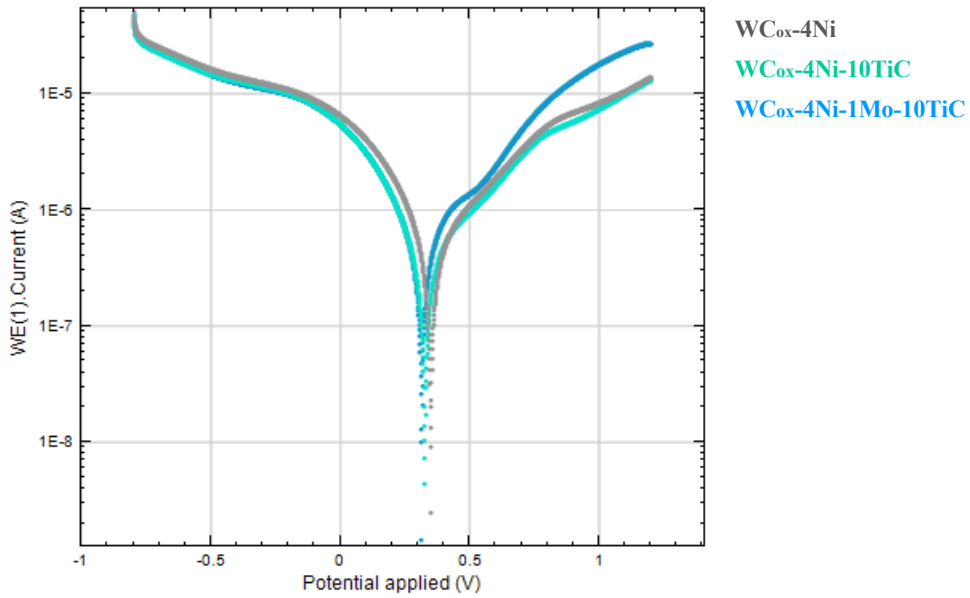

Figure 4.37: Polarization plots of optimal WC_{ox}-4Ni based coatings in tap water at 25°C.

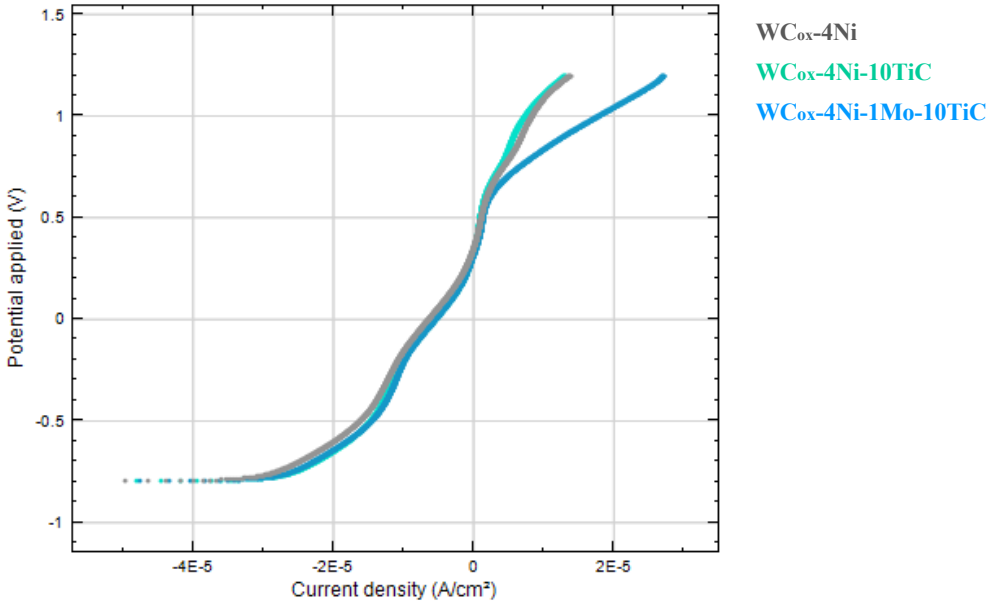

Figure 4.38: Potential vs current density plot of optimal WC_{ox}-4Ni based coatings in tap water at 25°C.

According to literature, the current density can be correlated to the corrosion rate [58,62,63]. The current density measurements of each composition after a 12-hour submersion in tap water are presented in *Figure 4.39*. The WC_{ox}-4Ni coatings had the lowest current density values and corrosion rate of 22.18 mm/yr (see *Table 4.6*), again validating it as the most corrosion resistant composition.

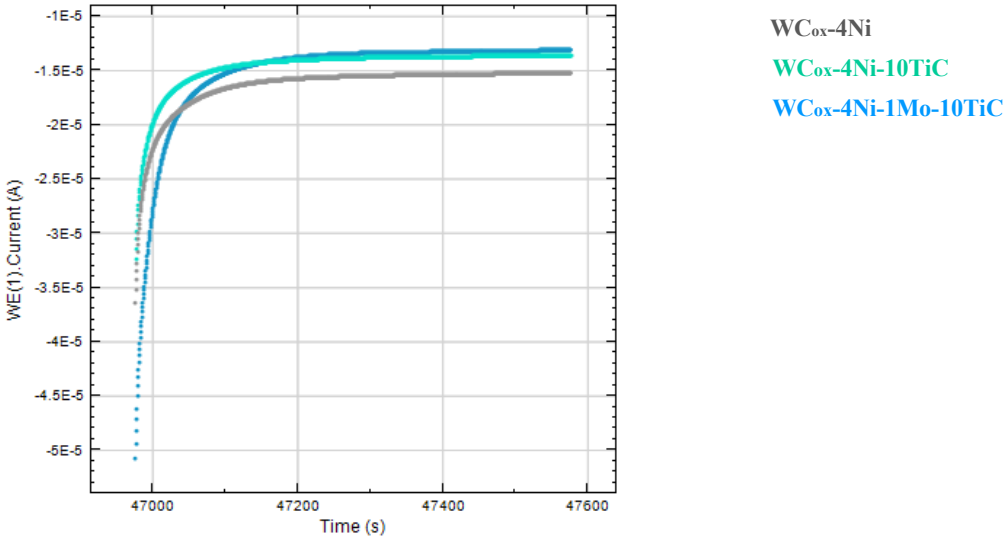

Figure 4.39: Current density vs time plots of optimal WC_{ox}-Ni based coatings in tap water at 25°C.

SEM micrographs of the corroded surface do not show any signs of damage to the Ni or carbide phases, however, several types of contaminants can be observed in *Figures 4.40-4.41*.

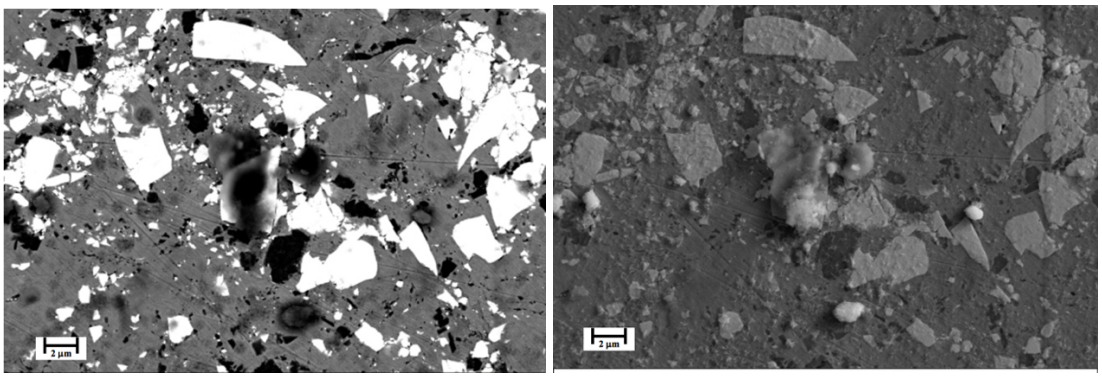

Figure 4.40: Backscatter and Secondary electron SEM micrographs of the WC_{ox}-4Ni-10TiC based coating subsequent to corrosion testing.

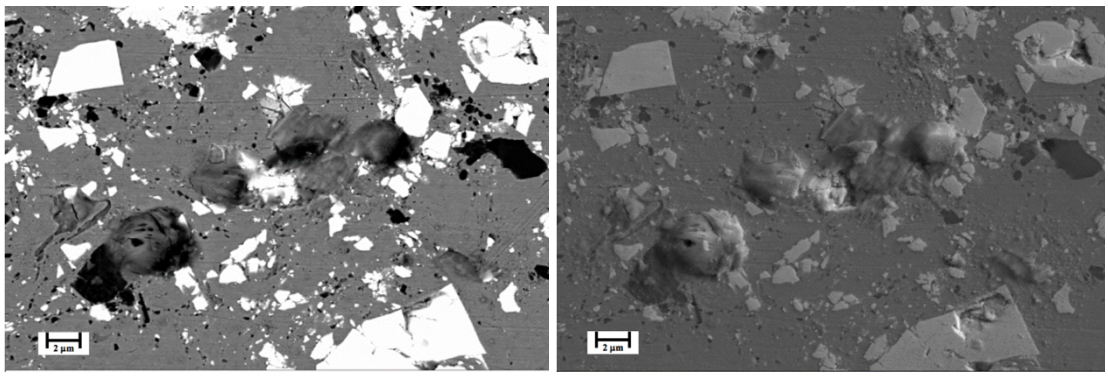

Figure 4.41: Backscatter and Secondary electron SEM micrographs of the WC_{ox} -4Ni-1-Mo-10TiC based coating subsequent to corrosion testing.

5. Discussion

This chapter provides an in-depth analysis of the results obtained in *Chapter 4*.

5.1. Feasibility of the Taguchi Mixed-level DoE technique in the selection of the optimized deposition parameters.

The Taguchi DoE technique proved to be an efficient method for determining the optimal deposition parameters for each powder composition. Without the use of the technique, a total of 64 spray combinations would have had to be tested, requiring the fabrication of 528 coatings (see *Section C* of the *Appendix* for the calculations). This experimental route would have been time-consuming, resource-intensive and resulted in large sets of data that would have been complex to interpret.

DoE techniques also enable investigators to gain an understanding of how the system under study works as the relationships between some of the factors and the response variables were not intuitive. For example, a proportional relationship between the Ni content and thickness across all the WC-Ni based coatings was expected as higher binder contents lead to greater deposition efficiencies [43]. However, this trend was not observed for the WC_{ox} -Ni coatings as the WC_{ox}-10Ni powder produced the thinnest coatings while the WC_{ox}-25Ni powder resulted in the thickest coatings. Similarly, the effect of Ni additions on the coating hardness was not conclusive as the hardness of the WC_{12Co}-10 Ni coating was higher than the one measured for the WC_{12Co}- 4 Ni composition. Other examples of this non-intuitive behaviour were discussed in *Section 4.2*. of the *Results* chapter.

The Taguchi DoE technique in conjunction with the utility concept also enables investigators to predict the optimal coating thickness and hardness values. However, for the system under study, neither the coating thickness nor the hardness values obtained experimentally fell within the ranges predicted by the method as observed in *Table 4.2* of the *Results* chapter. For the WC_{ox}-25Ni powder, both the experimental thickness and hardness values were greater than those predicted by the method, while lower experimental hardness values were observed for the WC_{12Co}-50Ni and WC_{10Ni}-25Ni coatings.

There are several probable reasons for the deviation in the predicted results. Firstly, the Taguchi DoE technique has been criticised for its difficulty to accurately account for the interactions between parameters. According to literature, if the levels within a factor are too large, then excessive, non-additive effects will arise and make the functions under investigation more complex [86]. Vital information regarding the interactions of the parameters and their effect on the response variables may also be missed. However, if the levels are too small, the variation from other sources increases the dataset, further complicating the interpretation of results and ultimately decreasing the efficiency of the DoE technique. Errors in the selected size range of the levels used in this study may have contributed to the failed predictions. It is proposed by Whitcomb and Anderson [86] that when applying the Taguchi technique, the factor levels selected for the experiments be adjusted to bring the predicted values closer to the target, reducing the variability [86-87]. An iterative application of the method should, therefore, be applied until convergence between the predicted and experimental values is obtained.

Secondly, certain researchers have criticised the technique stating that, since the Taguchi DoE technique is an offline method, it, therefore, cannot be applied to dynamic systems such as the one under study [87]. The strain hardening of the cold spray coatings can be considered as dynamic due to the shot peening effect that takes place when the hard WC particles continuously impact the coatings during deposition [88].

Thirdly, the cold spray system also failed to produce repeatable results, as seen in the high standard deviation values of the measured response variables (see *Section C* of the *Appendix*), even for those deposited under identical spray conditions. During coating deposition, it was noted that the non-pressurized gravitational vibratory powder feeder used to inject the powder into the system did not supply a consistent mass flowrate of powder which ultimately affected the deposition and coating characteristics. This challenge was minimized by carefully observing the flow of the powders through the feeder and stopping all machine operations when the powder flow rate was inconsistent. However, for more consistent powder flow, it is recommended that an external powder feeder fitted with a flow meter be used for increased powder injection control. In the Taguchi DoE technique, it is essential that the response variables being measured be precise and repeatable as these ultimately affect the SNR calculations [67-69,71-73].

However, there are examples where the technique produced accurate predictions. Goyal et al. [71] used a similar Taguchi DOE technique on a low-pressure CGDS system to determine the optimal deposition parameters yielding the thickest copper coatings. The average coating thickness was found to be 72.36 mm which fell within the confidence interval (CI) of the predicted optimal coating thickness values as indicated in *Equation 5.1* below. It can, therefore, be recommended that the technique be used as a guideline rather than a standard for determining the optimal parameters for a multivariable, multilevel system [71].

$$\text{CI: } 71.69 < \mu < 74.13 \text{ mm} \qquad \text{Equation 5.1 [71].}$$

The deposition parameters determined by the Taguchi DoE technique also influenced the resultant coating properties. According to work conducted by Phani et al. [89], the temperature of the inlet gas temperature is the most influential parameter on the coating properties followed by stagnation pressure and standoff distance, due to its drastic effect on particle velocity. Increasing the gas temperature has a minimal effect on the particle deposition temperature as the energy is expended on accelerating the particles to higher velocities. Upon heating, the gas rapidly expands in the divergent nozzle which results in higher in-flight and impact velocities [17,89]. The stagnation pressure applied during deposition also has a considerable influence on the coating properties, particularly on hardness. At lower pressures, most of the particles are not deposited but are rebounded from the substrate [40,90]. This results in a shot peening effect which improves particle bonding and increases the hardness of the coatings through a strain hardening effect as observed by Lee et al.[90]. At very high stagnation pressures, erosion of the coating may take place as observed with the WC_{ox}-xNi based coatings where the thickness decreased with increasing deposition pressures. This erosive effect was most likely compounded by the erosive nature of the sharp and angular micro-sized WC powder particles (see *Figure 4.1* in *Chapter 4*).

Standoff distance controls two competing mechanisms that affect particle velocity, namely, particle acceleration-deceleration due to the formed free gas jet and the presence of the bow shock that increases the drag force experienced by the particles [91]. This relationship is depicted in *Figure 5.1*. Pattison et al. [91] demonstrated that the occurrence of bow shock reduced both the velocity of the carrier gas and the entrained particles. At low standoff distances, the effect of the bow shock was more pronounced resulting in decreased particle velocities and deposition efficiencies. At higher standoff distances, the presence of the bow

shock disappeared, however, the gas velocity had fallen below the particle velocity resulting in particle deceleration [91]. This relationship was observed for the deposition of the oxide reduced WC_{ox}-Ni and the agglomerated and sintered WC_{12Co}-Ni and WC_{10Ni}-Ni powders in which a higher SOD setting of 15 mm instead of 10 mm was ideal. Overall, the careful control of the deposition parameters used in CGDS is required to achieve the desired deposition efficiencies and coating properties.

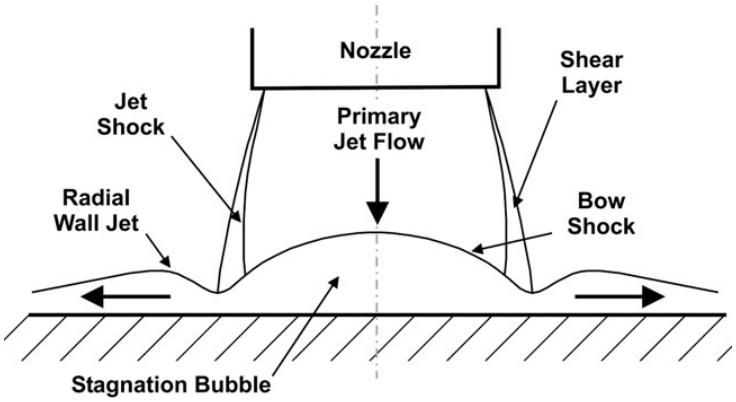

Figure 5.1: Schematic diagram of the supersonic impingement zone with the occurrence of bow shock at the substrate [91].

5.2. Influence of the feedstock powders on the coating deposition and properties.

Differences in the morphologies of the feedstock powders are known to influence the deposition behaviour and resultant properties of the coatings [16,21,44]. The oxide reduced WC_{ox} powder was composed of two different morphologies, namely angular and spherical particles. Spherical particles are more ideal for transportation within a moving gas stream compared to angular ones as their shape minimises the inflight resistance encountered by the powders, giving rise to more superior powder flowability [92-93]. Angular particles generally have poor aerodynamic properties which inherently affect the flowability of particles within a gas stream [92-93]. Even though the angular particles were within the size range recommended for cold spraying (−45 + 5 μm), some particles may have been scattered to the periphery of the carrier gas stream during deposition. The angular particles that did reach the substrate may have eroded the coating due to the impact of the sharp facets during deposition [40,44]. However, the highly dense nature of carbide particles increased the impact energy of the particles which was beneficial for the adiabatic shearing and adhesion of the Ni binder and

resulted in less porous coatings [17-18,20,38-39]. It is therefore hypothesised by the author that two competing mechanisms, namely coating build-up and erosion, may have taken place during deposition. The porous, spherical and agglomerated nano-structured WC_{12Co} and WC_{10Ni} particles were most likely able to achieve higher particle velocities during flight compared to the WC_{ox} particles. This powder type has good aerodynamic properties which maximises the number of particles that reach the substrate for deposition. The morphology of this powder type was also advantageous as the manner in which the particles deformed during deposition assisted with the high carbide retention. However, its highly porous nature resulted in coatings with lower hardness values.

The milling process resulted in the smearing of the Ni powder onto the WC particles as observed in *Figure 5.2*, which may have been beneficial for the coating deposition and adhesion properties of the powders. In the study conducted by Wang et al. [21], the deposition efficiencies of WC-Al and WC-Cu powder blends produced by mechanical mixing, and WC particles coated with Al and Cu using a chemical vapour deposition (CVD) process were compared. It was found that the metal coated WC feedstock powders retained higher percentages of the WC phase in the resultant coatings compared to their mechanically blended counterpart powders. The addition of a ductile metal layer around the hard, brittle carbide particles appeared to improve the solid-state particle-to-substrate and particle-to-particle bonding, and as a result, the encapsulated hard WC particles behaved like regular soft metal powders during impact [21].

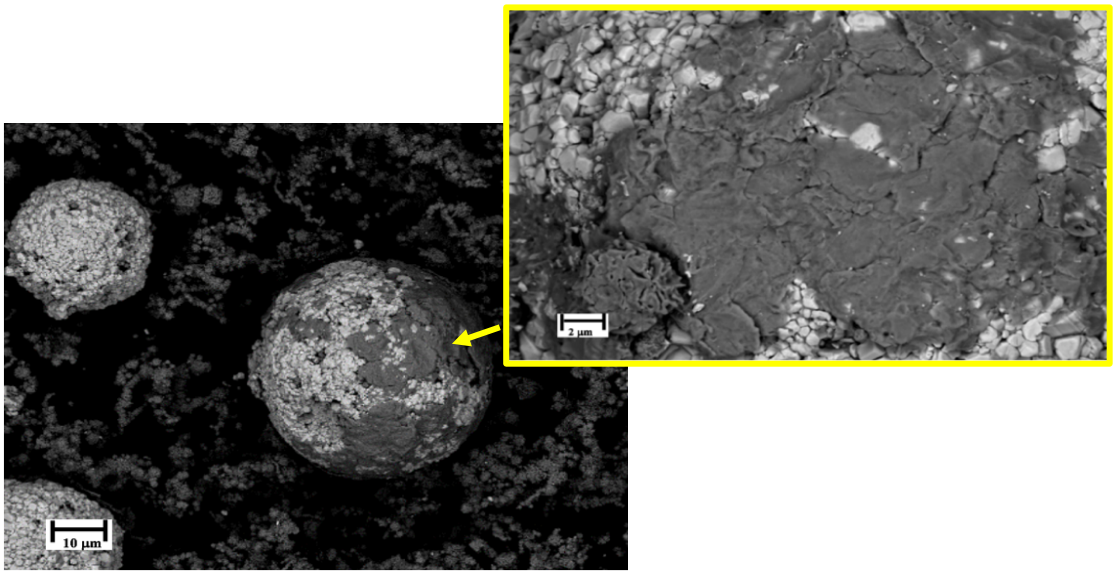

Figure 5.2: Smearing of Ni binder on surface of spherical and agglomerated WC_{12Co} powder as a result of milling process.

The porosity of the starting powders also affected the deposition and porosity properties of the resultant coatings. The WC_{ox}-4Ni powder yielded coatings with the lowest porosity of 1.47% while the WC_{12Co}-50Ni coatings possessed the highest porosity of 5.11%. Overall, higher porosity values were obtained for the spherical and agglomerate WC_{12Co}-xNi and WC_{10Ni}-xNi coatings. Dosta [45] studied the effect of starting powder porosity on the deposition behaviour of WC-25Co using CGDS [45]. *Figure 5.3* illustrates the cross-section of the as-received WC_{ox}, WC_{12Co} and WC_{10Ni} powder particles used in this study. The porosity of the agglomerated and sintered WC_{12Co} and WC_{10Ni} type powders was calculated to be 31% and 34 % respectively, classifying them as high porosity powders. Similarly to the particles examined by Dosta [45], the highly porous WC_{12Co} particles experienced much deformation and particle compaction during deposition as illustrated in *Figure 5.4*. The porous nature of the spherical and agglomerated WC_{12Co} and WC_{10Ni} increased the deformability of the particles, allowing for particle densification and coating build-up. The deposition behaviour of the WC_{ox} particles resembled that of the low porosity WC-25Co agglomerated and sintered powders used by Dosta [45] as the particles displayed limited deformation during impact. However, the impact experienced was sufficient to shatter the WC_{ox} particles during deposition as observed in *Figure 5.5.*

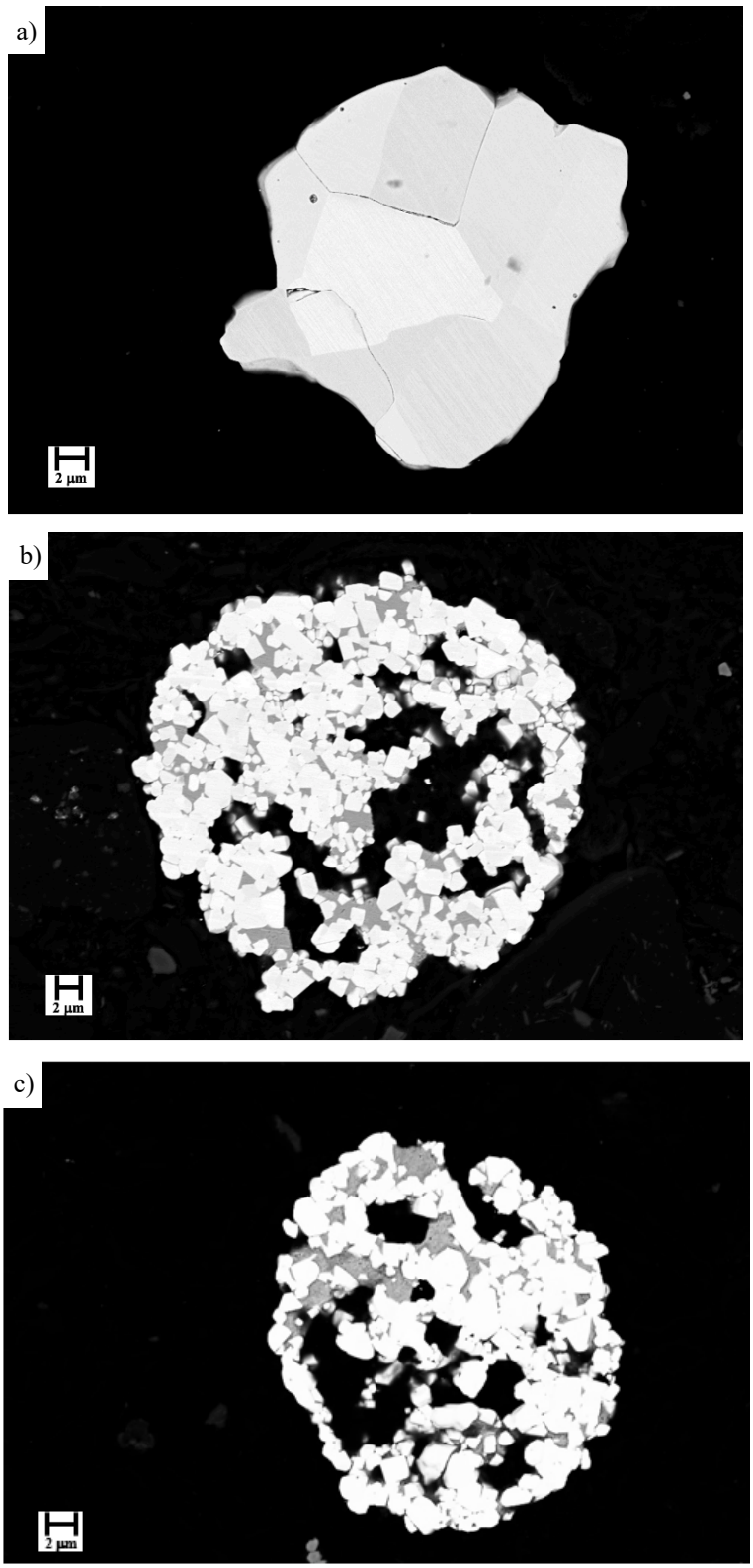

Figure 5.3: Cross sections of the as-received (a) WC_{ox}, (b)WC_{12Co} and WC_{10Ni} powder particles.

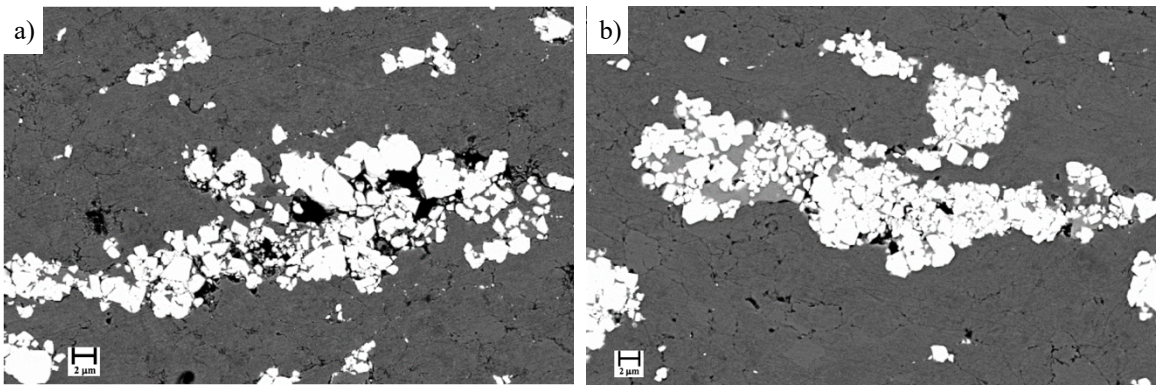

Figure 5.4: SEM micrographs showing elongated and deformed (a) WC_{12Co} and (b)WC_{10Ni} agglomerates within Ni matrix as a result of the high energy impact experienced during deposition.

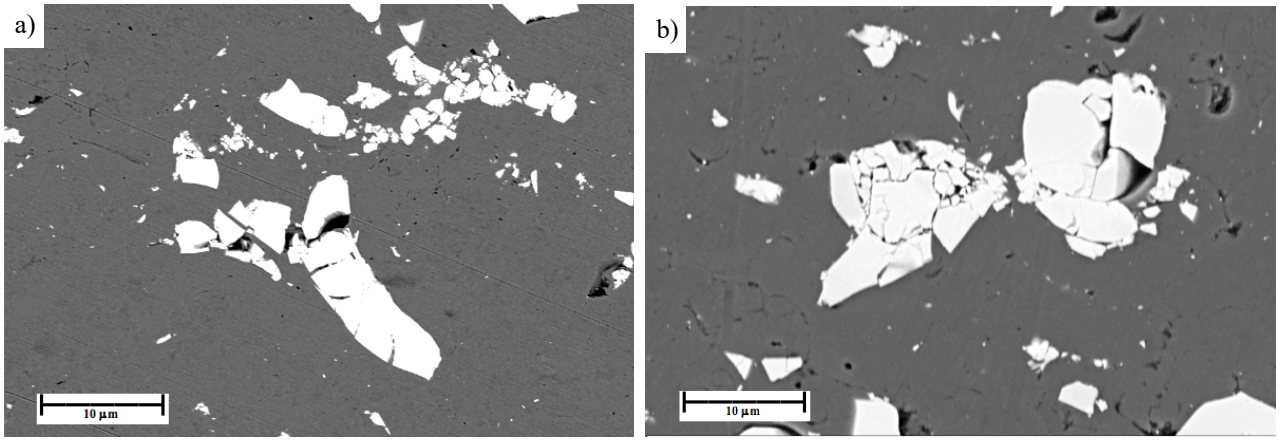

Figure 5.5: SEM micrographs showing fractured WC_{ox} particles within Ni matrix as a result of the high energy impact experienced during deposition.

5.2.1. Microstructure of the cold sprayed coatings

As observed in the XRD patterns of the WC_{ox}-xNi, WC_{12Co}-xNi and WC_{10Ni}-xNi coatings, the chemical composition and bulk properties of the coatings were identical to the parent powders. This indicates that the cold spray conditions applied did not cause any decarburization, oxidation and phase changes typically generated in HVOF coatings [4-5,7-9,13]. Ang et al. [35] observed the occurrence of grain refinement in which higher deposition pressures in the range of 1200-1503 kPa (174-218 psi) were used, and concluded that this was due to the grain refinement and severe plastic deformation experienced during particle impact [35]. In the current work, the occurrence of possible grain refinement was not identified in the XRD

patterns and could not be further investigated due to a limitation in the additional samples required for Rietveld refinement studies.

A high standard deviation in the coating hardness values was observed across all the coatings, which was also prevalent in the WC-Ni based coatings produced by Melendez et al [43] using a similar low pressure CGDS system. It was also noted that the hardness values obtained for the WC_{12Co}-4Ni coatings were slightly lower than those obtained by Melendez et al [43], even though the chemical composition of the powders were identical. Melendez made use of a sintered and crushed WC-12Co powder, depicted in *Figure 5.6*, which appeared denser than the spherical and agglomerated WC_{12Co} powder used in the current study. In addition, the morphology of the sintered and crushed WC-12Co powder used by Melendez was more similar to the oxide reduced WC_{ox} powder which gave rise to superior coating hardness due to the dense nature of both carbide powders. Overall, cold sprayed WC-Ni MMC coatings are expected to have a large variation in the coating hardness values due to the dispersion of the hard carbide particles within the soft Ni binder [43].

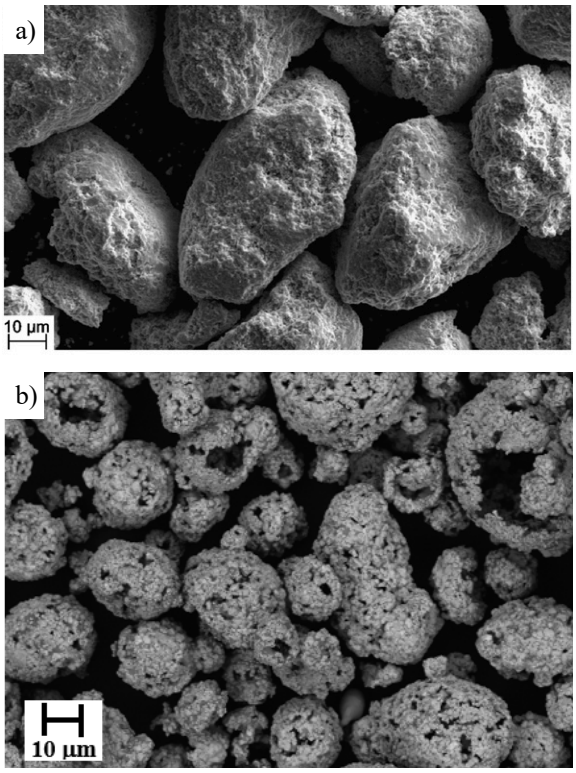

Figure 5.6: (a)Sintered and crushed powders WC-12 wt.% Co used by Melendez et al. [43] and (b) The WC_{12Co} powders used in the current study to develop the WC-Ni based MMC coatings.

According to literature, the most critical material property determining erosion resistance is fracture toughness (K_{1c}) [49]. In the current investigation, the fracture toughness of the WC-Ni based coatings could not be determined. The palmqivist cracks formed from the Vickers indentations, which are required for the K_{1c} calculation, were not formed as seen in *Figure 5.7*, therefore this property could not be determined. Since coating hardness is also one of the critical factors considered for erosion [49], the powder combination that produced the hardest coatings was selected as the optimal composition to undergo erosion testing. The oxide reduced WC_{ox}-4Ni coating composition (464 ± 15 HV) was selected to undergo slurry erosion and corrosion testing as it possessed the highest hardness of the all the coatings.

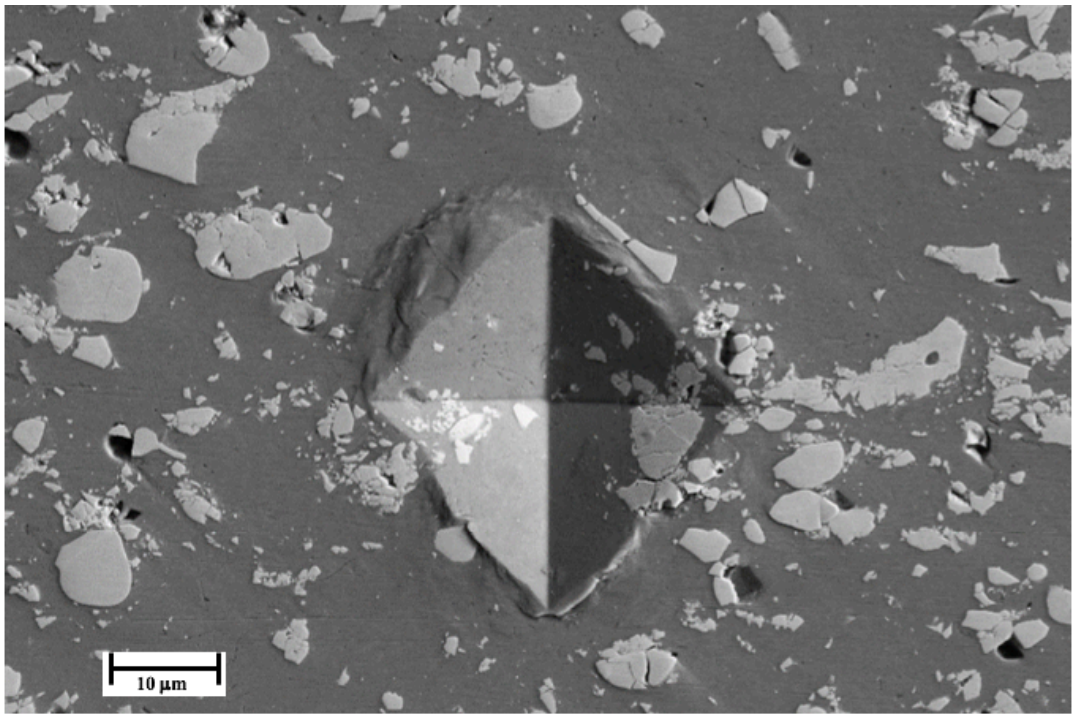

Figure 5.7: SEM micrograph of Vickers hardness indent in WC_{ox}-Ni MMC coating illustrating the occurrence of plastic deformation and no Palmqvist cracking required for fracture toughness measurements.

5.3. Influence of TiC and Mo additions to the WC-4Ni wt. % coating

The addition of 1 wt% Mo (1530 HV [84]) and 10 wt% TiC (3200 HV [85]) to the optimal WC_{ox} - 4Ni composition further increased the hardness of the coatings as summarized in *Table 4.4* in *Section 4.4*. Good coating build-up was also observed across three of the four coatings, with the exception of the WC_{ox}-4Ni-1Mo coating, which showed poor deposition properties

and coating delamination. This combination was eliminated from further erosion and corrosion testing. The subsequent slurry erosion tests indicate that two distinct modes of wear took place on the WC_{ox} -Ni MMC coatings, namely, erosion by plastic deformation and brittle fracture as seen in the SEM micrographs of the eroded surfaces in *Figures 5.8* and *5.9*.

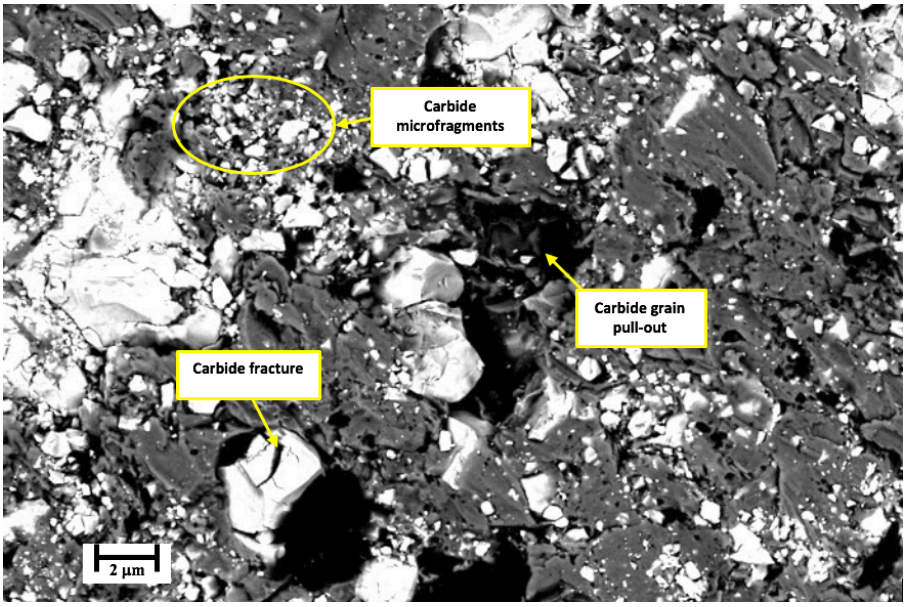

Figure 5.8: Backscatter electron SEM micrographs of an eroded WC_{ox}-4Ni based coating demonstrating erosive wear by brittle fracture.

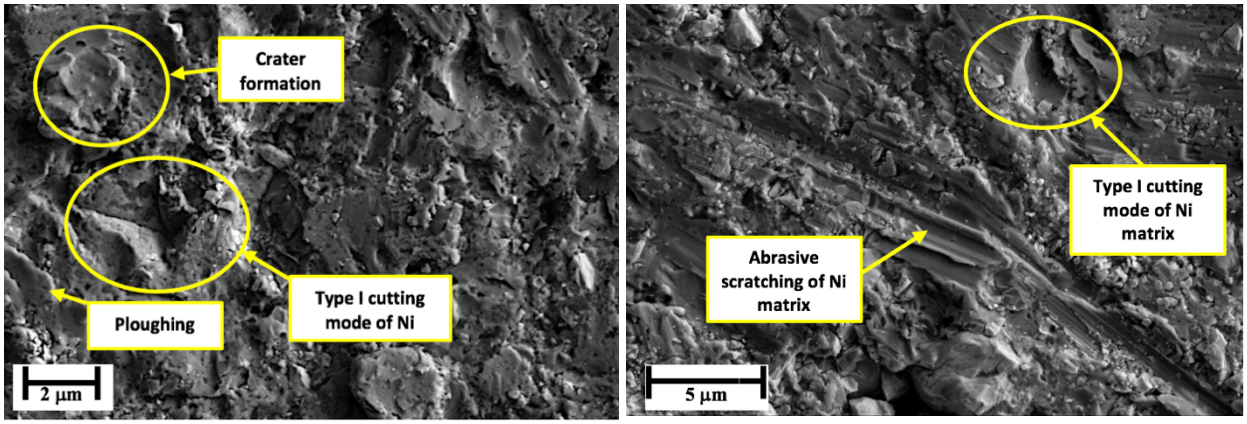

Figure 5.9: Secondary electron SEM micrographs of an eroded WC_{ox} -4Ni based coating with indentation, scratching and crater formation, characteristic of erosive and abrasive wear by plastic deformation.

Erosion by brittle fracture is characterized by the occurrence of particle fracture and the detachment of material in the form of wear debris [49]. Several forces act on the erodent particle upon impact with the surface as depicted in *Figure 5.10* [49]. The normal force is the

most dominant as it is responsible for the retardation of the in-flight particle. When the applied normal load reaches a critical value, which is dependent on the toughness of a material, the formation of lateral cracks occurs within the hard, brittle carbide grains. The intersection of several lateral cracks causes severe particle fragmentation which then leads to the formation of WC micro-fragments and grain pullout from the Ni matrix as observed in *Figure 5.8* [49].

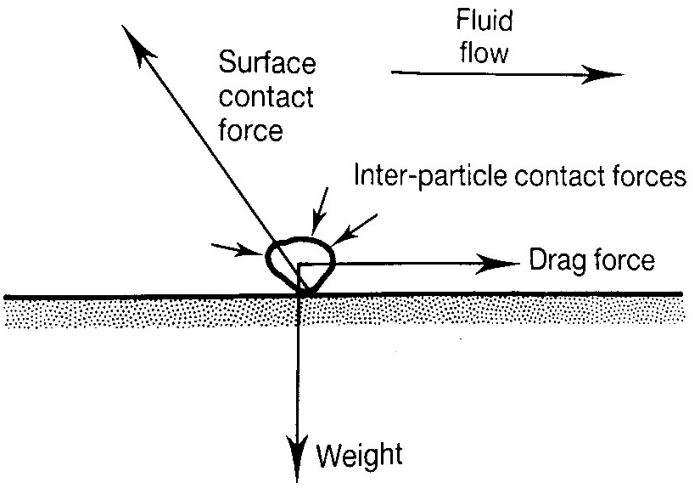

Figure 5.10: Diagram showing forces which act on a particle in contact with a solid surface [49].

Ploughing and cutting within the ductile Ni binder was also observed across all three coating compositions which is characteristic of erosion by plastic deformation. The Type I mode of cutting was observed, as seen in *Figure 5.9,* which occurs when the erodent particle strikes the surface, rolls forward and causes a raised indent in the material. The ploughing mode is mainly caused by rounded particles that displace the material to the side and front of the erodent particle, forming a crater [49].

Several factors affect the extent and nature of the wear mechanism of materials, these include, but are not limited to the shape, hardness and size of the erodent particles, the properties of the counter surface, the impact angle and the slurry medium properties [49]. The SiC particles (*Figure 5.11*) used to erode the cold spray particles consisted of a sharp morphology which led to the formation of deep, distinct indents within ductile materials as labelled in *Figure 5.9*. Angular particles cause more erosive damage than spherical ones, particularly at an impact angle of 90° [49]. The hardness of the erodent also plays a dominant role in the erosion rate of the surface. According to the slip-line theory for non-spherical particles, erodents of any shape

will cause scratching only if the hardness of the abrasive (H_a) and surface(H_s) is $H_a/H_s>1.2$ [49]. An H_a/H_s value of 13 and 1,083 (see *Equations 5.2* and *5.3*) for the respective SiC- Ni and SiC-WC combinations confirmed that the silica erodent is able to plastically deform the Ni matrix but not the WC grains. It should also be noted that some of the erodent particles became embedded in the matrix as illustrated in *Figure 5.12*. This occurrence may have altered the accuracy of the weight readings for the total mass loss vs time graph in *Figure 4.33* of the *Results* chapter.

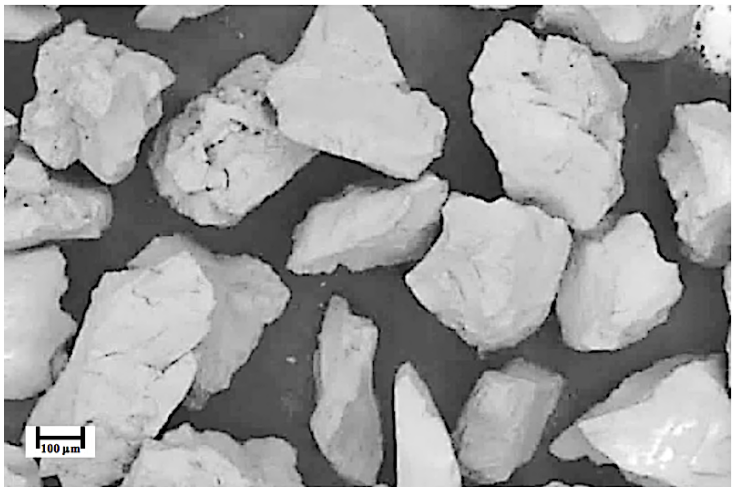

Figure 5.11: SEM micrograph of SiC erodent particles.

$$\frac{Ha_{SiC}}{Hs_{Ni}} = \frac{2600\ HV}{200\ HV} = \boldsymbol{13} \qquad \text{Equation 5.2}$$

$$\frac{Ha_{SiC}}{Hs_{WC}} = \frac{2600\ HV}{2400\ HV} = \mathbf{1{,}083} \qquad \text{Equation 5.3}$$

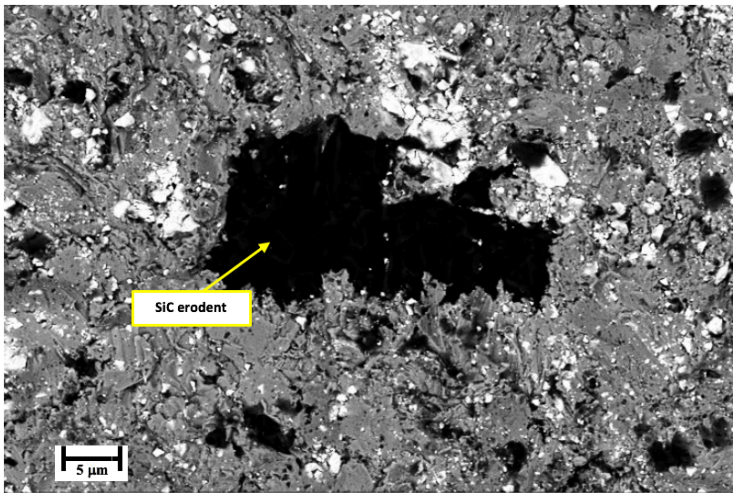

Figure 5.12: SiC particle embedded within softer Ni matrix of WC-4Ni based coating.

Even though the hardness values of SiC (2600 HV [94]) and WC (2400 HV [3]) were comparable, the successive impact of the erodent was able to shatter the WC particles as seen in *Figure 5.7*. The impact of hard SiC particles on the brittle WC particles induced particle fracture and the propagation of cracks which led to material removal from the surface. It is hypothesized by the author that the extent of WC particle fracture may have been amplified by the residual stresses induced during the cold spraying process, lowering the materials resistance to impact and causing premature fracture during erosion testing.

The eroded surfaces also possessed long wear paths which is indicative that a two-body abrasive wear mechanism took place. Abrasive wear is distinct from erosion in that it is caused by the sliding action of a hard particle on a surface [49]. Upon impact on the coating surface, the flow of the slurry medium leads to the lateral movement of the SiC erodents which then causes scratching within the Ni matrix as highlighted in *Figure 5.9*. Since the hardness values of WC (2400 HV [3]) and SiC (2600 HV [94]) were similar, the abrasive action of the erodent on the WC grains did not lead to the formation of distinct wear paths however may have further contributed to cracking and fragmentation of the grains [49].

The homogeneity of the WC_{ox}-Ni coatings was also essential for wear resistance. For erodent indentations significantly larger than the WC grain size and binder mean free path, the material will behave like a homogenous solid and the erosion of both the carbide and binder will occur as depicted in *Figure 5.13* [49]. However, for cemented carbides with a long binder mean free path such as the one observed for the WC-Ni based coatings under study, the materials behave heterogeneously, giving rise to the two distinct wear mechanisms as previously discussed.

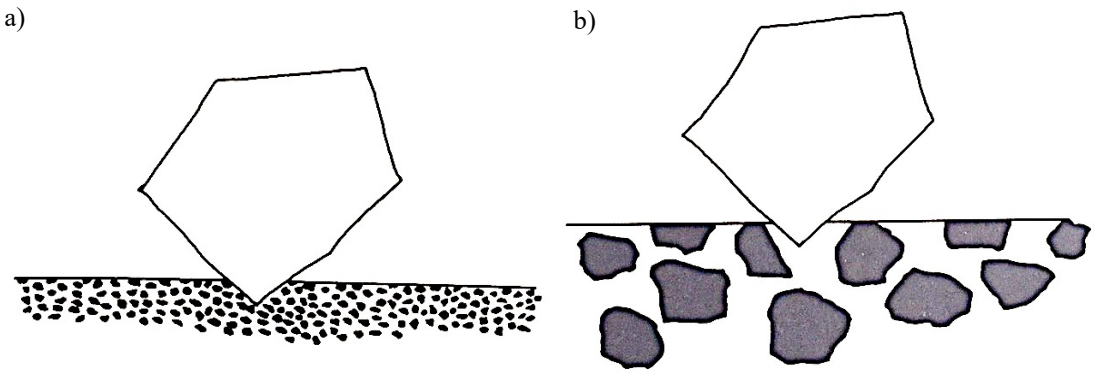

Figure 5.13: Illustration of the importance of relative sizes of the particle contact zone and the hard phase regions in the abrasive wear of a two-phase material. In (a) the material responds heterogeneously, whereas in (b) the material responds heterogeneously [49].

All the coatings demonstrated good slurry erosion resistance at an impact angle of 90°. Even though extensive fracture of the WC grains was observed, the overall mass loss experienced by the coatings throughout the erosion tests was low. Ductile materials are most resistant to erosive wear at high impact angles as they possess the ability to experience plastic deformation, energy absorption and strain hardening before material failure [49]. At lower impact angles the shear stresses encountered by the surface are maximized, leading to high amounts of plastic deformation and material damage. Brittle materials on the other hand have a limited ability to deform and absorb energy before fracture [49]. A normal incident angle maximises the extent of particle fracture and grain pullout, therefore. The relationships between the impact angle and erosion rate, and the stress and strain curves of ductile and brittle materials are summarised in *Figures 5.14 a* and *b* respectively.

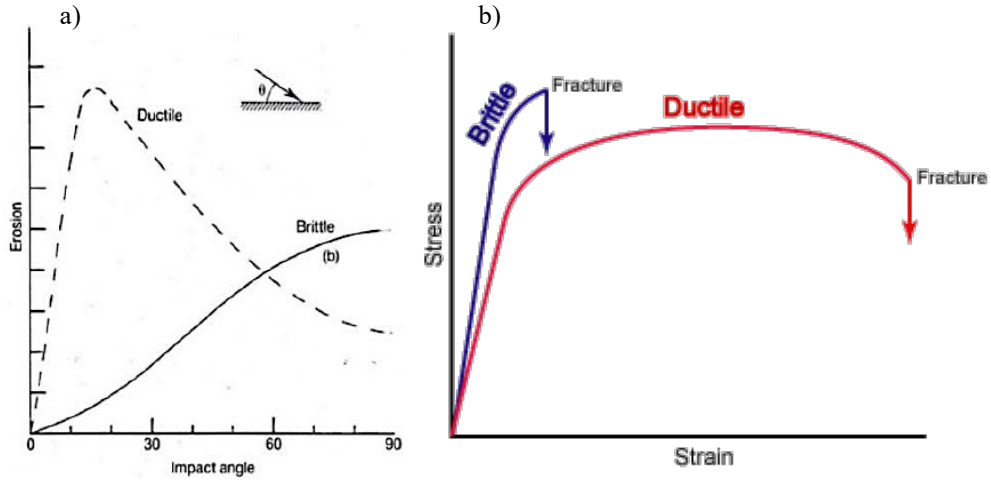

Figure 5.14: a) The effect of impact angle on the erosion rate [49], and (b) the stress and strain curves for ductile and brittle materials [95].

Further studies on the response of the WC_{ox}-Ni based coatings at lower impact angles could not be conducted due to a limitation in the number of samples. Most of the as-received carbide powder was used during the parameter optimization study. Additional oxide reduced WC_{ox} powder was purchased from Flomaster, however, its morphology differed significantly from the original powder as depicted in *Figure 5.15*. None of the sharp and angular particles, present in the original carbide powder, could be observed in the SEM micrographs of the new oxide reduced WC_{ox} powder. The average particle size of the latter powder was also much larger even though a powder with identical specifications had been requested from the manufacturer. This deviation in powder morphology would have affected the deposition and material

properties of the resultant coatings, hence additional WC_{ox}-4Ni coatings could not be developed. Extensions to the current work will be included in the *Recommendations for Future Work* section.

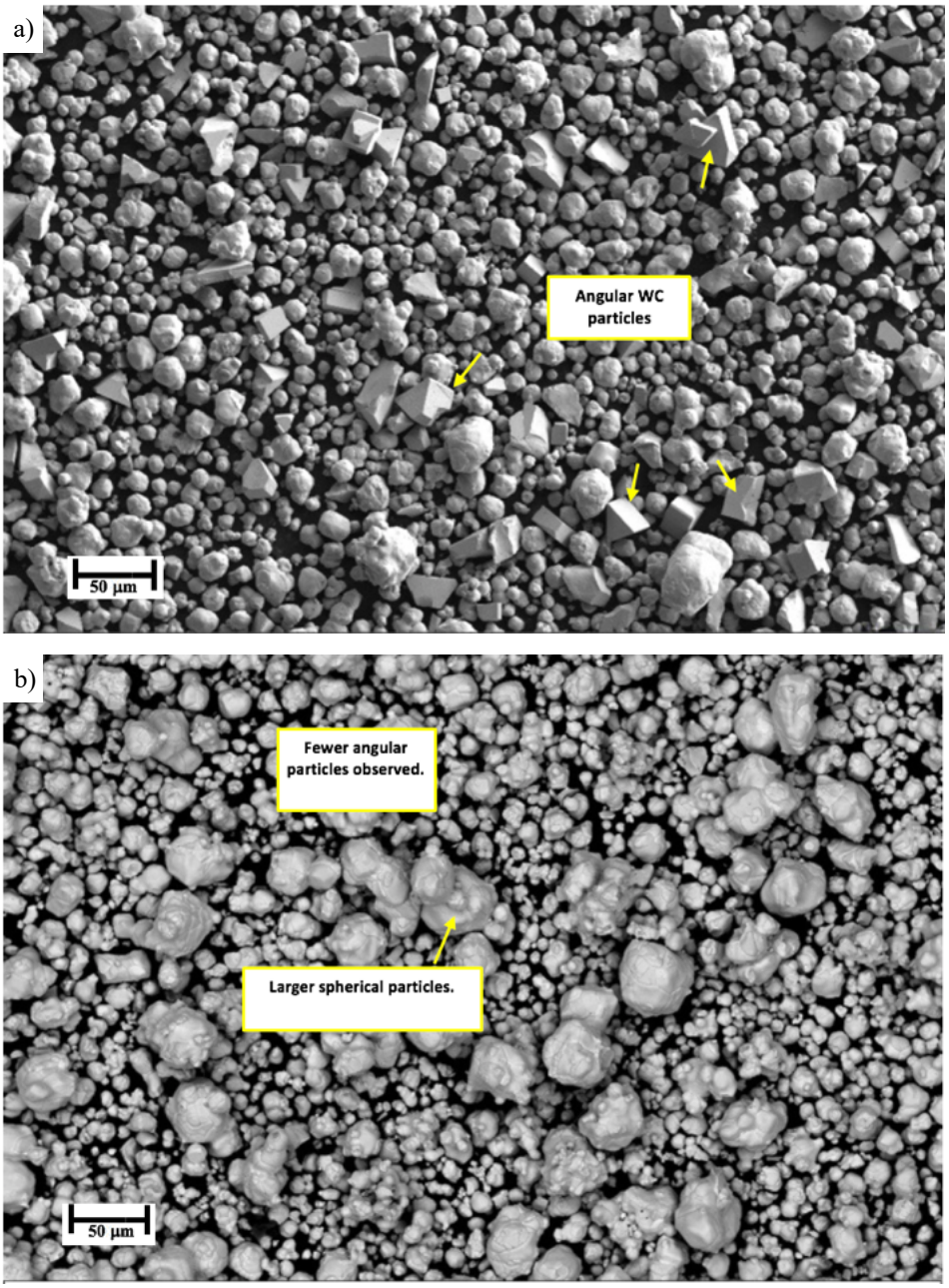

Figure 5.15: SEM micrographs of the (a) initial and new (b) oxide reduced WC_{ox} powder.

Similarities between the cold spray process and the erosion tests conducted on the WC-Ni based coatings can be drawn as both processes involve the impact of hard, high-speed particles onto a ductile metallic surface. Cold spraying and erosion with SiC erodents at an impact angle

of 90° caused the severe strain hardening of the Ni matrix. Strain hardening is the strengthening of a ductile metal by the introduction of residual stresses and plastic deformation [88]. The impact energy from the in-flight carbide particles is absorbed by the ductile metal matrix which induces residual stresses and the formation of dislocations within the material. The accumulation of dislocations leads to the resistance of further plastic deformation and consequently increase the strength of the metal [81]. A harder Ni matrix would subsequently lead to a decrease in toughness and the ability to absorb the impact energy of the particles, resulting in a more brittle form of erosion. Significant differences in the extent of WC_{ox} damage before and after erosion testing can be observed in *Figure 5.16*, indicating that the SiC erodents induced further strain with the coatings. Future work would include conducting stress-strain analysis on the cold spray coatings before and after the erosion tests. This comparison will provide insight into the effect that the particle impact had on the surfaces.

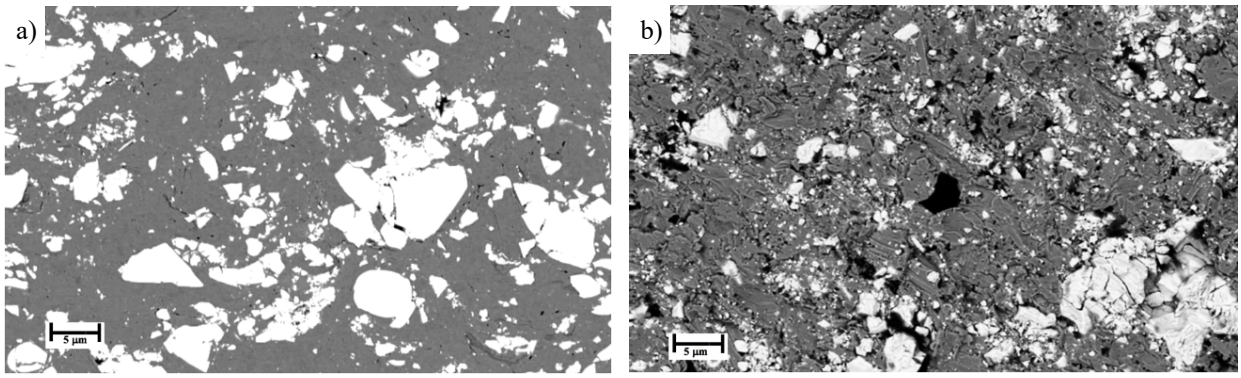

Figure 5.16: SEM micrograph of WC_{ox}-4Ni coating illustrating extent of carbide fracture (a) before and (b) after erosion.

Previous studies have indicated that cold spray coatings outperform the wear properties of WC-based coatings produced by high-temperature processes, mainly due to the presence of these residual compressive stresses. Melendez et al. [56] studied the dry abrasion wear of WC-12 wt% Co-Ni coatings deposited using a low pressure CGDS system and compared the erosion properties with the ones produced by HVOF spraying. From the study, it was found that as the hardness and the percentage of WC retained within the cold sprayed coating increased, the wear rate consequently decreased. The relationship between hardness and wear rate for the coatings was relatively linear, suggesting that hardness contributed significantly to the abrasive wear resistance [56]. Although hardness is typically used as a first-order approximation of wear rate for WC-based materials, carbide grain size and binder content have been shown to have

an effect on the wear resistance [57]. Melendez et al. [56] then compared the wear rates of the cold sprayed coating with the highest retained WC content of 66 wt% to HVOF sprayed WC-Co coatings with 83 wt% retained WC [56]. Once again, the same trend observed; the CGDS coatings had better wear resistances compared to the HVOF coatings, despite the higher hardness of the HVOF coatings (1100 HV compared to 533 HV). This trend was attributed to the negative impact of WC decarburization as a result of the high temperature process [56]. The ductility and toughness of the Ni matrix of the cold sprayed carbide coating also contributed to the improved wear resistance. The WC particles reinforced the coating, minimizing the damage to the surface of the coatings. The binder mean free path, which dictates the distance between the reinforcing WC particles within the metallic matrix, may be used to describe the mechanical properties of WC-based coatings. Melendez et al. [56] used the Ni mean free path to explain the changes in the wear rate of the WC-Co-Ni coatings. The authors found that the wear rate of the coatings decreased significantly as the mean free path between the WC-based reinforcing particles decreased. The main wear mechanism observed was plastic deformation of the soft Ni matrix, while the hard WC particles appeared to remain undamaged [56].

The erosion performance of the cold sprayed WC_{ox}-Ni based coatings produced in this study was also compared to the HVOF sprayed WC-Co coatings developed by Ogunmuyiwa [96] who conducted slurry erosion tests on the coatings under identical conditions. The microstructure of the WC-Co alloys produced by Ogunmuyiwa. [96] is presented in *Figure 5.17* [96]. The cold spray coatings experienced lower erosion rates at an impact angle of 90° compared to the HVOF sprayed WC-Co coatings as summarized in *Figure 5.18*. The superior erosion resistance of the cold sprayed coatings can be attributed to the presence of the ductile Ni binder which is able to absorb the impact energy of the erodents, deform plastically, and strain harden during erosion. The presence of ditungsten carbide (W_2C) was also detected in the HVOF sprayed WC-17Co-10VC coatings which is known to decrease the wear resistance of WC-Co coatings. However, these coatings had a higher wear resistance compared to the WC-12Co coatings which can be attributed to the higher binder content within the coatings.

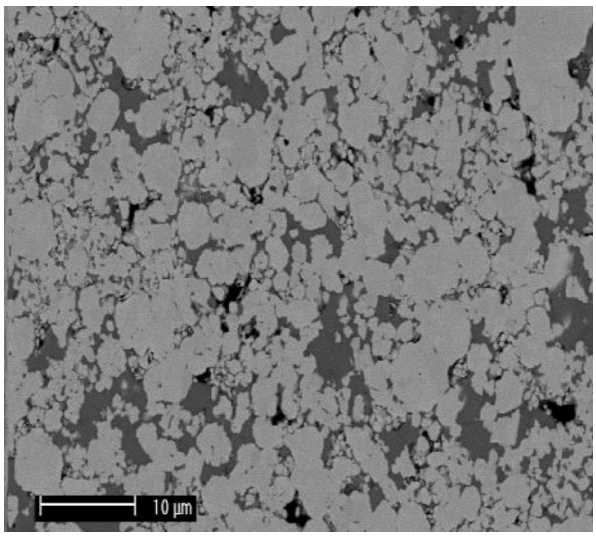

Figure 5.17: SEM micrograph of the HVOF sprayed WC-Co alloys produced by Ogunmuyiwa [96].

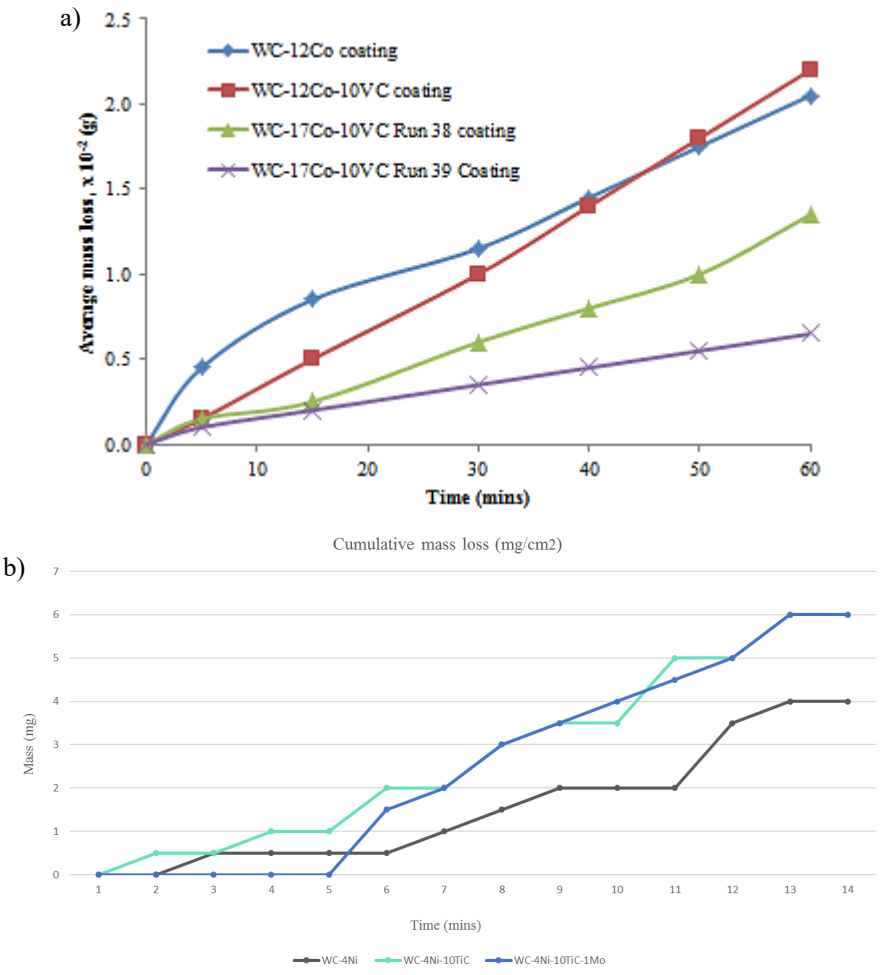

Figure 5.18: Cumulative mass loss of (a) HVOF sprayed WC-17Co-10VC coatings [96], and (b) cold sprayed WCox-4Ni based coatings.

5.3.1. Alloying effect

Previous studies indicate that alloying results in a negligible effect on the overall erosion rate of materials within the same alloy system [49]. This phenomenon was also observed with the WC_{ox}-Ni based coatings under investigation. The addition of 1 wt. % Mo to the WC_{ox}-4Ni -10TiC did not affect the total mass loss of the cold sprayed coatings. However, Mo did increase the wear resistance of break-in period of the WC_{ox}-4Ni-1Mo-10TiC coatings as this composition experienced no mass loss for the first 30 mins of the test in contrast to the other two compositions. The occurrence of this phenomenon is unknown and would require further investigation in future studies.

5.4. Corrosion properties of cold sprayed WC-Ni based coatings

The addition of Mo and TiC also did not aid the corrosion resistance of the WC_{ox}-4Ni based coatings in tap water as deduced from the OCP and potentiodynamic readings. OCP is an indication of the thermodynamic tendency of a material to participate in an electrochemical reaction with the surrounding medium when no external voltage or current is applied [81]. Metals with a high OCP value are more thermodynamically stable and are, therefore, less likely to undergo corrosion [58-59,62-63]. The WC_{ox}-4Ni coating had the highest OCP values, however, was unstable in the electrolyte. This erratic behavior was not observed in the WC_{ox}-4Ni-10TiC and WC_{ox}-4Ni-1Mo-10TiC coatings, suggesting that the addition of TiC and Mo increased the stability of the coatings within the solution, but did not necessarily improve their corrosion resistance. The WC_{ox}-4Ni-10TiC and WC_{ox} -4Ni-1Mo-10TiC coatings had the lowest E_{corr} and highest i_{corr} values meaning that they were the most chemically active in tap water, further substantiating the more superior corrosion resistance of the WC_{ox}-4Ni composition.

The composition of the metallic binder is usually the main determinant for the corrosion resistance of cemented carbides [1,25-26]. Metals are more susceptible to corrosion compared to most materials due to their tendency to donate surface electrons in an attempt to lower their energy state and be in a more thermodynamically stable state with their environment [58-59]. Nickel and its alloys have exceptional corrosion properties and are mainly used for protection against corrosion in aqueous solutions [1, 24]. Nickel possess superior corrosion resistance in distilled and fresh water; the typical corrosion rate for pure Ni in a distilled water at 25 ° C is

<0,0025mm/yr [97]. Since the wt. % Ni of the coatings remained constant, the increase in corrosion rates can be attributed to the chemical attack of the Mo and TiC. Molybdenum starts to erode at high humidity levels and when placed in water and is conventionally added to stainless steels for increased corrosion resistance, in particular pitting and crevice corrosion [74]. The metal works by forming a tough surface oxide layer on the steel component, making it harder for chlorides and other pitting agents to penetrate the substrate layer. Additions of 1 or 2 wt. % are usually added for a pronounced effect on the corrosion resistance in alkaline and oxidizing liquids [74]. At an atmospheric humidity of under 60 %, Mo is corrosion-resistant, however, discoloration of the metals starts to occur at higher humidity levels, explaining its poorer resistance in tap water. The general corrosion properties of Mo are summarized in *Table 5.1*. The addition of Mo also caused a change in the cathodic response of the WC_{ox}-4Ni based coatings as observed in *Figures 4.37 and 4.38* of the *Results* chapter. At an applied voltage of 0.65 V, the cathodic reaction and current density of the WC_{ox}-4Ni-1Mo-10TiC coating increased. It is hypothesized by the author that at this potential, the surface electrons from Mo and the excess electrons from the applied potential caused an increase the cathodic reaction, leading to the reduction of H ions according to *Equation 5.4*.

$$\mathbf{2H^+ + 2e^- \rightarrow \boldsymbol{H^2}} \qquad \text{Equation 5.4}$$

Table 5.1: Corrosion resistance of molybdenum [74].

Water	Cold and warm water < 80 °C (353 K)	resistant
	Hot water > 80 °C (353 K)	not resistant
	Hot water with nitrogen gassing or inhibitor	resistant
Inorganic acids	Hydrofluoric acid < 100 °C (373 K)	resistant
	Nitrohydrochloric acid, cold and warm	not resistant
	Nitric acid, cold and warm	not resistant
	Hydrochloric acid, cold and warm	resistant
	Sulfuric acid < 70 % up to 190 °C (463 K)	resistant
	Potassium hydroxide (KOH < 50 %) up to 100 °C (373 K)	resistant
	Potassium hydroxide (KOH > 50 %)	not resistant
Lyes	Sodium hydroxide (NaOH < 50 %) up to 100 °C (373 K)	resistant
	Sodium hydroxide (NaOH > 50 %)	not resistant
	Sodium hypochlorite solution, cold and warm	not resistant
	Oxalic acid 20 °C (293 K)	resistant
	Tartaric acid 20°C (293 K)	resistant
	Boron up to 1 600 °C (1 873 K)	resistant
Organic acids	Carbon up to 1 100 °C (1 373 K)	resistant
	Phosphorous up to 800 °C (1 073 K)	resistant
	Sulfur up to 440 °C (713 K)	resistant
	Silicon up to 600 °C (873 K)	resistant
	Fluorine 20 °C (293 K)	resistant
Non-metals	Chlorine up to 250 °C (523 K)	resistant

Carbides are also known for their chemically resistant nature [3]. Previous studies have indicated that the corrosion properties of cemented carbides can further be improved by the addition of refractory metal carbides such as TiC, TaC, VC and Mo_2C, which was the reason for the addition of TiC [25-29]. Lin et al. [98] demonstrated that TiC additions to WC-10wt.% Co were able to increase the corrosion resistance of the cemented carbides submerged in a 1 molar (M) NaOH solution. TiC also performed exceptionally in highly acidic mediums such as 1 M HCl [98]. In the current study, the 10 wt. % TiC additions to the cold sprayed WC_{ox}-4Ni coatings led to a decrease in corrosion resistance. Limited studies comparing the corrosion behavior of Ni and TiC in water are available in literature. However, the addition of TiC to the WC_{ox}-4Ni composition decreased the corrosion resistance of the coatings. It is hypothesized by the author that Ni exhibits more superior corrosion properties in water than TiC, hence the

decrease in corrosion resistance when the latter compound was added to the MMC. When cemented carbides corrode in harsh environments, the binder material is usually attacked first which then leads to WC grain pullout [1,99]. This behavior was not observed for any of the coatings under study, however, significant contamination can be observed on the surface of the coatings. Tap water is composed of several organic and inorganic compounds [100] which remained on the surface of the coatings as contaminants upon evaporation as seen in *Figures 4.40-4.41* of *Chapter 4.*

In general, previous studies have shown that CGDS produced more corrosion resistant WC-Co coatings compared to those fabricated using high temperature HVOF techniques. Dosta et al. [45] demonstrated that WC-25Co coatings deposited using a high-pressure cold gas dynamic system were more corrosion resistant in a 3.5% NaCl solution than WC-12Co coatings produced using HVOF deposition. The high-temperature process led to the formation of oxides which resulted in inferior corrosion resistance when compared to parent material of the same composition. The superior chemical resistance of the cold sprayed coatings was attributed to the formation of homogenous, oxide-free, low porosity coatings without cracks or delamination that prevented the electrolyte from attacking the Co matrix interface and the substrate.

6. Conclusion

The findings presented in the current study demonstrate that low-pressure CGDS can be used to deposit WC based coatings, provided that suitable ductile metal binders and deposition parameters are selected to facilitate adhesion.

The use of the Taguchi design of experiments method proved to be an efficient tool for systematically determining the optimal spray parameters for each of the 11 WC-Ni based coatings used in this study. The technique assisted in gaining a better understanding of the relationships between the various deposition parameters and the resultant coating properties while minimizing the number of experiments that had to be conducted. However, the technique did have its shortcomings as it works best for static systems where the measured response variables do not vary significantly or change with time.

Nickel served as an appropriate binder as it was able to successfully co-deposit the oxide reduced WC_{ox}, and the spherical and agglomerated WC_{12Co} and WC_{10Ni} powders even at percentages as low as 4 wt%. The WC_{ox}-4Ni coatings possessed the maximum hardness of 464 ± 15 $HV_{0.3}$ and lowest porosity of 1.47% and were subsequently selected to undergo erosion and corrosion testing. It was found that alloying with 10 wt% TiC (3200 HV [85]) and 1 wt% Mo (1530 HV [84]) improved the average hardness of the WC_{ox}-4Ni coatings, however at the expense of the erosion resistance. Hard and brittle coatings are less resistant to erosion at an impact angle of 90°, hence the higher rates of material degradation observed for the WC_{ox}-4Ni-10TiC and WC_{ox}-4Ni-1Mo-10TiC coatings. Two distinct modes of wear took place on the tested coatings, namely, erosion by plastic deformation and brittle fracture. Ploughing and cutting within the ductile Ni binder was observed across all three coating compositions which was indicative of erosion by plastic deformation. Extensive particle fracture and the detachment of the carbide material was observed as a result of the impact of the SiC erodent which is characteristic of a brittle mode of erosion. The eroded surfaces also possessed long wear paths which was indicative that a two-body abrasive wear mechanism took place due to the lateral flow of the SiC erodents in the slurry medium.

The slurry erosion performance of the cold sprayed WC_{ox}-Ni coatings was also compared to WC-Co coatings produced by HVOF techniques. It was found that the latter coatings experienced lower erosion rates at an impact angle of 90°. This can be attributed to the presence

of the ductile Ni binder which was able to absorb the impact energy of the erodents. XRD analysis of the cold sprayed WC-Ni based coatings indicated that no detrimental phases, such as W_2C, W, and WO_3 typical observed in HVOF coatings, were detected further contributing to increased wear resistance. These findings indicate that low-pressure systems can potentially be used as an alternative for slurry erosion resistance for applications with an impact angle of 90°.

The addition of Mo and TiC also did not aid the corrosion resistance of the WC_{ox}-4Ni based coatings in tap water. The WC_{ox}-4Ni-10TiC and WC_{ox}-4Ni-1Mo-10TiC coatings were the most chemically active in tap water compared to the WC_{ox}-4Ni composition. Nickel possesses superior corrosion resistance in distilled and fresh water [97]. Since the wt% Ni of the WC_{ox}-4Ni, WC_{ox}-4Ni-10TiC and WC_{ox}-4Ni-1Mo-10TiC remained constant, the increase in corrosion rates can be attributed to the chemical attack of the Mo, which starts to erode at high humidity levels and when placed in water.

7. Recommendations

Further research and development on the application of WC-Ni based coatings deposited using low pressure CGDS for industrial slurry erosion environments is still required. In view of the findings presented in this study and for the future expansion of the work which was conducted, the following is recommended:

7.1. Parameter optimization

- Use an iterative method of the Taguchi mixed level DoE technique until convergence between the predicted and experimental values is obtained, thereby improving the robustness of the technique as recommended by Whitcomb et al [86].
- Ensure the repeatability of the measured response variables (i.e coating harness and thickness) when deposited under identical conditions. This will reduce the variability between the predicted and experimental values.

7.2. Cold spray deposition

- Make use of an external powder feeder fitted with a flow meter instead of the non-pressurized vibratory powder feeder for the controlled injection of the powders into the cold spray system. An inconsistent mass flow rate had an impact on the deposition and properties of the resultant coatings which also affected the SNR calculations and the accuracy of the Taguchi DOE method.
- Investigate the use of He or N_2 as an alternative carrier gas as these gases will allow higher particle velocities to be achieved without the use of a more powerful gas compressor. Higher impact velocities will also enable the use of less ductile metals like Co as alternative binder metals for low-pressure systems.

7.3. WC-Ni coating properties

- Make use of oxide-reduce type powders without the sharp and angular particles as these tend to erode the coating and substrate during deposition. Less angular particles will

also improve the aerodynamic properties and increase the deposition efficiency of the powders.

- Investigate the use of metal-coated WC particles as an alternative for increased deposition efficiencies and carbide retention as observed by Wang et al. [21].
- Conduct stress-strain analysis on the cold spray coatings using neutron diffraction stress measurement. This technique will enable the study of the induced compressive stresses within the cold spray coatings, providing more insight into the procedure's deposition mechanism. It will also enable the compressive stresses induced by strain hardening during cold spraying and erosion to be studied in greater detail.

7.4. Erosion and corrosion properties of WC-Ni based coatings

- Investigate the erosion properties of the WC-Ni based coatings at low impact angles, since the coatings were mainly composed of ductile Ni which is most susceptible to erosion at an impact angle of 30°.
- Use mathematical models to determine the mass loss of the MMC coatings since the embedded particles alter the accuracy of the mass loss readings used to calculate the wear rates of the coatings.
- Eliminate the TiC and Mo additions from the WC-Ni based MMC as these did not improve the erosion or corrosion properties of the coatings in tap water at an impact angle of 90°.
- Explore more corrosive environments such as salt water or synthetic mine water where the addition of these alloy systems is more beneficial [24,74,97].
- Study the synergistic erosion-corrosion mechanisms on the rate of coating degradation in further detail.

8. References

1. Davis, J. Applications for Thermal Spray Processing. in *Hand book of thermal spray technology* 169–175 (ASM International, 2004).
2. Davis, J. Introduction to Coatings, Equipment, and Theory. in *Hand book of thermal spray technology* 42–46 (ASM International, 2004).
3. Upadhyaya, G. S. *Cemented tungsten carbides: production, properties, and testing*. (Noyes Publications, 1998).
4. Jacobs, L., Hyland, M. M. & De Bonte, M. Comparative Study of WC-Cermet Coatings Sprayed via the HVOF and the HVAF Process. *Journal of Thermal Spray Technology* **7**, 213–218 (1998).
5. Kear, B. H. *et al.* Thermal Sprayed Nanostructured WC/Co Hardcoatings. *Journal of Thermal Spray Technology* **9**, 399–406 (2000).
6. Kulu, P. & Pihl, T. Selection Criteria for Wear Resistant Powder Coatings Under Extreme Erosive Wear Conditions. *Journal of Thermal Spray Technology* **11**, 517–522 (2002).
7. Qiao, Y., Fischer, T. & Dent, A. The Effects of Fuel Chemistry and Feedstock Powder Structure on the Mechanical and Tribological Properties of HVOF Thermal-sprayed WC–Co Coatings with Very Fine Structures. *Surface and Coatings Technology* **172**, 24–41 (2003).
8. Sahraoui, T., Guessasma, S., Ali Jeridane, M. & Hadji, M. HVOF sprayed WC–Co coatings: Microstructure, mechanical properties and friction moment prediction. *Materials & Design* **31**, 1431–1437 (2010).
9. Watanabe, M., Owada, A., Kuroda, S. & Gotoh, Y. Effect of WC size on interface fracture toughness of WC–Co HVOF sprayed coatings. *Surface and Coatings Technology* **201**, 619–627 (2006).
10. Zikin, A. *et al.* Plasma Transferred ARC (PTA) Hardfacing of Recycled Hardmetal Reinforced Nickel-matrix Surface Composites. *Materials Science* **18**, (2012).
11. Stewart, D. A., Shipway, P. H. & McCartney, D. G. Abrasive wear behaviour of conventional and nanocomposite HVOF-sprayed WC–Co coatings. *Wear* **225**–**229**, 789–798 (1999).
12. Stewart, D., Shipway, P. & McCartney, D. Microstructural evolution in thermally sprayed WC–Co coatings: comparison between nanocomposite and conventional starting powders. *Acta Materialia* **48**, 1593–1604 (2000).

13. Usmani, S., Sampath, S., Houck, D. L. & Lee, D. Effect of Carbide Grain Size on the Sliding and Abrasive Wear Behavior of Thermally Sprayed WC-Co Coatings. *Tribology Transactions* **40**, 470–478 (1997).
14. Padilla, K., Velásquez, A., Berríos, J. A. & Puchi Cabrera, E. S. Fatigue behavior of a 4140 steel coated with a NiMoAl deposit applied by HVOF thermal spray. *Surface and Coatings Technology* **150**, 151–162 (2002).
15. Kim, H.J., Lee, C.H. & Hwang, S.Y. Fabrication of WC–Co coatings by cold spray deposition. *Surface and Coatings Technology* **191**, 335–340 (2005).
16. Lima, R., Karthikeyan, J., Kay, C., Lindemann, J. & Berndt, C. Microstructural characteristics of cold-sprayed nanostructured WC–Co coatings. *Thin Solid Films* **416**, 129–135 (2002).
17. Papyrin, A. *Cold spray technology*. (Elsevier, 2007).
18. Hussain, T., McCartney, D. G., Shipway, P. H. & Zhang, D. Bonding Mechanisms in Cold Spraying: The Contributions of Metallurgical and Mechanical Components. *Journal of Thermal Spray Technology* **18**, 364–379 (2009).
19. Villafuerte, J. Current Trends in Cold Spray Technology: Looking at the Future. *Materials Today* 37–39 (2010).
20. Ning, X.J., Jang, J.H. & Kim, H.J. The effects of powder properties on in-flight particle velocity and deposition process during low pressure cold spray process. *Applied Surface Science* **253**, 7449–7455 (2007).
21. Wang, J. & Villafuerte, J. Low Pressure Cold Spray of Tungsten Carbide Composite Coatings. *Advanced Materials and Processes* 54–56 (2009).
22. Sarin, V. K. Cemented carbide cutting tools (English). *Advances in Powder Technology* 253–288 (1982).
23. Couto, M., Dosta, S. & Guilemany, J. M. Comparison of the mechanical and electrochemical properties of WC-17 and 12Co coatings onto Al7075-T6 obtained by high velocity oxy-fuel and cold gas spraying. *Surface and Coatings Technology* **268**, 180–189 (2015).
24. Sandvik Hard Materials. *Corrosion resistant grades*. (Sandvik Hard Materials, 2008).
25. Tomlinson, W. J. & Ayerst, N. J. Anodic polarization and corrosion of WC-Co hardmetals containing small amounts of Cr3C2 and/or VC. *Journal of Materials Science* **24**, 2348–2352 (1989).

26. Machio, C. N., Konadu, D. S., Potgieter, J. H., Potgieter-Vermaak, S. & Van der Merwe, J. Corrosion of WC-VC-Co Hardmetal in Neutral Chloride Containing Media. *ISRN Corrosion* **2013**, 1–10 (2013).
27. Poblano-Salas, C. A. *et al.* Effects of VC additions on the mechanical properties of bimodal WC–Co HVOF thermal sprayed coatings measured by nanoindentation. *International Journal of Refractory Metals and Hard Materials* **48**, 167–178 (2015).
28. Hashe, N. G., Neethling, J. H., Berndt, P. R., Andrén, H.O. & Norgren, S. A. comparison of the microstructures of WC–VC–TiC–Co and WC–VC–Co cemented carbides. *International Journal of Refractory Metals and Hard Materials* **25**, 207–213 (2007).
29. Bhaumik, S. K., Upadhyaya, G. S. & Vaidya, M. L. Properties and microstructure of WC–TiC–Co and WC–TiC–MO $_2$ C–Co(Ni) cemented carbides. *Materials Science and Technology* **7**, 723–727 (1991).
30. Marple, B. R. & Lima, R. S. Process Temperature/Velocity-Hardness-Wear Relationships for High-Velocity Oxyfuel Sprayed Nanostructured and Conventional Cermet Coatings. *Journal of Thermal Spray Technology* **14**, 67–76 (2005).
31. Thermal Spray Coating Systems & equipment: HVOF-High Velocity Oxygen Fuel. *Flame Spray Technologies.* (2018).
32. Guilemany, J. M., de Paco, J. M., Miguel, J. R. & Nutting, J. Characterization of the W2C phase formed during the high velocity oxygen fuel spraying of a WC + 12 pct Co powder. *Metallurgical and Materials Transactions A* **30**, 1913–1921 (1999).
33. Hussain, T., McCartney, D. G. & Shipway, P. H. Impact phenomena in cold-spraying of titanium onto various ferrous alloys. *Surface and Coatings Technology* **205**, 5021–5027 (2011).
34. Christensen, R. M. *The theory of materials failure*. (Oxford University Press, 2013).
35. Ang, A. S. M., Berndt, C. C. & Cheang, P. Deposition effects of WC particle size on cold sprayed WC–Co coatings. *Surface and Coatings Technology* **205**, 3260–3267 (2011).
36. Bortolussi, V. *et al.* Cold spray of metal-polymer composite coatings onto carbon fiber-reinforced polymer (CFRP). in 7 (TSC 2016 - International Thermal Spray Conference, 2016).
37. Sharma, V. *Convergent-divergent de Laval Nozzle.* (2017).
38. Assadi, H., Gärtner, F., Stoltenhoff, T. & Kreye, H. Bonding mechanism in cold gas spraying. *Acta Materialia* **51**, 4379–4394 (2003).

39. Grujicic, M., Zhao, C., DeRosset, W. & Helfritch, D. Adiabatic shear instability based mechanism for particles/substrate bonding in the cold-gas dynamic-spray process. *Materials & Design* **25**, 681–688 (2004).
40. Schmidt, T., Gärtner, F., Assadi, H. & Kreye, H. Development of a generalized parameter window for cold spray deposition. *Acta Materialia* **54**, 729–742 (2006).
41. Bailyn, M. *A survey of thermodynamics*. (AIP Press, 1994).
42. Rees, D. W. A. *Basic engineering plasticity: an introduction with engineering and manufacturing applications*. (Elsevier, 2006).
43. Melendez, N. M. & McDonald, A. G. Development of WC-based metal matrix composite coatings using low-pressure cold gas dynamic spraying. *Surface and Coatings Technology* **214**, 101–109 (2013).
44. Lioma, D., Sacks, N. & Botef, I. Cold gas dynamic spraying of WC–Ni cemented carbide coatings. *International Journal of Refractory Metals and Hard Materials* **49**, 365–373 (2015).
45. Dosta, S., Couto, M. & Guilemany, J. M. Cold spray deposition of a WC-25Co cermet onto Al7075-T6 and carbon steel substrates. *Acta Materialia* **61**, 643–652 (2013).
46. He, J., Ice, M., Lavernia, E. J. & Dallek, S. Synthesis of nanostructured WC-12 pct Co coating using mechanical milling and high velocity oxygen fuel thermal spraying. *Metallurgical and Materials Transactions A* **31**, 541–553 (2000).
47. Gao, P.H., Li, C.J., Yang, G.J., Li, Y.G. & Li, C.X. Influence of substrate hardness on deposition behavior of single porous WC-12Co particle in cold spraying. *Surface and Coatings Technology* **203**, 384–390 (2008).
48. Nunthavarawong, P., Sacks, N. & Botef, I. Effect of powder feed rate on the mechanical properties of WC-5 wt%Ni coatings deposited using low pressure cold spray. *International Journal of Refractory Metals and Hard Materials* **61**, 230–237 (2016).
49. Hutchings, I. M. *Tribology: friction and wear of engineering materials*. (Butterworth-Heinemann, 2001).
50. Pasaribu, H. Friction and wear of zirconia and alumina ceramics doped with CuO. (s.n.], 2005).
51. *Springer handbook of materials measurement methods*. (Springer, 2006).
52. Bagci, M., Imrek, H. & Aktas, A. Solid particle erosion behaviour of glass mat-based polyester laminate composite materials. *Journal of Thermoplastic Composite Materials* **26**, 777–794 (2013).

53. Liu, H. Y., Kou, S. Q. & Lindqvist, P. A. Numerical Studies on Bit-Rock Fragmentation Mechanisms. *International Journal of Geomechanics* **8**, 45–67 (2008).
54. Hutchings, I. M. Mechanisms of wear in powder technology: A review. *Powder Technology* **76**, 3–13 (1993).
55. Unknown. *Substances & Technologies. Adhesive wear.* (2018).
56. Melendez, N. M., Narulkar, V. V., Fisher, G. A. & McDonald, A. G. Effect of reinforcing particles on the wear rate of low-pressure cold-sprayed WC-based MMC coatings. *Wear* **306**, 185–195 (2013).
57. Luyckx, S., Sacks, N. & Love, A. Increasing the abrasion resistance without decreasing the toughness of WC–Co of a wide range of compositions and grain sizes. *International Journal of Refractory Metals and Hard Materials* **25**, 57–61 (2007).
58. Jacobson, G. A. Corrosion Basics Corrosion - A Natural but Controllable Process. *NACE International* (2018).
59. McEwan, J. J. Corrosion Control in Southern Africa. *South Africa: Corrosion Institute of Southern Africa* (2004).
60. Joshi, C. Characterization and corrosion of BCC-tantalum coating deposited on aluminum and steel substrate by dc magnetron sputtering. (New Jersey Institute of Technology, 2003).
61. G01 Committee. *Test Method for Conducting Potentiodynamic Polarization Resistance Measurements*. (ASTM International, 2018). doi:10.1520/G0059-97R14
62. Fontana, M. G. *Corrosion engineering*. (McGraw-Hill, 1986).
63. Jones, D. A. *Principles and prevention of corrosion*. (Prentice Hall, 1996).
64. Rahman, R. *Anodic Protection Evans diagram.* (2017).
65. Brookes, K. J. A. Corrosion damage in WC/Co. *Met. Powder Rep* 82–87 (2015).
66. Sharma, R. Erosion Corrosion. (2016).
67. Phadke, M. S. Introduction To Robust Design (Taguchi Method). *iSixSigma* (2018).
68. Athreya, S. & Venkatesh, Y. D. Application Of Taguchi Method For Optimization Of Process Parameters In Improving The Surface Roughness Of Lathe Facing Operation. *International Refereed Journal of Engineering and Science* 13–19 (2012).
69. Karna, S. K. & Sahai, R. An Overview on Taguchi Method. *International Journal of Engineering and Mathematical Sciences* **1**, 11–18
70. Nist Sematech. Blocking of full factorial designs. *Engineering Statistics Handbook* (2015).
71. Goyal, T., Walia, R. S. & Sidhu, T. S. Multi-response optimization of low-pressure cold-sprayed coatings through Taguchi method and utility concept. *The International Journal of Advanced Manufacturing Technology* **64**, 903–914 (2013).

72. Goyal, T., Walia, R. S. & Sidhu, T. S. Effect of Parameters on Coating Density for Cold Spray Process. *Materials and Manufacturing Processes* **27**, 193–200 (2012).
73. Goyal, T., Walia, R. S. & Sidhu, T. S. Study of Coating Thickness of Cold Spray Process Using Taguchi Method. *Materials and Manufacturing Processes* **27**, 185–192 (2012).
74. Plansee. *Molybdenum.* (Plansee., 2018).
75. Centerline (Windsor) Limited, Supersonic Spray Technologies. *Technical data sheet: Ni SST-N5001 Commercial Powder*. (2015).
76. E04 Committee. *Test Method for Knoop and Vickers Hardness of Materials*. (ASTM International, 2018). doi:10.1520/E0384-11E01
77. E04 Committee. *Test Methods for Determining Area Percentage Porosity in Thermal Sprayed Coatings*. (ASTM International, 2018). doi:10.1520/E2109-01R14
78. Smith, C. S. & Guttman, L. Measurement of Internal Boundaries in Three-Dimensional Structures By Random Sectioning. *JOM* **5**, 81–87 (1953).
79. Zu, J. B., Hutchings, I. M. & Burstein, G. T. Design of a slurry erosion test rig. *Wear* **140**, 331–344 (1990).
80. G01 Committee. *Practice for Conventions Applicable to Electrochemical Measurements in Corrosion Testing*. (ASTM International). doi:10.1520/G0003-89R10
81. G01 Committee. *Reference Test Method for Making Potentiodynamic Anodic Polarization Measurements*. (ASTM International). doi:10.1520/G0005-94R11E01
82. G01 Committee. *Practice for Calculation of Corrosion Rates and Related Information from Electrochemical Measurements*. (ASTM International). doi:10.1520/G0102-89R15E01
83. J01 Committee. *Terminology and Acronyms Relating to Corrosion*. (ASTM International). doi:10.1520/NACEASTMG0193-12D
84. Wolfram Research Inc. ElementData. Vickers Hardness of the elements. (2018).
85. *CRC materials science and engineering handbook*. (CRC Press, Taylor & Francis Group, 2016).
86. Whitcomb, P. J. & Anderson, M. J. Robust design — reducing transmitted variation: finding the plateaus via response surface methods. in *ASQC Qual Cong Proc* **50**, 642–651 (1996).
87. Unitek Miyachi Group. *Welding Material Control.* 1–5 (1999).
88. Verpoort, C. M. & Gerdes, C. Influence of Shot Peening on Material Properties and the Controlle Shot Peening of Turbine Blades. *Metal Behaviour and Surface Engineering, IITT-International* (1989).

89. Sudharshan Phani, P., Srinivasa Rao, D., Joshi, S. V. & Sundararajan, G. Effect of Process Parameters and Heat Treatments on Properties of Cold Sprayed Copper Coatings. *Journal of Thermal Spray Technology* **16**, 425–434 (2007).
90. Lee, H., Shin, H., Lee, S. & Ko, K. Effect of gas pressure on Al coatings by cold gas dynamic spray. *Materials Letters* **62**, 1579–1581 (2008).
91. Pattison, J., Celotto, S., Khan, A. & O'Neill, W. Standoff distance and bow shock phenomena in the Cold Spray process. *Surface and Coatings Technology* **202**, 1443–1454 (2008).
92. Boiko, V. M. & Poplavskii, S. V. Drag of nonspherical particles in a flow behind a shock wave. *Combustion, Explosion, and Shock Waves* **41**, 71–77 (2005).
93. Hassan, M. S. & Lau, R. W. M. Effect of Particle Shape on Dry Particle Inhalation: Study of Flowability, Aerosolization, and Deposition Properties. *AAPS PharmSciTech* **10**, (2009).
94. International Syalons (Newcastle) Limited. *Silicon Carbide*. (International Syalons (Newcastle) Limited, 2018).
95. NDT Resource Center. *Tensile Properties*. (NDT Resource Center, 2018).
96. Ogunmuyiwa, E. *Processing, characterization and tribological assessment of novel WC-VC-Co coatings and alloys*. (University of the Witwatersrand, 2014).
97. Total Materia. *Corrosion of Nickel-Base Alloys*. (2001).
98. Lin, N. *et al.* Influence of TiC additions on the corrosion behaviour of WC–Co hardmetals in alkaline solution. *International Journal of Refractory Metals and Hard Materials* **46**, 52–57 (2014).
99. Wentzel, E. J. & Allen, C. Erosion-corrosion resistance of tungsten carbide hard metals with different binder compositions. *Wear* **181**–**183**, 63–69 (1995).
100. Mohotsi, M. *Johannesburg Metro Water Quality Report*. (Rand Water, 2016).

9. Appendix

Section A

Publications and conferences:

1. Lioma, D., Sacks, N. & Botef, I. Cold gas dynamic spraying of WC–Ni cemented carbide coatings. *International Journal of Refractory Metals and Hard Materials* 49, 365–373 (2015).
   journal ISSN: 0263-4368
   DOI 10.1016/j.ijrmhm.2014.08.017

2. Lioma D., Sacks N. and Botef I., Cold gas dynamic spraying of wear resistant WC-based coatings, 11th International Tribology Conference, 10-12 March 2015, Pretoria, South Africa, 2015.

Section B

WC-Ni based powder properties:

Refer to the attached disc for all the the raw data used to determine the particle size distribution and XRD graphs of the as-received and milled WC-Ni based powders.

Section C

Taguchi DoE calculations:

2 FACTOR - 4 LEVELS

* Nickel content: 4,10,25,50

* Pressure 100, 150, 200, 250

2 FACTORS - 2 LEVELS

* Temperature: 450, 550

* Standoff Distance: 10, 15 mm

*Total number of experiments **without** Taguchi DoE technique:*

= (Σ WC_{ox}-xNi coatings + Σ WC_{12Co}-xNi coatings + Σ WC_{10Ni}-xNi coatings) x3 repeats*

= $(4^2x2^2 + 4^2x2^2 + 4^1x3^12^2)x3$

= 528 coatings to be sprayed for optimisation study

*Since WC_{ox}-xNi and WC_{12Co}-xNi coatings have 2 factors with 4 levels (Stagnation pressure & wt%Ni) and 2 factors with 2 levels (Temp & SOD) , while the WC_{10Ni}-xNi coatings have 1 factor with 4 levels (Stagnation pressure), 1 factor with 3 levels (wt%Ni) and 2 factors with 2 levels (Temp & SOD).

*Total number of experiments **with** Taguchi DoE technique:*

= (Σ$L16_{OA}WC_{ox}$-xNi coatings + Σ$L16_{OA}WC_{12Co}$-xNi coatings + Σ$L16_{OA}WC_{10Ni}$-xNi coatings) x3 repeats*

= (16+16+12*) x3

=132 coatings to be sprayed for optimisation study

*All the $L16_{OA}$ spray combinations requiring 4 wt% Ni were eliminated for the WC_{10Ni}-xNi powders as the minimum Ni content was 10 wt%.

Response variables to be measured:

*Coating thickness

*Coating hardness

Example of calculation

SNR (Thickness) $= -\mathbf{10}\ \mathbf{log}\ [\frac{\mathbf{1}}{\boldsymbol{R}}\sum_{\boldsymbol{j}=\mathbf{1}}^{\boldsymbol{R}}\frac{\mathbf{1}}{\boldsymbol{Y_j}^2}]$ Equation 9.1 [71].

= -10 log ($\frac{1}{3}$*Σ (1/Y^2))

= -10 log ($\frac{1}{3}$* ($\frac{1}{x1^2} + \frac{1}{x2^2} + \frac{1}{x2^2}$)

= -10 log ($\frac{1}{3}$*($\frac{1}{86,7^2} + \frac{1}{92,5^2} + \frac{1}{144,6^2}$)

= -10 log ($\frac{1}{3}$ *2,97898 E-04)

= 40,0305

Where Y_j j = 1,2… n are the response values under the trial conditions repeated R times, being hardness and coating thickness for the current study.

Average SNR = $\frac{SNR\ (Thickness)+SNR\ (Hardness)}{2}$

Parameters with highest Average SNR were selected as the optimal.

							Thickness measurements					
OA Experiment No.	**Repetition number (R1)**	**Sample number**	**% Nickel**	**Pressure**	**Temp**	**SOD**	**x1 (µm)**	**x2 (µm)**	**x3 (µm)**	**Average x (µm)**	**Σ (1/Y^2)**	**S/N ratio**
1	1	1	**4**	**100**	**450**	**10**	90,9	86,2	82,9	86,7	2,97898E-04	40,0305
	2	2					81,5	99,1	96,8	92,5		
	3	3					338	41,4	54,5	144,6		

Utility calculations:

Confidence interval (CI) calculation for predicted hardness and thickness values:

$\bar{x} + 1.96 \frac{\sigma}{\sqrt{n}}$ upper bound

$\bar{x} - 1.96 \frac{\sigma}{\sqrt{n}}$ lower bound

Where σ is the standard deviation of the full set of hardness/thickness values and n is number of thickness/hardness measurements used in the calculations.

Refer to the attached disc for the raw data and full set of calculations used in the Taguchi DoE optimization study.

Section D

<u>WC-Ni based coating properties:</u>

Refer to the attached disc for all the FESEM images and the raw data used to determine the properties and the XRD graphs of the WC-Ni based coatings.

Section E

The addition of Mo and TiC to the WC-Ni based coating

Refer to the attached disc for all the FESEM images and the raw data used to determine the coating properties.

Section F

Erosion results

Refer to the attached disc for the raw data and full set of calculations to determine the erosion properties of the coatings.

Section G

Corrosion results

Refer to the attached disc for the raw data and full set of calculations to determine the corrosion properties of the coatings.